Performance Demonstration of Guided Waves based Structural Health Monitoring system for Aerospace Application

Sanjay Sharma

université PARIS-SACLAY

Performance demonstration of guided waves based structural health monitoring system for aerospace application

Démonstration de la performance d'un système de contrôle santé des structures par ondes guidées pour une application aérospatiale

Thèse de doctorat de l'université Paris-Saclay

École doctorale n° 580, sciences et technologies de l'information et de la communication (STIC)
Spécialité de doctorat : Traitement du signal et des images
Graduate School : Informatique et sciences du numérique
Référent : ENS Paris-Saclay

Thèse préparée à l'**Institut LIST** (Université Paris-Saclay, CEA), sous la direction de **Bastien CHAPUIS**, Ingénieur-chercheur, et le co-encadrement d'**Olivier MESNIL**, Ingénieur-chercheur

Thèse soutenue à Paris-Saclay, le 24 octobre 2022, par

Sanjay SHARMA

Composition du jury

Sylvie LE HÉGARAT-MASCLE Professeure, Université Paris-Saclay	Présidente
Nazih MECHBAL Professeur, ENSAM Paris	Rapporteur & Examinateur
Patrice MASSON Professeur, Université de Sherbrooke (Canada)	Rapporteur & Examinateur
Odile ABRAHAM Chercheuse HDR, Université Gustave Eiffel	Examinatrice
Bastien CHAPUIS Ingénieur-chercheur, CEA-List	Directeur de thèse

THESE DE DOCTORAT
NNT: 2022UPASG073

université PARIS-SACLAY

ÉCOLE DOCTORALE
Sciences et technologies de l'information et de la communication (STIC)

Titre : Démonstration de la performance d'un système de contrôle santé des structures par ondes guidées pour une application aérospatiale

Mots clés : SHM, ondes élastiques guidées, transducteur piézoélectrique, SHM-POD, MAPOD, *length-at-detection*, *random effects*

Résumé : Les ondes élastiques guidées émises et reçues par des transducteurs piézoélectriques minces sont reconnues comme une technologie prometteuse pour plusieurs applications de surveillance de l'état de santé des structures (ou Structural Health Monitoring - SHM), en particulier pour les composants aérospatiaux. La démonstration des performances de ces systèmes, souvent exprimées en termes de courbe de probabilité de détection (POD), est un élément clé du déploiement réussi de cette technologie dans l'industrie. La détermination expérimentale de la courbe POD nécessite de nombreux échantillons instrumentés, ce qui rend son coût prohibitif. Une approche basée sur la simulation, ou assistée par un modèle, est une alternative intéressante. Cependant, la simulation de systèmes SHM basés sur les ondes guidées et la détermination de la courbe POD de tels systèmes sont jusqu'à présent limitées en raison d'un manque de méthodologie spécifique, de procédures, de méthodes statistiques appropriées et de validation.

Cette thèse propose une méthodologie générale pour une approche POD assistée par la simulation de système SHM par ondes guidées, avec une démonstration sur la surveillance d'une fissure croissante à partir d'un trou dans une plaque d'aluminium. La méthodologie tire parti de l'outil de simulation par éléments finis spectraux transitoires dans le domaine temporel développé au CEA-List (module CIVA SHM) qui permet d'exécuter les grandes campagnes de simulation nécessaires pour déterminer une courbe POD.

Un nouveau modèle d'actionneur hybride a été proposé dans ce travail en considérant le comportement dépendant de la fréquence du transducteur et la contrainte normale en plus de la contrainte radiale comme charges surfaciques afin de permettre l'utilisation de la simulation sur une plus grande gamme de fréquences d'excitation, adaptées à l'application visée. Deux méthodes récentes et appropriées d'un point de vue statistique : la *length-at-detection* et *random effects*, ont ensuite été adaptées pour estimer et comparer la courbe POD à partir des ensembles de données expérimentales et simulées. L'approche bayésienne s'est avérée plus utile que l'estimation du maximum de vraisemblance pour l'estimation des paramètres du modèle de la méthode *random effects* afin de comparer la limite d'incertitude pour chaque paramètre du modèle à partir des ensembles de données expérimentales et simulées. Enfin, une étude de détermination de la taille de l'échantillon a été menée sur la base de la méthode *random effects* afin d'identifier le nombre d'échantillons nécessaires pour répondre aux exigences d'une application SHM particulière.

Tous ces résultats montrent une grande confiance dans l'approche assistée par la simulation pour l'estimation de la POD et confirment le potentiel de cette solution en tant qu'outil compatible avec les exigences industrielles pour la démonstration des performances des systèmes SHM basés sur les ondes guidées.

université PARIS-SACLAY

ÉCOLE DOCTORALE
Sciences et technologies de l'information et de la communication (STIC)

Title : Performance demonstration of guided waves based structural health monitoring system for aerospace application

Keywords : SHM, guided elastic waves, piezoelectric transducer, SHM-POD, MAPOD, *length-at-detection*, *random effects*

Abstract : Guided elastic waves emitted and received by thin piezoelectric transducers are recognized as a promising technology for several applications of Structural Health Monitoring, especially for aerospace components. Demonstration of the performances of such systems, often expressed in terms of Probability Of Detection (POD) curve, is a key enabler of the successful deployment of the technology in industry. POD curve experimental determination requires many instrumented samples making its cost prohibitive. A simulation-based approach, or model-assisted, is an attractive alternative. However, simulation in guided waves based SHM and POD determination of such systems are so far limited due to a lack of specific methodology, procedures, appropriate statistical methods, and validation.

This thesis proposes a general methodology for a model-assisted POD approach of guided waves based SHM, with a demonstration of monitoring a growing crack from a hole in an aluminum plate. The methodology benefits from the efficient time domain transient spectral finite element simulation tool developed at CEA-List (CIVA SHM module) that allows running the large simulation campaigns required to determine a POD curve.

A new hybrid actuator model has been proposed in this work by considering the transducer frequency-dependent behavior and normal stress in addition to radial stress as surface loads to enable the use of simulation on a higher range of excitation frequencies, suitable for the targeted application. Two recent suitable statistical methods : *length-at-detection* and *random effects*, have then been adapted to estimate and compare the POD curve from both experimental and simulated datasets. The Bayesian approach is found to be more useful in model parameter estimation of *random effects* method for comparing the uncertainty bound for each model parameter from experimental and simulated datasets than Maximum Likelihood Estimation. Finally, a sample size determination study has been conducted based on the *random effects* method to identify how many samples are required to achieve the requirement of a particular SHM application.

All these results show great confidence in the model-assisted approach to POD estimation methodology and confirm the potential of this solution as a cost-effective tool for performance demonstration of guided waves based SHM systems.

Dedicated to Nidhi

Acknowledgment

Foremost, I express my deep and sincere thanks to my thesis director Dr. Bastien Chapuis and my supervisor Dr. Olivier Mesnil for their patience, motivation, enthusiasm, and immense knowledge. Their guidance and advice continuously support me in all the research and writing this thesis at CEA Paris-Saclay. Working with them has been an enriching and pleasant experience.

Special thanks to David Barncel from ArianeGroup, France, who took the time to come to my thesis defense and asked exciting queries on the industry application of my thesis.

I am also thankful to my committee members, Prof. Nazih Mechbal, Prof. Patrice Masson, Prof. Sylvie Le Hégarat, and Dr. Odile Abraham, for their encouragement and insightful comments on my Ph.D. work.

My sincere thanks also go to Dr. Pierre Calmon and Prof. S. Gopalakrishnan (IISc, Bangalore, India) for offering me the Ph.D. opportunity at CEA to work in one of the best public research groups.

I thank Dr. Valentin Serey for assisting me in COMSOL and Alexandre Yoshitaka Charau for helping me carry out experiments in the lab. I thank my friends and colleagues at CEA, Arthur, Jean-François, Vivek, Tinh, Jordan, Guillaume, Clément, Tzila, Nina, Amond, Jitendra, Tom, and Arnaud for making my research life in CEA pleasurable.

I also thank Arnesh, Preeti, Kavya, Sidhi, Aditi, and Shashaank, who has been a part of my life's ups and downs.

Last but never least, I want to mention my parents, brother Dr. Sachin, sister Suhani, bhabhi Ranu, and wife Nidhi, for being pillars of support during my entire journey of Ph.D.

Contents

List of Figures

List of Tables

CHAPTER 1

General introduction

Outline

1.1 Introduction

Recent advances in new materials and manufacturing, such as additive manufacturing and composites, are improving automobile, aerospace, and nuclear engineering structures. These advances ensure that the built structures are safe and deliver maximum service life. However, every day these structures encounter various hostile working environments and loading conditions (e.g., corrosion, fatigue, aging...) that may degrade their service life and operational performance. These degradations sometimes lead to unexpected structural failures due to prolonged service. For example, the structural failure in the De Havilland Comet that crashed in 1954 was due to fatigue [1]. Most recently, the Polsevera Viaduct (Genoa, Italy) cable-stayed concrete bridge collapsed in 2018 due to the combined effects of corrosion and fatigue [2], and the 2004 gas pipeline explosion in Ghisleghion, Belgium, was caused by a leak in the pipeline [3]. Several similar accidents have been reported due to the

structural failure resulting in heavy financial losses as well as many casualties. Therefore, maintenance of critical infrastructures is essential to avoid such undesirable circumstances and guarantee that an engineering structure safely performs over a designed service period.

In aerospace industry, as in other industrial sectors, maintenance also plays an important role in operating costs, as it directly affects economic benefits, depending on the nature and purpose of maintenance work and its frequency [4]. Maintenance aims to preserve engineering structures in an operational condition by either preventing the transition to a failed state or restoring them following a failure by servicing, repairing, or replacing the required components. Maintenance costs involve not only the direct costs of the maintenance crew, repairs, and parts replacement, but also indirect costs such as unexpected maintenance costs due to sudden downtime of engineering structures (e.g., delay in flights), causing larger inconvenience to the users. Based on cost-effectiveness, maintenance strategies have evolved from corrective to preventive maintenance over the past several decades. Corrective maintenance, also named fault based detection, means this maintenance activity becomes engaged after damage or failure happens in the structure. Whereas preventive maintenance, also named time based detection, is carried out at predetermined intervals, in which structural components are timely replaced, despite remaining useful life. At present, inspection-based maintenance has become more prevalent, commonly known as nondestructive evaluation (NDE) or nondestructive techniques (NDT), to inspect and maintain these engineering structures. More precisely, these techniques evaluate the integrity of a structural component at predetermined intervals to provide a red/green signal for repairing and replacing activities. Many NDE techniques are currently functionally and routinely applied in industries, including, but not limited to, visual inspection, magnetic testing, liquid penetrant, eddy current, radiography, and ultrasonic testing [5]. Based on their application, these techniques are currently the primary approach for damage detection of aerospace structures (and also in other industrial sectors) with a lower replacement cost and better spare inventory management than preventive maintenance [6]. Despite their extensive uses in industries, most NDT techniques are offline (inspection in the laboratory or plant) and schedule-based, which means that inspections are planned based on running hours of a structure or on specified dates, resulting in high maintenance costs with many human interventions. For example, American Airlines maintenance and repair costs are around 25% of its operating costs to keep the structure running due to scheduled maintenance [7]. Furthermore, these costs further increase rapidly as the aircraft structure ages due to additional tasks to perform for the airworthiness certificate given by regulatory authorities like FAA (Federal Aviation Administration) and EASA (European Union Aviation Safety Agency). Sometimes unanticipated failures also lead to higher maintenance costs in NDT-based inspections due to the non-availability of spare parts or tight plant schedules.

In recent years, the number of commercial flights has proliferated, increasing the complexity of maintenance strategy and task scheduling. Hence, maintenance costs are requested to decrease, and the service level (rate of the flights on time) is expected to increase. Therefore, the aerospace industry is increasingly interested in condition-based maintenance/monitoring to perform cost-effective maintenance. This requirement has given rise to a new NDE approach called structural health monitoring (SHM) with the help of recent advance in sensors technology, embedded electronic instruments, and signal

processing [8–10]. This approach is envisaged as a damage prognosis system that would provide a real-time structure's health information and, ultimately, predicts the engineering structure's remaining useful life while they are in service. It promises cost savings over schedule-based inspections, as monitoring will be done only when and where it is needed. This would help to perform maintenance at a scheduled time when the maintenance activity is most cost-effective but before the structure fails in service. Ideally, the SHM system would keep the operational structure's reliability and maintenance costs constant over the years with reducing downtime and the safety of users.

1.1.1 SHM System, techniques, and application examples

A typical SHM system consists of a sensor network permanently integrated or embedded in the structure for data acquisition with a few central processing units to assess structural health [11–13]. This system uses analyzed historical trends with real-time recorded sensor data to continuously evaluate the current structure's health and raise the alarm whenever an operational structure suffers a malfunction or is damaged. The primary function of sensors is to transform structure states, such as damage, load, and temperature, into corresponding sensing signals to monitor structural health. As described by Rytter [14], an SHM system can ensure four levels of a damage assessment scale for an operational structure. Level 1 and Level 2 give information about the damage presence and location in the structure, respectively. Whereas Level 3 provides classification and quantification of damage (e.g., damage size), and the final Level 4 provides a prognosis for the remaining useful life of the structure. Each level requires information about a lower level, which means that subsequent levels contain more information about the damage.

Over the past two decades, numerous SHM techniques have been researched and developed based on either the global (assess the state of the entire structure) or the local (monitoring a specific part of a structure) interrogation of the structure [15, 16]. Types of SHM techniques entirely depend on a measurement of the physical effects and type of sensors, i.e., optical fibers, piezoelectric materials, and air/vacuum galleries, used to monitor the structure's health [17]. Based on the monitoring objectives, SHM techniques can

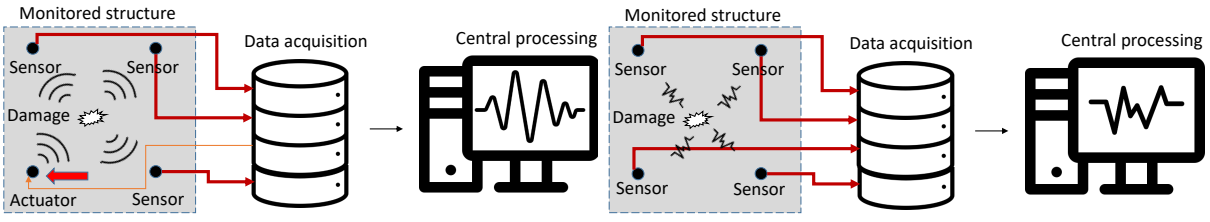

(a) Active (b) Passive

Figure 1.1: Types of damage monitoring.

generally be classified into operational and damage monitoring. Operational monitoring refers to the indirect assessment of the health status of a structure using measurements of operational and environmental parameters (e.g., pressure, temperature, vibration, stress, strain, and loading), whereas damage monitoring refers to the direct measurement of damage (e.g., cracks, delamination) in the structure which can be viewed as an embedded NDT

system. Furthermore, the damage monitoring-based SHM system can be passive or active depending on how the sensor works during the damage assessment. An active damage monitoring uses a diagnostic input signal, i.e., an actuation signal, through a signal generator to excite the structure by activating one sensor or all sensors sequentially. At the same time, other remaining sensors simultaneously use the data acquisition devices to record the propagating damage interacted signals in the structure, as shown in Figure 1.1(a). In contrast, under passive damage monitoring, all structural sensors only record the stress waves emanating from cracks, fiber breakage, and expansion of the matrix cracking, i.e., no need for diagnostic input, as shown in Figure 1.1(b). Many operational monitoring techniques have been studied for a long time and are relatively more mature than damage monitoring. The maturity, development, rank, and rate of evolution of SHM techniques are estimated based on Technology Readiness Levels (TRL) from 1 to 9, with 1 being the least and 9 being the most mature technology (similar to NASA TRL metric), as described by Roach and Neidigk [18]. Currently, most SHM techniques lie between 3 to 5 TRL (in the development phase), while some SHM techniques have reached TRL 8 (ready to use).

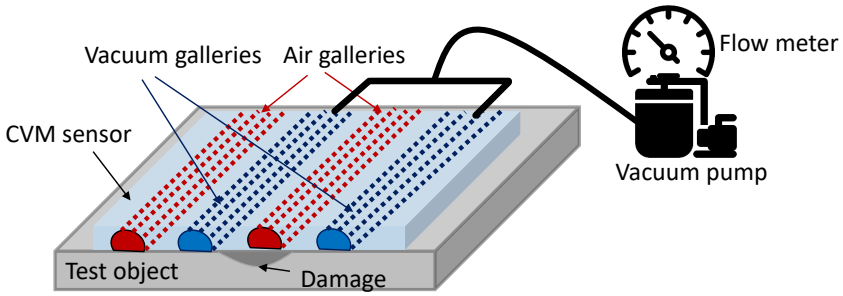

Figure 1.2: Schematic of comparative vacuum monitoring.

For example, one of the highest SHM TRL in aerospace is Comparative Vacuum Monitoring (CVM), which uses a sensor pad consisting of air/vacuum galleries, i.e., a pattern of alternating vacuum and atmospheric pressure galleries, as shown in Figure 1.2. Vacuum galleries maintain lower pressure with the help of a pump, while a flowmeter measures pressure in vacuum galleries. Whenever a crack initiates/propagates under the sensor, the pressure in vacuum galleries increases due to air leakage from atmospheric pressure galleries. This indicates a crack in structure based on the differential pressure between the recorded baseline and current pressure in the flowmeter. It was first installed and successfully tested in 2002 as part of a test program on a US Navy H-53 helicopter [19]. This technique provided the structure health in 5 minutes without any requirement of disassembling the structural parts. While in old conventional methods, where disassemble, inspection, and reassemble takes approximately 4 hours and need of scheduled inspection after every 25 fights hours. However, a significant limitation of CVM is that it can only detect damage underneath the sensor, i.e., the detection range is zero. This technique is most helpful in detecting damage at a hotspot where the damage location is well-known. It is the first (and currently the only one) SHM system certified by FAA in 2017 [20].

Another mature and promising monitoring technique is Acoustic Emission monitoring [21]. In it, sensors record radiation of acoustic (elastic) waves that occur in structure

when a material undergoes irreversible changes in its internal structure due to deformation, fiber breakage, and any other type of damage. Generally, this technique measures acoustic emission parameters, such as amplitude and arrival time, through piezoelectric sensors and estimates the presence and location of damage based on the measured parameters. An example of a successful application is the Acoustic Emission Helicopter Health and Use Monitoring System (AE-HUMS) as a tool for damage detection in helicopter drivetrains [22]. This technique was tested on an SH-60 drivetrain and identified a growing crack in a pinion gear more than fifteen minutes before gear failure. Other operational monitoring techniques, such as vibration-based monitoring [23, 24], measure the changes in a structure's modal characteristics for damage identification and are primarily used in rotating machinery. Similarly, local strain monitoring measures the local strain using strain gauges [25] and Fiber Bragg Grating (FBG) sensors [26] but suffers from the drawbacks of requiring more sensors on the structure.

Additionally, it should be noted that among various types of transducers, piezoelectric transducer-based SHM techniques are widely used due to their unique characteristics of dual coupling phenomena, allowing them to act as both actuator and sensor. The electromechanical impedance SHM technique is one of the monitoring techniques that mainly uses piezoelectric transducers, which can readily be bonded to structure and measures the electrical impedance of piezoelectric transducers for damage identification [10, 27, 28]. The damage changes the stiffness near the piezoelectric transducer, i.e., change in resonance frequency of a structure, resulting in a change in the piezoelectric transducer's impedance. It actively sends frequency broadband signals to record current impedance and diagnose based on the baseline impedance response. The advantage of this technique is that insensitive to changes in the boundary condition or operational vibrations. The low power requirement for piezoelectric transducer excitation and model-independent nature makes them suitable for complex structures. This technique has the potential to identify small damage, but their sensitivity drops off dramatically with increasing distance between the damaged location and the transducer. A bigger network of impedance-based transducers is needed to provide an effective damage detection tool for larger structure inspection.

Another monitoring technique, based on the use of guided waves (GWs) emitted and received by piezoelectric transducers, has evolved as a promising technology for structural health monitoring since they can quickly determine the location, severity, and type of damage whenever needed [29–31]. It is already well established in NDT, commonly known as ultrasonic guided waves testing [32], and is now part of an extensive research effort especially for aerospace structures [33]. A significant advantage of guided waves over other inspection/monitoring techniques is that they can help to monitor over long distances with high sensitivity to damage, resulting in the need of a limited number of sensors to monitor a given zone. They also have the ability to monitor the hard-to-reach hidden or complex structures [34]. The following section explains their specific advantages and application in details.

1.2 Ultrasonic wave techniques

Ultrasonic NDT wave techniques are generally based on measuring changes in the propagation characteristics of ultrasonic waves in a structure due to local damage interactions. Based on ultrasonic waves, many ultrasonic testing have been developed and are currently used in the industry. In conventional ultrasonic testing, a movable ultrasonic transducer is attached to a diagnostic machine to record ultrasonic bulk waves [35]. Through-transmission or pitch-catch system sends a wave from one side of the structure, and a separate transducer records the signal of the wave as it travels through the structure. Any fault between the transducer and the receiver reduces the wave amplitude or changes the phase, indicating damage to the structure. While a pulse-echo system technique measures reflection from damage using a single transducer. These techniques have shown their ability to detect small defects with high sensitivity in many industrial applications. The major limitations of these techniques are the narrow inspection area and the necessity of direct access of an inspector or robot close to the inspected part. These constraints make these conventional techniques not very appropriate for SHM or real-time monitoring.

A particular type of ultrasonic waves, called guided waves (GWs) have become more popular among researchers and industries in this perspective for SHM due to their possibility to propagate on large distances with low attenuation, which makes them more cost-effective for monitoring larger and extended structures. These waves use the structure as a waveguide, e.g., in a plate, the waves propagate between two free surfaces called guides [34]. Several GW classes have been studied depending on the stress boundary conditions of the bounded surfaces. Rayleigh waves are a type of GWs that travel along the stress-free surface of the structure with the decay amplitude in the direction of the thickness. Similarly, other classes of GWs are the Love waves that travel between two layers of a material, the Stoneley waves that propagate along the interface of two materials [36], and the more common Lamb waves that propagate in a thin structure bounded by two stress-free surfaces. Lamb waves exist when their wavelength is higher than or comparable to the thickness of a structure. These waves have an adjustable frequency range to inspect various sizes (a few millimeters to a few centimeters) and damage types, making them sensitive to various defects [37]. GWs in plate-like structures have long-range propagation and low attenuation characteristics, which significantly limit the number of sensors required to monitor a given critical zone or a component. Therefore, quick inspection is possible without the need for direct human or robot access to the structure, which makes GWs potentially suitable for SHM and meets most of the real-time inspection requirements.

An essential requirement for performing ultrasonic testing is transducer type, where the most commonly used transducers in ultrasonic testing are piezoelectric (e.g., angle wedge and comb piezoelectric transducers) [38, 39] and electromagnetic acoustic transducers (EMAT) [40] and are routinely used in the industry for monitoring and maintenance. The use of ultrasonic transducers is inconvenient for SHM applications as these transducers are generally bulky, expensive, and cannot be easily integrated or embedded in the structure. However, new advancements in transducer technology have overcome these impediments for enabling on-demand interrogation of structures for GWs based SHM. The small and thin piezoelectric transducer has become more appealing to researchers since it is inexpensive, lightweight, readily available in various shapes (square, rectangular, and

circular), and can be fabricated with a low thickness (typically 0.15 to 1 mm) [31, 41]. Their compact dimensions and characteristics make them easily mountable via an adhesive film (e.g., epoxy) to a structure or inserted between plies of a composite laminate during its fabrication. The dual coupling phenomenon between electrical and mechanical properties, known as the direct or inverse piezoelectric effect, makes them more suitable for GWs based SHM inspection [42]. The direct piezoelectric effect induces mechanical strain in the piezoelectric transducer under an electric voltage and transfers mechanical strain to the structure via an adhesive film. While the inverse piezoelectric effect generates an electric voltage under the mechanical strain in the structure. Hence, a single piezoelectric transducer can actuate and sense the GWs on the structure by covering a larger area [43]. Many types of piezoelectric materials are available, e.g., it is PZT material (Lead Zirconate Titanate) and a PolyVinyliDene Fluoride piezoelectric transducer (PVDF) [44] is an alternative that offers flexibility, and can be incorporated into the curved and deformable structure, whereas ceramic piezoelectric transducers are brittle in nature restricting them to use on rigid surfaces.

Other transducers can also be used in GWs based SHM. Fiber optics, especially Fiber Bragg Grating (FBG), have the potential for SHM due to their flexibility, easy integration in structure, and improved robustness to harsh environmental conditions (high temperature, chemical and radiations aggression...), making them attractive to SHM [45]. However, the acquisition is complicated and costly in practice. Other transducers, such as magnetostrictive sensors [46, 47], are also available, but they are still underdeveloped.

A laser Doppler vibrometer (LDV) is also a popular device for measuring GWs without contacting a structure based on the Doppler effect [48]. It helps in imaging techniques for detecting and understanding the interaction of GWs with damage from recorded grid points on the structure. However, they cannot be included in a structure for SHM as they are large in size, making it only a tool to better design GW based SHM systems.

Previous research emphasized GWs potential use in detecting cracks and delaminations by employing conventional angle-probe ultrasonic transducers studied by Rose [49]. Alleyne et al. [50] have used GWs to detect circumferential cracks and corrosion in steel pipes and Dalton et al. [51] has studied the potential use of GWs for monitoring metallic aircraft structures. Moreover, Cawley and Alleyne [52] have shown Lamb waves' applicability for long range in composites material.

Hence, GWs based monitoring has the possibility to facilitate on-demand inspection using few piezoelectric transducers or fiber optics to monitor real-time structure health for SHM. Their propagation in thin structures makes them more suitable for thin plate, shell-type-thin-walled, stiffeners, and other airframe parts of aircraft structures.

1.2.1 Guided waves based SHM

A typical active GWs based SHM system requires sensors, data acquisition devices, signal processing systems, and power systems [10, 53]. Sensors are permanently installed on the structure and are usually connected to a signal generator with data acquisition devices, as shown in Figure 1.3. Thin piezoelectric transducers, have been employed in the majority of GWs based SHM systems [54, 55]. These transducers are attached to or in the structure and generate various elastic wave modes, generally low order antisymmetric and

symmetric Lamb modes in isotropic plate-like structures or similar waves in anisotropic plate-like specimens (more explanation are given in chapter 2). The recorded GW signals

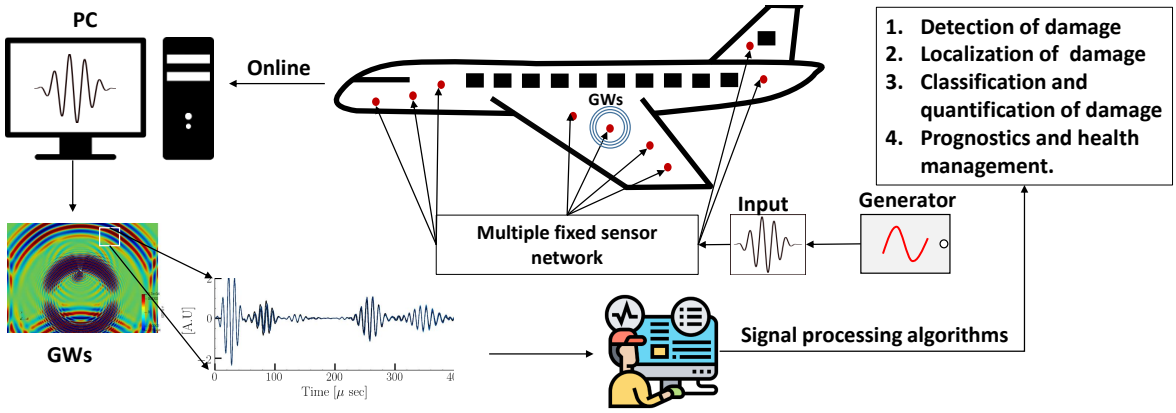

Figure 1.3: Schematic of active GWs based SHM.

through sensors are often complicated due to having multimode, dispersive, and containing reflection from the boundaries of a structure [45, 56]. Their interaction with geometrical features of the waveguide and potential structural flaws shows nearly similar mode conversion, reflection, and diffraction in the recorded signals. Similarly, environmental and operational conditions also change the GWs propagation [57]. For example, the temperature effect on GWs shows the changes in GW signals without any damage to the structure, as shown in Figure 1.4. Therefore, advanced signal processing is often needed, along with a sound knowledge of wave propagation, to extract the damage information from these complex variations in the signals.

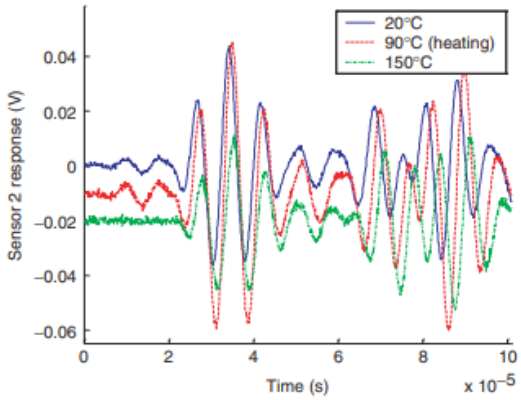

Figure 1.4: Temperature effects on GW signals at 120kHz [58].

Considerable work has been done on signal processing techniques of GW signals, as reported in [59]. Mainly two techniques are used for damage identification: baseline and baseline-free. A baseline technique compares a current recorded signal to a reference signal (pristine signal) [60]. This technique has become more widespread since it holds exclusively information related to damage after removing all other information in the signals,

e.g., reflection from the geometrical features. Damage index (DI) based damage detection has become more prevalent in the baseline technique since the estimation of DIs is simple, repeatable, fast, and highly sensitive to small damage. For example, Rizzo and di Scalea [61] and Giurgiutiu [10] presented a root mean square DI, peak-to-peak amplitude DI by Su and Ye [53] and Betz et al. [62], Time of flight (TOF) based DI [63], and some other types of DIs were recently published by Barreto et al. [64]. Imaging techniques are also developed to detect the location and size of damage based on array transducers, e.g., Delay and sum [65], correlation based Excitelet [66], minimum variance [67], and probabilistic imaging [68]. Recently, Kulakovskyi et al. [69] have reported a comparison of these imaging techniques. However, baseline techniques are highly affected by environmental and operational conditions [57], which often leads to false damage results in image analysis and other feature extraction techniques. In order to compensate for environmental effects, Croxford et al. [70] have reported a baseline subtraction technique. Similarly, Konstantinidis et al. [71] have reported optimal baseline selection (OBS), and Croxford et al. [72] used OBS with the baseline stretch method (BSM) [73]. While, baseline-free techniques are also extensively reported in the literature [74–76] to overcome temperature compensation methods. These techniques rely on the current recorded GW signals without a reference signal, making them environmentally less vulnerable to monitoring the damage but are much complicated to develop and have not reached high level of maturity so far.

Recently, many data-driven techniques such as machine learning and deep learning are rapidly emerging for identifying damage characteristics and temperature compensation [55, 77–80]. Numerous studies are reported on their use in GWs based SHM, as mentioned in a recent review paper by Sattarifar and Nestorović [81]. However, these techniques require a large amount of reliable data, which is limited in SHM studies.

As mentioned above, all GWs based SHM detecting algorithms have matured in the literature and laboratories. Although, their use in the industry is still insignificant, especially in the aerospace industry. The lack of performance demonstration methodology is identified by the SHM community as a major difficulty for such inspection systems transitioning to the industry [82]. The following section explains a complete understanding of the requirement and challenges of performance demonstration for GWs based SHM.

1.2.2 Industry adoption issue for GWs based SHM

A vast amount of literature has been reviewed on GWs use in SHM [13, 31, 45, 83]. Such SHM techniques are subjected to various sources of variabilities (the stochastic nature of physical phenomena) associated with uncertainties in the environment (temperature, radiation, humidity) and operating conditions, which may affect the performance of the SHM system [84, 85]. Therefore, an SHM system should be robust enough to detect the required minimum damage even in the presence of such variabilities. This requirement leads us to the need for a performance demonstration of SHM system to bridge the gap between scientific research and industrial [29].

The performance demonstration is already addressed in NDT system and the methodology is widely accepted by the industry. The MIL-HDBK-1823A [86] assesses NDT methods using the Probability of Detection (POD) curve. This curve is mapped via a standard statistical method (hit & miss or signal response) from the relationship between

the measured responses (e.g., damage index) under all the influencing variabilities and damage characteristics (e.g., crack length). The threshold is often defined above the noise in the inspection system and can be varied to find a compromise between the Probability of False Alarms (PFA) and POD [87]. POD curve is usually expressed as a function of crack length a with a_{90} (POD is 0.90 or 90% for a crack length) and $a_{90|95}$ (an upper bound 95% confidence interval for a_{90}) scaler values, as shown in Figure 1.5. It identifies largest defect size with a 95% confidence value that could be missed during inspection denoted as $a_{90|95}$. In a POD computation, capturing all the variabilities are necessary; otherwise, the

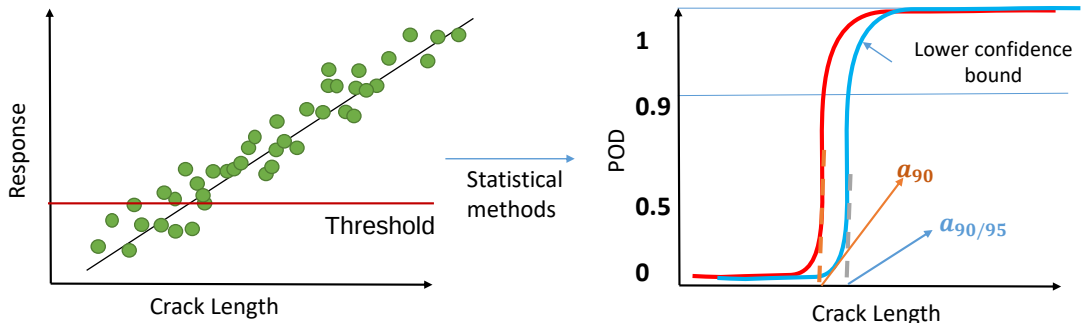

Figure 1.5: Illustration of the estimation of the POD curve from the relationship between the measured response and the crack length (left) to the POD curve (right) with its 95% confidence interval in blue.

POD curve can lead to a biased estimation. The most significant variabilities in the NDT system usually come from crack morphology, sensor devices (manufactured by various vendors and properties) and human factors [88, 89].

Similarly, the SHM system inherits all the variabilities from the NDE system. But in addition, in situ effects (temperature, humidity and, load) and sensor mounting variabilities affect the SHM system. Whereas in NDE, the in situ effects are generally less influent than human factor variability since most of the inspection happened in the laboratory or controlled environment where temperature, humidity and load do not change between the calibration step and the measurement. A table of main differences between NDE and SHM variabilities is mentioned in [82].

The same methodology of POD computation for NDT could be extended for SHM as reported in [29, 90–92]. Roach and Rice [93] have shown the potential need for SHM and POD study with a demonstration of an SHM experiment on an engine mount beam. However, one of the primary issues associated with POD estimation is to perform large-scale experiments containing all variabilities. It requires a large number of experiments with similar configurations, which is costly and cumbersome in NDT, but in SHM, it is prohibitively expensive due to the fixed nature of the sensor on the structure. In many NDT POD studies, this cost is overcome by a simulation-based approach, i.e., a physics-based approach to generate large amounts of data with many variabilities, even with those that are very difficult to acquire experimentally [94–98]. This simulation based approach POD estimation is also known as Model Assisted Probability of Detection (MAPOD) [99].

However, the SHM based POD or MAPOD studies are so far limited in the SHM community, as mentioned in [82, 100]. There are two main reasons behind it, the first is

the cost of performing a complete POD study either by experiment or simulation. Even MAPOD is computationally expensive, e.g., most of the GW based simulation and modeling tools are based on the traditional finite element method (FE), as mentioned in [101], that requires almost 10 to 20 degrees of freedom per smallest wavelength [102], whereas typical structures are several tens or hundreds of wavelengths long. For this reason, it is generally prohibitive to conduct MAPOD computations where hundreds or thousands of simulations must be executed. The second reason is the assumption of the data independence in the standard statistical methods used in NDT POD computations is invalid in the SHM system. Indeed in NDT, independent measurements are created by multiplying acquisition steps by different operators and transducers on a limited number of samples. In contrast, in SHM, the transducers are fixed to the structure; therefore, creating independent acquisitions on the same structure is impossible, which is why multiple structures are necessary. Shook et al. [103] have mathematically shown the effects on the POD curve of dependent and independent data.

However, to make use of the standard methods in SHM, Janapati et al. [104] have classified the SHM system into four categories based on data collection and damage location. Based on data collection, it is divided into two categories, first scheduled-based SHM (S-SHM) and second automatic-based SHM (A-SHM). The scheduled-based SHM means data can be collected over predetermined time intervals, whereas automatic-based SHM collects the data continuously in an automated way. They further divided S-SHM and A-SHM into known damage location and unknown damage location. They have mentioned that only known damage location with S-SHM can consider independent acquisitions, where one sample provides several measurements within a specific time interval. With this philosophy, many studies used standard statistical methods for POD computation of SHM, as mentioned in [105–108]. However, the repeated measurements from a fixed sensor on the structure and the two acquisition time intervals to define independent samples remains an open question.

Nevertheless, several SHM systems are designed for automatic damage identification, characterization, localization, and damage growth prediction, which create data dependent on repeated measurements on the same configuration. Some notable works are done toward enabling a POD study for A-SHM for considering dependency in the SHM data, i.e., Shook et al. [103] have developed a mathematical technique to construct a POD curve for dependent and independent data. Similarly, Kabban et al. [109] have presented a linear mixed effect statistical model for repeatedly measured fatigue crack growth in the wing spar lug of an aircraft to produce a POD curve. They have also calculated the number of samples required to reach the desired $a_{90|95}$ values for SHM. Recently, Meeker et al. [110] have proposed two new statistical methods for A-SHM: *length-at-detection* (LaD) and *random effects*. They have conducted crack detection experiments over thirteen metal plates, where plates were subjected to the cyclic fatigue load so that the crack grows over time. They have produced several POD curves for a growing crack and stated that LaD values follow the normal distribution. Later, O'Connor [111] quantified these two methods and specified that LaD is suitable for smaller samples (less than 10). Whereas, for bigger samples, the *random effects* method is more appropriate.

Only two research papers described above (Kabban et al. [109] and Meeker et al. [110]) have computed complete experimental POD for SHM. Kabban et al. [109] have used only

three samples, which is insufficient to conclude on the POD curve. In fact, in NDT POD, about 40 to 60 samples are required to reach a robust POD curve [86]. But in SHM POD there is no specific study that how many samples are needed to capture the maximum number of variabilities. Therefore, the MAPOD approach has raised a lot of interest in the SHM community to determine the appropriate statistical methodology further to estimate POD curves with high confidence.

1.2.3 Modeling and simulation of GWs based SHM for MAPOD

Modeling and simulation play a vital role in the GW based SHM system for understanding transducers structure interaction, complex wave patterns, dispersion relation, wave-damage interaction, and especially comprehending experiments findings [69, 76, 112]. Simulation is not only limited to MAPOD but also enables the use of various data-driven damage identification algorithms, e.g., machine learning and deep learning [79, 113]. Since they require a vast amount of datasets due to a high number of influencing parameters, conducting such analysis is experimentally expensive.

The extensive research on simulation and modeling tools for GW based SHM are presented in Willberg et al. [114] and Lee and Staszewski [115]. The modeling is not only limited to numerical techniques but also includes analytical and semi-analytical techniques. Numerical techniques mainly include the finite element method (FE), the finite difference method (FD), the spectral finite element method (SFE), and the boundary element method. Analytical [10, 116–118] and semi-analytical [119, 120] methods are studied to propagate GWs in infinite structures of finite cross-sections. However, such techniques are limited in terms of the structure's geometry [121, 122]. Another choice of simulation is FE for the research to enable the 3D modeling of GW based SHM. Some of the FE software offers multiphysics modules for modeling the transducer-structure coupling, which is often a critical and challenging part of the simulations [123]. A benchmark of the most common finite element software (Abaqus, COMSOL, and Ansys) platforms was conducted on a single composite of $120 \times 60 \times 1$ mm^3 with eight plies [101]. They noted that a single simulation at 300 kHz of central frequency requires 20 h to up to 1 week to complete with a powerful computer. Even GPU-based FE solvers are limited by the memory available on the GPU, and also massive data transfer from GPU is a bit slow [101]. Hence, FE is generally prohibitive for the MAPOD computations where hundreds or thousands of simulations must be executed.

This numerical computational cost issue is overcome by the SFE by reducing the number of degrees of freedom and a more efficient computation at each time step, reducing the overall computational cost [124–126]. Recently, Mesnil et al. [127] have reported comparing transient SFE integrated into the CIVA software platform with the experimental data of the Open Guided Wave database [128]. They have shown a good fit of the results below 100 kHz at a computational cost of a few hours [129], whereas conventional FE software provides similar results in several days to about a week of computation. These results prove that SFE has excellent potential to produce numerous simulations when performing MAPOD computations. In order to achieve such competitive computational performances of CIVA, two approaches are combined. First, SFE, using the higher-order elements compared to a classical formulation [130] and mesh parametrized with the help

of macro mesh [126]. The second approach is a simplified transducers model called as Pin force [131] model for transmitting and receiving the signals. Both approaches enable the CIVA for MAPOD, but the transducers model drastically limits the CIVA for larger GWs based SHM configurations of interest regarding higher excitation frequency [132]. More information on CIVA software can be extracted from EXTENDE company website[1]. As far as the author's knowledge is concerned, MAPOD based on SFE has not been done in the literature.

1.3 Motivations and objectives of thesis

Despite having demonstrated great potential in GWs based SHM for inspecting a structure in a laboratory, the industry transition is still a bit slow for it. While Airbus, Boeing, and other industries are paying close attention to it, they still have not fully succeeded in incorporating it into their aircraft [133]. One of the main barrier to mainstream adoption of the technology is the difficulty of demonstrating the performances of such a system. Especially for aerospace industries, the performances must be quantified in terms of the POD curve and certified before any usage of such inspection technologies. A major hindrance is the requirement of enormous expenditures to perform experimental POD curves and also a strong need for statistical expertise associated with the SHM POD study. This

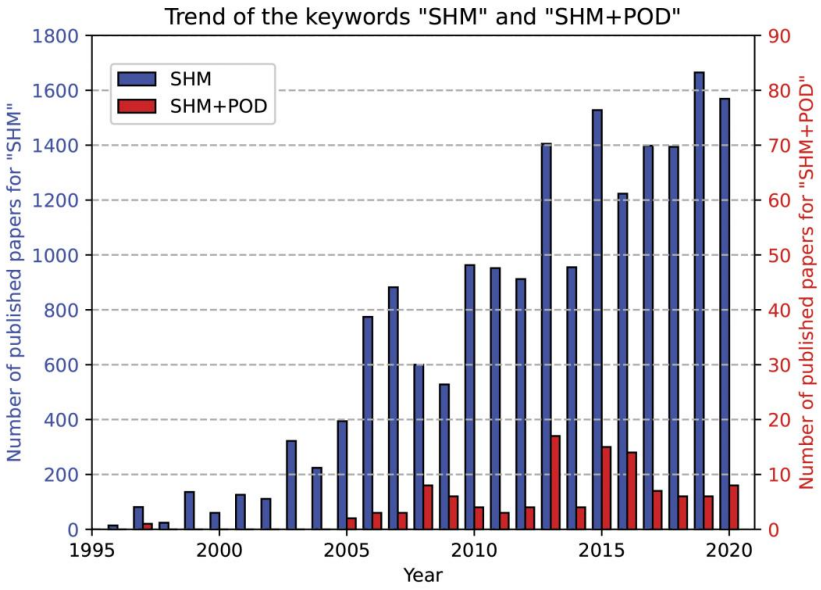

Figure 1.6: Trend of SHM and SHM+POD publications till 2021 mentioned by Falcetelli et al. [82].

limits the awareness of POD study in the SHM community against the SHM study, as shown in Figure 1.6. Scientists and researchers in this field are strongly encouraged to use the MAPOD method to demonstrate their performance, as mentioned in [109, 110] .

[1]https://www.extende.com/

In order to enable the MAPOD studies for GWs based SHM, as noted by Chapuis et al. [134] for NDT, similarly, the acceptance of MAPOD in the SHM community depends on three primary requirements:

1. Reliable and computationally fast simulation tools for SHM and wave interaction with damage [108].

2. Validation of the simulation with experiments for a maximum number of variabilities that influenced the SHM system is a solid requirement to produce consistent results of the physical model used in the simulation.

3. Validation of statistical algorithms that are to be used for SHM.

This thesis presents a general methodology and framework to demonstrate the performance of GWs based SHM through a MAPOD approach. A fast, reliable, and validated simulation tool is a primary requirement to achieve the above described objectives. A specific effort has therefore been spent to identify configurations on which the simulation tool used to generate the data in this thesis (CIVA SHM module) is validated. In particular, a new transducer model, compatible with the spectral finite element scheme implemented in the CIVA SHM module, has been proposed to demonstrate the applicability of the methodology at higher frequencies than allowed by the current model for configurations of practical interest in the aerospace industry.

The full methodology has finally been applied to the specific case of growing crack in aluminum plate's hole detection and compared with experimental data acquired on a large set of samples.

1.4 Contributions and outlines of thesis

Two major contributions have been made to achieve the above-mentioned requirements using simulation, experimentation, statistics, and sensor modeling. These contributions are presented as follows.

Chapter 2: A general overview of the Lamb wave theory for isotropic plates is described based on the famous Navier–Lamé equation. Along with it, a complete description of the transient spectral finite element scheme in CIVA is explained as a surface load with a pin force transducer model. Furthermore, the analytical formulation of the transduction equations is compared to that of the transient spectral finite element. Finally, in COMSOL, a complete piezoelectric transducer model with an adhesive is used to derive the limitations of the pin force transducer model based on a considered configuration.

Chapter 3: A hybrid actuator model (HAM) is proposed to overcome the previous limitations of the pin force model while being compatible with efficient transient spectral finite element scheme in CIVA. The HAM-obtained signals at two different configurations are compared with a pin force model and a COMSOL simulation with a fully described transducer using finite elements. An experimental study is also conducted using the correlation coefficient metric to compare quantitatively. [Paper under review in Ultrasonics]

Chapter 4: The complete methodological steps of POD calculations are presented for both experimental and model assisted SHM studies of a growing crack from a hole in

an aluminum plate. This simplified configuration is representative of numerous aerospace bolt components submitted to cracks introduced by fatigue. An extensive experimental procedure is conducted to obtain stochastic responses and also used to validate acquired datasets from a deterministic simulation tool under the considered variabilities. Both experimental and simulation time domain signals are compared and quantified in damage responses based on the damage index. In addition, the DI sensitivity study is presented with the sensor path and normalized crack length by wavelength.

Chapter 5: Two recently proposed POD statistical methods are demonstrated with their assumptions and formulation for computing the POD curve for the experimental and model assisted SHM datasets. Both experimental and simulated POD curves are compared and two common POD curve values, a_{90} and $a_{90|95}$, are calculated and compared with both statistical methods. Bayesian analysis-based parameter estimation and the underlying distribution of damage characteristics are used to validate the MAPOD approach with experimental POD. In addition, based on Bayesian analysis, a study is presented to calculate a sample size to estimate the required $a_{90|95}$ for a particular application.

At last, a conclusion and perspectives chapter is added, the research progress has been presented at three international conferences, one journal paper is under review, and the second is to be submitted to the SHM journal. Additionally, one more journal paper is currently under review, where experimental datasets are used from this thesis work, as mentioned in the following section.

1.5 Conferences and journal papers

1. Sanjay Sharma, Olivier Mesnil, Bastien Chapuis,& Pierre Calmon, Model Assisted POD for Guided Wave based Structural Health Monitoring of growing cracks, NDE 2019, Bangalore, India [Oral presentation]

2. Sanjay Sharma, Olivier Mesnil, Arnaud Recoquillay, & Bastien Chapuis, An Improved sensor model for efficient Guided Wave based Structural Health Monitoring simulation, the 13th International Symposium on NDT in Aerospace 2021, [Oral presentation]

3. Sanjay Sharma, Olivier Mesnil, Arnaud Recoquillay, & Bastien Chapuis, A Hybrid Actuator Model for Efficient Guided Wave Based Structural Health Monitoring Simulations Ultrasonics, 2022, [Under review]

4. Olivier Mesnil, Arnaud Recoquillay, Clément Fisher, Valentin Serey, Sanjay Sharma, & Oscar d'Almeida, Self-referenced robust guided wave based defect detection: application to woven composite parts of complex shape Ultrasonics, 2022, [Under review]

5. Sanjay Sharma, Olivier Mesnil, Arnaud Recoquillay, & Bastien Chapuis, Methodology for Probability of Detection curve of Guided Wave Structural Health Monitoring Journal of structural health monitoring, 2022, [To be submitted]

CHAPTER 2

Lamb waves in isotropic plates

Outline

2.1 Introduction

Lamb waves, one of the types of guided waves (GWs), propagate between two parallel surfaces that are guided between the upper and lower surface of a plate. As one of the most promising elastic waves for SHM applications, they propagate in the thin structural media by activating an attached transducer on or in the structure. These waves exhibit various elastic wave modes in the structure, which are classified into antisymmetric and symmetric modes. Lamb waves generated by a source or transducer of omnidirectional effects that cause propagation in a circular pattern in the structure are known as axisymmetric Lamb waves. A detailed derivation of axisymmetric Lamb waves is presented in the cylindrical coordinate system with the help of Hankel transformation in this chapter. After that, the dispersion relations are obtained for both modes.

An approximate transducer model of a circular piezoelectric transducer called the pin force (PF) model is considered to obtain an analytical formulation of the Lamb waves displacement field and sensor response. This chapter also provides validation of the transduction in the time-domain transient spectral finite element scheme for GWs based SHM recently implemented into CIVA software. The theoretical dispersion curve is compared with the computed one through a B-scan of displacement measurement from CIVA. Additionally, the lower-order modes amplitude response of displacement and sensor from CIVA is compared with analytically driven equations. Finally, an entire piezoelectric transducer is considered in COMSOL, which provides a PF model range in CIVA for a configuration.

2.2 Axisymmetric guided waves in isotropic plates

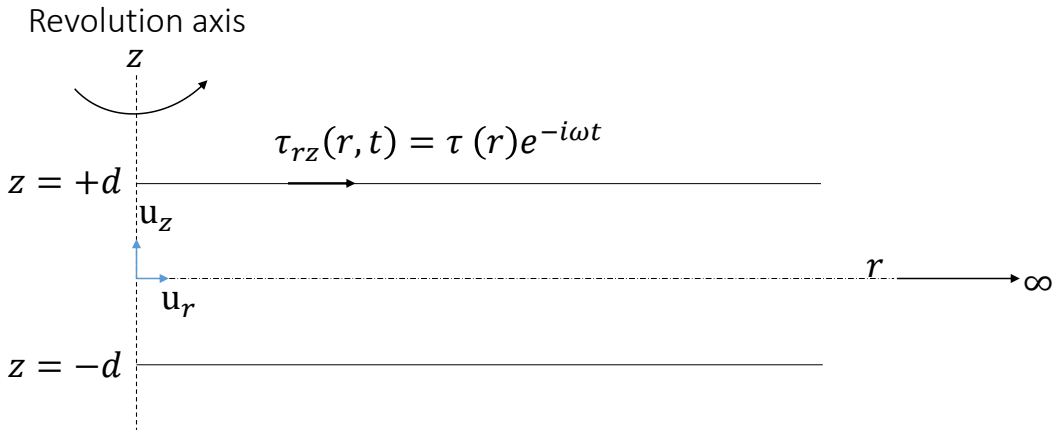

Figure 2.1: Axisymmetric structure.

Omnidirectional Lamb waves are often considered in SHM as they cover a larger area for inspection from a single transducer location. An infinite axisymmetric structure with thickness $2d$ is considered to obtain circular Lamb waves equations in a metallic plate, as shown in Figure 2.1. An approximate transducer model is assumed with a shear stress τ_{rz} in the radial direction at the upper surface with time-domain excitation, where ω is the frequency of excitation and t is the time. To formulate wave propagation, the Navier-Lamé equation of elastic solid can be represented as shown below:

$$(\lambda + \mu)\boldsymbol{\nabla}(\boldsymbol{\nabla} \cdot \mathbf{u}) + \mu\nabla^2\mathbf{u} = \rho\ddot{\mathbf{u}}, \tag{2.1}$$

where $\mathbf{u} = u_r\mathbf{e_r} + u_\theta\mathbf{e}_\theta + u_z\mathbf{e_z}$ denotes displacement filed vector, ($\boldsymbol{\nabla}$, ∇^2) representing a grad and a Laplacian operator, respectively. (λ, μ) denote Lame coefficients, and ρ is the density of the elastic structure. The displacement field is assumed to be expressed in terms of two potential functions, a scalar potential $\boldsymbol{\Phi}$ and a non-rotational vector potential $\mathbf{H} = H_r\mathbf{e_r} + H_\theta\mathbf{e}_\theta + H_z\mathbf{e_z}$, which is represented in the following form

$$\mathbf{u} = \boldsymbol{\nabla}\boldsymbol{\Phi} + \boldsymbol{\nabla} \times \mathbf{H} \tag{2.2}$$

Equation 2.2 is the Helmholtz decomposition and provides a unique condition $\boldsymbol{\nabla} \cdot \mathbf{H} = 0$. To obtain solution for the guided waves, Equation 2.2 is substituted into the Equation 2.1, which yields,

$$(\lambda + \mu)\boldsymbol{\nabla}\left(\nabla^2 \boldsymbol{\Phi}\right) + \mu\left(\nabla^2 \boldsymbol{\nabla}\Phi + \nabla^2 \boldsymbol{\nabla} \times \mathbf{H}\right) = \rho\left(\boldsymbol{\nabla}\ddot{\Phi} + \boldsymbol{\nabla}\ddot{\mathbf{H}}\right) \tag{2.3}$$

Equation 2.3 can be rearranged in the following form

$$\boldsymbol{\nabla}\left[(\lambda + \mu)\nabla^2 \boldsymbol{\Phi} - \rho\ddot{\Phi}\right] + \boldsymbol{\nabla} \times \left[\mu\nabla^2 \mathbf{H} - \rho\ddot{\mathbf{H}}\right] = \mathbf{0} \tag{2.4}$$

where the components (shown in brackets) in Equation 2.4 must be independently zero, as shown below:

$$C_p^2 \nabla^2 \boldsymbol{\Phi} - \ddot{\Phi} = \mathbf{0} \tag{2.5}$$

$$C_s^2 \nabla^2 \mathbf{H} - \ddot{\mathbf{H}} = \mathbf{0} \tag{2.6}$$

Equation 2.5 indicates a wave equation for the scalar potential, Φ, propagates with longitudinal wave speed $C_p = \sqrt{\frac{\lambda+2\mu}{\rho}}$, whereas Equation 2.6 indicates a wave equation for the vector potential, $\mathbf{H}$, propagates with the shear speed $C_s = \sqrt{\frac{\mu}{\rho}}$. The displacement filed $\mathbf{u}$ can be represented in the full vector form of scalar and vector potential, i.e.,

$$\mathbf{u} = \left(\frac{\partial \Phi}{\partial r} - \frac{\partial H_\theta}{\partial z}\right)\mathbf{e_r} + \left(\frac{\partial H_r}{\partial r} - \frac{\partial H_z}{\partial z}\right)\mathbf{e}_\theta + \left(\frac{\partial \Phi}{\partial z} + \frac{1}{r}\frac{\partial (r H_\theta)}{\partial z}\right)\mathbf{e_z} \tag{2.7}$$

where $\frac{\partial H_r}{\partial r} - \frac{\partial H_z}{\partial z} = 0$, since circular waves are axisymmetric and do not change along with circumference $\left(\frac{\partial}{\partial \theta} = 0\right)$, the displacement filed in tangential direction u_θ is zero. Only two direction displacements (u_r, u_z) are considered in further analysis that requires only two potential functions, Φ and H_θ. The wave Equations 2.5 and 2.6 can be expanded with the Laplacian operator in polar coordinates for scalar Φ and vector H, as shown below:

$$\frac{1}{r}\frac{\partial}{\partial r}\left(r\frac{\partial \Phi}{\partial r}\right) + \frac{\partial^2 \Phi}{\partial z^2} - \frac{1}{C_p^2}\ddot{\Phi} = 0 \tag{2.8}$$

$$\frac{1}{r}\frac{\partial}{\partial r}\left(r\frac{\partial (rH)}{\partial r}\right) + \frac{\partial^2 H}{\partial z^2} - \frac{1}{C_p^2}\ddot{H} = 0 \tag{2.9}$$

The wave potentials Φ and H are harmonic in time t, i.e., $\ddot{\Phi} = -\omega^2 \Phi$ and $\ddot{H} = -\omega^2 H$. The Equations 2.8 and 2.9 solutions could be obtained from Fourier transformation, which may lead to complex formalism due to the axisymmetric. For this problem, Hankel transformation is more suitable, which is represented as Hankel transformation of order ν of a function $g(r)$ as shown below:

$$g(\tilde{\xi}) = \int_0^\infty r g(r) J_\nu(\xi r) dr \tag{2.10}$$

The Hankel transformation of Equations 2.8 and 2.9 are shown below:

$$\begin{aligned} -\xi^2\tilde{\Phi}_{J_0} + \frac{\partial^2\tilde{\Phi}_{J_0}}{\partial z^2} + \frac{\omega^2}{C_p^2}\tilde{\Phi}_{J_0} = 0 \\ -\xi^2\tilde{H}_{J_1} + \frac{\partial^2\tilde{H}_{J_1}}{\partial z^2} + \frac{\omega^2}{C_s^2}\tilde{H}_{J_1} = 0 \end{aligned} \tag{2.11}$$

where $\tilde{\Phi}_{J_0} = \int_0^\infty r\phi(r)J_0(\xi r)dr$ and $\tilde{H}_{J_1} = \int_0^\infty rH(r)J_1(\xi r)dr$ are Hankel transformations of order zero and one for Φ and H, respectively, Equation 2.11 can be rearranged as

$$\begin{aligned} \frac{\partial^2\tilde{\Phi}_{J_0}}{\partial z^2} + \Lambda_p^2\tilde{\Phi}_{J_0} = 0 \\ \frac{\partial^2\tilde{H}_{J_1}}{\partial z^2} + \Lambda_s^2\tilde{H}_{J_1} = 0 \end{aligned} \tag{2.12}$$

where $\xi^2 = \frac{\omega^2}{C_p^2} - \Lambda_p^2$ and $\xi^2 = \frac{\omega^2}{C_s^2} - \Lambda_s^2$, ξ is a wavenumber in the radial direction. The general solution of Equations in 2.12 is given by

$$\begin{aligned} \tilde{\Phi}_{J_0} = C_1 \sin\Lambda_p z + C_2 \cos\Lambda_p z \\ \tilde{H}_{J_1} = C_3 \sin\Lambda_S z + C_4 \cos\Lambda_S z \end{aligned} \tag{2.13}$$

where C_1, C_2, C_3, and C_4 are constants, the Equation 2.13 must be solved for boundary conditions to obtain these constant values. The boundary condition can be obtained from the constitutive law of materials, as explained in Appendix [10]. Therefore, the displacement $\mathbf{u}$ and required stresses to solve constants are shown below after Hankel transformation of displacements u_r and u_z,

$$\begin{aligned} (\tilde{u}_r)_{J_1} = -\xi\tilde{\Phi}_{J_0} - \frac{\partial\tilde{H}_{J_1}}{\partial z} \\ (\tilde{u}_z)_{J_0} = \frac{\partial\tilde{\Phi}_{J_0}}{\partial z} + \xi\tilde{H}_{J_1} \end{aligned} \tag{2.14}$$

and stresses τ_{rz} and τ_{zz},

$$\begin{aligned} (\tilde{\tau}_{rz})_{J_1} = \int_0^\infty r\tau_{rz}J(\xi r)_1 dr = -2\mu\xi\frac{\partial\tilde{\Phi}_{J_0}}{\partial z} - \xi^2\mu\tilde{H}_{J_1} - \mu\frac{\partial^2\tilde{H}_{J_1}}{\partial z^2} \\ (\tilde{\tau}_{zz})_{J_0} = \int_0^\infty r\tau_{zz}J_0(\xi r)dr = -\lambda\frac{\omega^2}{C_p^2}\tilde{\Phi}_{J_0} + 2\mu\frac{\partial^2\tilde{\Phi}_{J_0}}{\partial z^2} + 2\mu\xi\frac{\partial\tilde{H}_{J_1}}{\partial z} \end{aligned} \tag{2.15}$$

where the boundary conditions are $(\tilde{\tau}_{zz})_{J_0}|_{\pm d} = 0$ and $(\tilde{\tau}_{rz})_{J_1}|_{+d} = \tilde{\tau}$ given in Hankel transformation of τ_{rz}. Substituting $\tilde{\Phi}_{J_0}$ and $\tilde{H}_{J_1}$ from Equation 2.13 into Equation 2.15

and after simplification, yields

$$
\begin{aligned}
(\tilde{\tau}_{rz})_{J_1} &= -2\mu\xi\left(C_1\Lambda_p\cos\Lambda_p z - C_2\Lambda_p\sin\Lambda_p z\right) - \mu\left(\xi^2-\Lambda_s^2\right)\left(C_3\sin\Lambda_s z + C_4\cos\Lambda_s z\right)\\
(\tilde{\tau}_{zz})_{J_0} &= \mu\left(\xi^2-\Lambda_s^2\right)\left(C_1\sin\Lambda_p z + C_2\cos\Lambda_p z\right) + 2\mu\xi\left(C_3\Lambda_s\cos\Lambda_s z - C_4\Lambda_s\sin\Lambda_s z\right)
\end{aligned}
\tag{2.16}
$$

Putting boundary conditions into Equation 2.16

$$
\frac{(\tilde{\tau}_{rz})_{J_1}}{\mu}\,|_{z=+d} = -2\mu\xi\left(C_1\Lambda_p\cos\Lambda_p d - C_2\Lambda_p\sin\Lambda_p d\right) - \mu\left(\xi^2-\Lambda_s^2\right)\left(C_3\sin\Lambda_s d + C_4\cos\Lambda_s d\right) \tag{2.17}
$$

$$
\frac{(\tilde{\tau}_{rz})_{J_1}}{\mu}\,|_{z=-d} = -2\mu\xi\left(C_1\Lambda_p\cos\Lambda_p d + C_2\Lambda_p\sin\Lambda_p d\right) - \mu\left(\xi^2-\Lambda_s^2\right)\left(-C_3\sin\Lambda_s d + C_4\cos\Lambda_s d\right) \tag{2.18}
$$

$$
\frac{(\tilde{\tau}_{zz})_{J_0}}{\mu}\,|_{z=+d} = \mu\left(\xi^2-\Lambda_s^2\right)\left(C_1\sin\Lambda_p d + C_2\cos\Lambda_p d\right) + 2\mu\xi\left(C_3\Lambda_s\cos\Lambda_s d - C_4\Lambda_s\sin\Lambda_s d\right) \tag{2.19}
$$

$$
\frac{(\tilde{\tau}_{zz})_{J_0}}{\mu}\,|_{z=-d} = \mu\left(\xi^2-\Lambda_s^2\right)\left(-C_1\sin\Lambda_p d + C_2\cos\Lambda_p d\right) + 2\mu\xi\left(C_3\Lambda_s\cos\Lambda_s d + C_4\Lambda_s\sin\Lambda_s d\right) \tag{2.20}
$$

The above displayed four equations make a 4×4 matrix that can be decomposed into two 2×2 matrices, one for symmetric particle motion and the other for antisymmetric motion. The motion of particles is called the modes, as shown in Figure 2.2 for symmetric and antisymmetric modes, and matrices are mentioned in the next two sections.

2.2.1 Symmetric mode

The symmetric modes are also known as longitudinal modes because the particle motion is primarily in the longitudinal direction below the cutoff frequency. The symmetric mode matrix is shown below, obtained after adding Equations 2.19 and 2.20 and subtracting Equations 2.18 and 2.17.

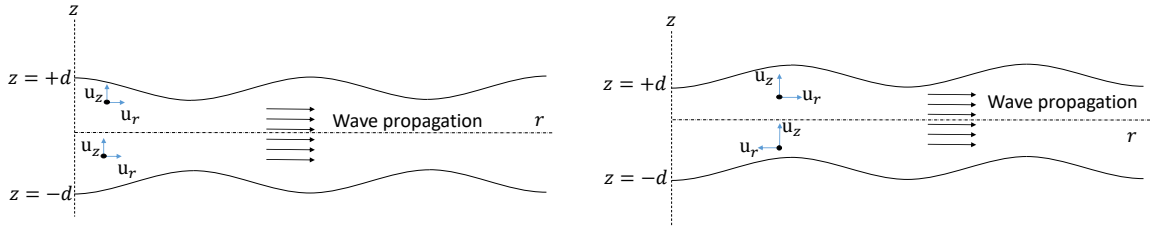

(a) Symmetric mode

(b) Antisymmetric mode

Figure 2.2: Lamb wave modes of symmetric plate.

$$\begin{bmatrix} (\xi^2 - \Lambda_s^2)\cos\Lambda_s d & 2\xi\Lambda_s \cos\Lambda_s d \\ -2\xi\Lambda_p \sin\Lambda_s d & (\xi^2 - \Lambda_s^2)\sin\Lambda_s d \end{bmatrix} \begin{bmatrix} C_2 \\ C_3 \end{bmatrix} = \begin{bmatrix} 0 \\ -\frac{\tilde{\tau}}{2\mu} \end{bmatrix} \tag{2.21}$$

After solving Matrix 2.21 for C_2 and C_3 are expressed below:

$$C_2 = -\frac{2\xi\Lambda_s \cos\Lambda_s d}{D_S}\left(-\frac{\tilde{\tau}}{2\mu}\right) \quad C_3 = \frac{(\xi^2 - \Lambda_s^2)\cos\Lambda_p d}{D_S}\left(-\frac{\tilde{\tau}}{2\mu}\right) \tag{2.22}$$

where $D_S = (\xi^2 - \Lambda_s^2)^2 \sin\Lambda_S d \cos\Lambda_P d + 4\zeta^2\Lambda_P\Lambda_S \sin\Lambda_P d \cos\Lambda_S$.

2.2.2 Antisymmetric mode

The antisymmetric mode is also called a flexural mode because the particle motion is primarily in the transverse direction below the cutoff frequency. Similarly, the antisymmetric mode matrix is shown below, obtained after subtracting Equations 2.19 and 2.20 and adding Equations 2.18 and 2.17.

$$\begin{bmatrix} (\xi^2 - \Lambda_s^2)\sin\Lambda_P d & -2\xi\Lambda_s \sin\Lambda_S d \\ -2\xi\Lambda_p \cos\Lambda_P d & (\xi^2 - \Lambda_s^2)\cos\Lambda_S d \end{bmatrix} \begin{bmatrix} C_1 \\ C_4 \end{bmatrix} = \begin{bmatrix} 0 \\ -\frac{\tilde{\tau}}{2\mu} \end{bmatrix} \tag{2.23}$$

After solving Matrix 2.23 for C_1 and C_4 are expressed below:

$$C_1 = \frac{2\xi\Lambda_s \sin\Lambda_s d}{D_A}\left(-\frac{\tilde{\tau}}{2\mu}\right) \quad C_4 = \frac{(\xi^2 - \Lambda_s^2)\sin\Lambda_p d}{D_A}\left(-\frac{\tilde{\tau}}{2\mu}\right) \tag{2.24}$$

where $D_A = (\xi^2 - \Lambda_s^2)^2 \sin\Lambda_p d \cos\Lambda_s d + 4\xi^2\Lambda_p\Lambda_s \sin\Lambda_s d \cos\Lambda_p d$.

2.2.3 Dispersion curve

The D_S and D_A are called Rayleigh-Lamb wave equations for symmetric and antisymmetric modes. The roots of these transcendental equations are the wavenumber ξ, and D_S roots are represented as ξ_s for symmetric, and D_A roots are denoted as ξ_A for antisymmetric modes. The roots of D_S and D_A bring a relationship between wavenumber ξ and frequency ω or phase velocity C_P and frequency ω, called the dispersion relation. There are infinite wavenumbers (roots) for a given frequency, which satisfies D_S and D_A. However, a finite number of these wavenumbers are purely real and imaginary, while others are complex. The real wavenumbers represent propagating modes, mainly used for SHM applications since they propagate longer distances than imaginary roots. The real roots corresponding ten first modes for both symmetric and antisymmetric are shown in Figure 2.3.

2.2.4 Complete solution of displacement

Once the constants and roots are calculated, then it is straightforward to show the displacement $\mathbf{u}$ of axisymmetric Lamb waves after substituting Equation 2.13 with the value

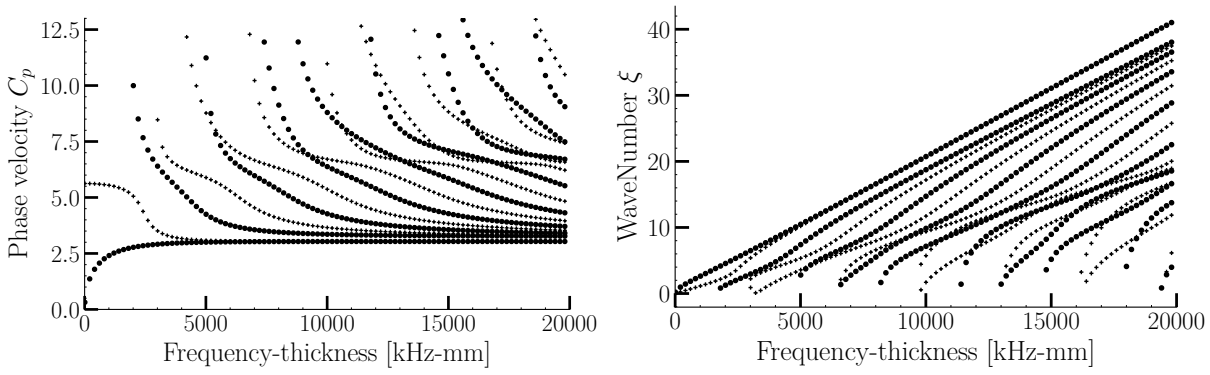

(a) Phase velocity C_p (b) Wavenumber ξ

Figure 2.3: Dispersion curves of an aluminum plate (+ for symmetric and o for anti-symmetric) (a) Phase velocity vs. Frequency-thickness (b) Wavenumber vs. Frequency-thickness.

of the constant into Equation 2.14, which shows

$$(\tilde{u}_r)_{J_1} = -\frac{\tilde{\tau}}{2\mu}\frac{1}{\xi}\left(\frac{N_S}{D_S}+\frac{N_A}{D_A}\right), \quad (\tilde{u}_z)_{J_0} = -\frac{\tilde{\tau}}{2\mu}\frac{1}{\xi}\left(\frac{M_S}{D_S}+\frac{M_A}{D_A}\right) \tag{2.25}$$

where

$$\begin{cases} N_S &= \xi\Lambda_S\left(\xi^2+\Lambda_s^2\right)\cos(\Lambda_P d)\cos(\Lambda_S d) \\ N_A &= -\xi\Lambda_S(\xi^2-\Lambda_s^2)\sin(\Lambda_P d)\sin(\Lambda_S d) \\ M_S &= 2\xi^2\Lambda_s\Lambda_p\cos(\Lambda_s d)\sin(\Lambda_p d)+\xi^2(\xi^2-\Lambda_s^2)\cos(\Lambda_p d)\sin(\Lambda_s d) \\ M_A &= 2\xi^2\Lambda_s\Lambda_p\cos(\Lambda_p d)\sin(\Lambda_s d)+\xi^2(\xi^2-\Lambda_s^2)\cos(\Lambda_s d)\sin(\Lambda_p d) \end{cases}$$

The inverse Hankel transformation can be used to represent displacement Equation 2.25 into the physical domain at d (upper surface) from wavenumber domain ξ. With the help of the residual integral theorem, the radial u_r and transverse u_z displacements can be represented as follows:

$$u_r(r,d)|_{z=d} = -\frac{\pi i}{2\mu}\left[\sum_{\xi_S}\tilde{\tau}(\xi_S)\frac{N_S(\xi_S)}{D'_S(\xi_S)}H_1^1(\xi_S r)e^{-i\omega t}+\sum_{\xi_A}\tilde{\tau}(\xi_A)\frac{N_A(\xi_A)}{D'_A(\xi_S)}H_1^1(\xi_A r)e^{-i\omega t}\right] \tag{2.26}$$

$$u_z(r,d)|_{z=d} = -\frac{\pi i}{2\mu}\left[\sum_{\xi_S}\tilde{\tau}(\xi_S)\frac{M_S(\xi_S)}{D'_S(\xi_S)}H_0^1(\xi_S r)e^{-i\omega t}+\sum_{\xi_A}\tilde{\tau}(\xi_A)\frac{M_A(\xi_A)}{D'_A(\zeta_S)}H_0^1(\zeta_A r)e^{-i\omega t}\right] \tag{2.27}$$

where H_0^1 and H_1^1 Hankel functions are the first type of order zero and one, respectively. The D'_S and D'_A are derivatives of D_S and D_A defined in the above section. However, function $\tilde{\tau}(\xi)$ is a Hankel transformation of circular excitation and is explained in the next section.

2.2.5 Excitation and sensing of axisymmetric Lamb waves

Piezoelectric transducer is widely used in exciting and measuring the guided waves for SHM applications since they are lightweight and inexpensive. Generally, piezoelectric transducers are coupled with elastic structure through an adhesive, as shown in Figure 2.5(a). Upon electric excitation, the piezoelectric transducer undergoes oscillatory contractions and expansions that transfer stress through the adhesive bonding layer to excite guided waves into the structure. Crawley and De Luis [135] first developed an analytical interaction model between piezoelectric transducer and structure. They estimated a uniform strain based analytical equation of stress transmission between piezoelectric transducer and structure. Later on, Giurgiutiu [131] used uniform strain assumption to deduce an analytical expression of stress transmission from the piezoelectric transducer to the structure in the form of interfacial stress for exciting the guided waves for SHM application, as shown below,

$$\tau\left(x\right)=\left(\frac{\Psi}{\Psi+\alpha}\right)\left(\frac{E_p t_p}{a}\right)\varepsilon_{ISA}\frac{\Gamma a}{\cosh\Gamma a}\sinh\Gamma x,\ \text{where}\ \Gamma^2=\frac{G_b}{t_b}\frac{1}{E_a t_a}\frac{\psi+\alpha}{\psi} \tag{2.28}$$

where α is a constant value to describe both longitudinal and bending excitation in the transducer. The E_p and t_p denote the elastic modulus and thickness of the piezoelectric transducer, respectively, while the E and d denote the elastic modulus and thickness of the structure. Similarly, G_b and t_b represent adhesive shear modulus and thickness layer of the adhesive. While $\varepsilon_{ISA}=d_{13}V/t_p$ denotes strain in a piezoelectric transducer, where d_{13} is a piezoelectric coupling effect, and V is applied voltage. The $\psi=Ed/E_p t_p$ represents the stiffness ratio that denotes the maximum fraction of the piezoelectric strain that can be induced. Similarly, Γ denotes the shear lag effect that defines bonding between piezoelectric transducer and structure. As shown in Figure 2.5(b), as the thickness of the adhesive layer t_b decreases, i.e., Γ increases, the stress transmission between the piezoelectric transducer and structure along the radius of the transducer appears at the edge of the transducer. It means that stress transmission can be represented by,

$$\tau(r)=a^2\tau_0\frac{\delta(r-a)}{r} \tag{2.29}$$

where τ_0 is a constant and δ is a Dirac delta function. The Equation 2.29 is assumed to produce surface shear stress with dynamic loading $e^{-i\omega t}$ and generate radial shear stress along its circumference on the plate at the surface $z=d$. It is worth noting that the uniform strain assumption is only appropriate when the thickness ratio (d/t_p) of the structure and the piezoelectric transducer is above six, as shown in Figure 2.5(c). This curve compares bending strain from the uniform and Euler-Bernoulli strain models with varying thickness ratios. The uniform strain model assumes strain in the transducer is uniform regardless of extension and bending in the structure. In contrast, the Euler-Bernoulli strain model assumes that the transducer exhibits linear variation in strain during structural bending, as shown in Figure 2.4. The more details of their formulation is defined in [136].

Nevertheless, the first order Hankel transformation of $\tau(r)$ mentioned in Equation 2.29

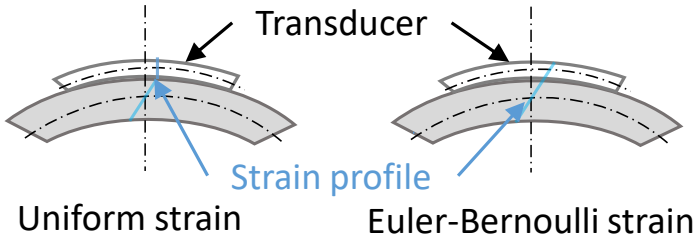

Figure 2.4: Comparison of normalized bending strains from uniform strain model and Euler-Bernoulli strain model.

can be represented as follows,

$$\tilde{\tau}(\xi) = a^2 \tau_0 J_1(\xi a) \tag{2.30}$$

where $\tilde{\tau}(\xi)$ is a Hankel transforms of $\tau(r)$, which can be substituted in Equation 2.25 to obtain the displacement of u_r and u_z. At the same time, the piezoelectric transducer can

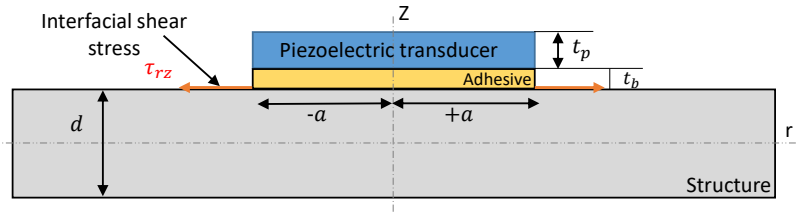

(a)

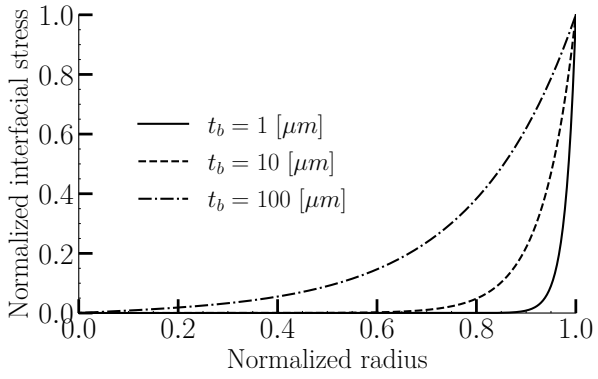

(b) Interfacial shear stress τ_{rr} variation

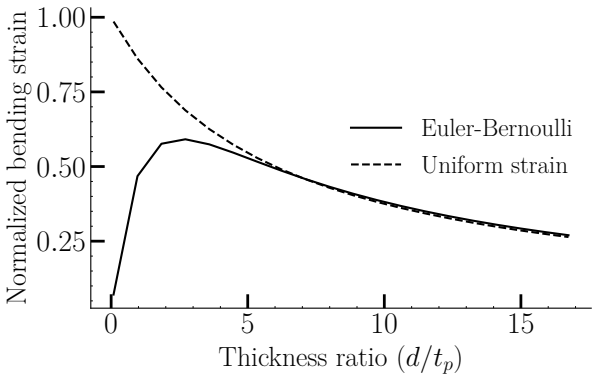

(c) Stiffness ratio ψ

Figure 2.5: (a) Shear layer interaction between piezoelectric actuator and structure (b) Variation of interfacial stress τ_{rz} with the thickness of adhesive t_b (c) Strain assumption in piezoelectric transducer for shear lag solution [136].

sense the guided waves from the structure through an accumulated charge on the surface (integration of electric displacement over a surface). The output can be represented in voltage as follows:

$$V_{out} = \frac{Q_P}{C_P} = S_P \int_A \epsilon_{ii} = S_P \int \int_A \left(\frac{\partial u_r}{\partial r} + \frac{u_r}{r} \right) r dr d\theta \tag{2.31}$$

where S_P is a constant value (assumed one), ϵ_{ii} is a surface strain (sum of ϵ_{rr} and ϵ_θ). Furthermore, A is the surface area of the circular sensor. On simplification of Equation 2.31 after substituting u_r from Equation 2.26 with $\tilde{\tau}(\xi)$ (from Equation 2.30) yields,

$$\begin{aligned} V_{out} = \; & S_P \Big[\textstyle\sum_{\xi_S} J_1(\xi_S a) \frac{N_S(\xi_S)}{D'_S(\xi_S)} \int\int_A \xi_S H_0^2(\xi_S r) r dr d\theta e^{-i\omega t} \\ & + \textstyle\sum_{\xi_A} J_1(\xi_A a) \frac{N_A(\xi_A)}{D'_A(\xi_A)} \int\int_A \xi_A H_0^2(\xi_A r) r dr d\theta e^{-i\omega t} \Big] \end{aligned} \tag{2.32}$$

where H_0^2 is a complex Hankel function of order 0 of the second type.

2.3 Simulation study

A simulation study is performed to compare the theoretical displacement and sensor response, as mentioned in Equations 2.25, 2.30, and 2.32 with a time-domain transient spectral finite element scheme for GWs based SHM implemented recently as the basis of the SHM module of CIVA software. It solves the elastodynamics problem given by,

$$\begin{cases} div(\sigma(u)) - \rho \partial_{tt} u = 0 & \Omega \times \mathbb{R}_+ \\ \sigma(u) n = \tau & \Gamma \times \mathbb{R}_+ \\ u(.,0) = \partial_t u(.,0) = 0 \end{cases} \tag{2.33}$$

Equation 2.33 is a more general representation of Equation 2.1. Where u and ρ are field vector and density, respectively, $\sigma(u) = \mathbb{C}\left(\nabla u + \nabla u^T\right)$ from Hook's law, τ is a surface load with a compact support on $\partial\Omega$, and Ω and Γ are computation and surface load (source) domains, respectively. To solve this, CIVA relies on two approaches: High-order spectral finite elements enabling a parametric meshing procedure based on macro-elements [126], and Pin Force (mentioned in Equation 2.29) approximated piezoelectric transducer model, as a surface load for actuating the GW. The surface load is defined as $\tau(X,d) = p(X)g(d)$, where $p(X)$ is spatial load and $g(t)$ is an actuation signal of sinusoidal tone burst modulated by a Hann window represented in the following mathematical form:

$$g(t) = A \sin(\omega_c t) \left[1 - \tfrac{\cos(\omega_c t)}{N}\right] H\left(\tfrac{2\pi N}{\omega_c} - t\right) \tag{2.34}$$

where N, A, and ω_c denote the number of cycles, signal amplitude, and central frequency, respectively. H is the Heaviside function. To define the surface load τ_{PF} for PF, we obtain the following form:

$$\tau_{PF} = \begin{pmatrix} \bar{\tau}_{rr} \\ \bar{\tau}_{zz} \end{pmatrix} = \begin{pmatrix} g(t)\delta(r-a)/a \\ 0 \end{pmatrix} \tag{2.35}$$

where $\bar{\tau}_{rr}$ and $\bar{\tau}_{zz}$ are surface loads in radial and normal directions, respetively. An aluminum plate of $1000 \times 1000 \times 1.5$ mm^3 is considered in CIVA, as shown in Figure 2.7, where a 5 mm radius circular transducer (actuator) is placed at the center of the plate, and a second similar transducer (receiver) is placed at 100 mm from the actuator. The properties of the aluminum plate and both transducers are shown in Table 2.1. A one-cycle actuation signal is considered with a central frequency of 320 kHz, which excites the

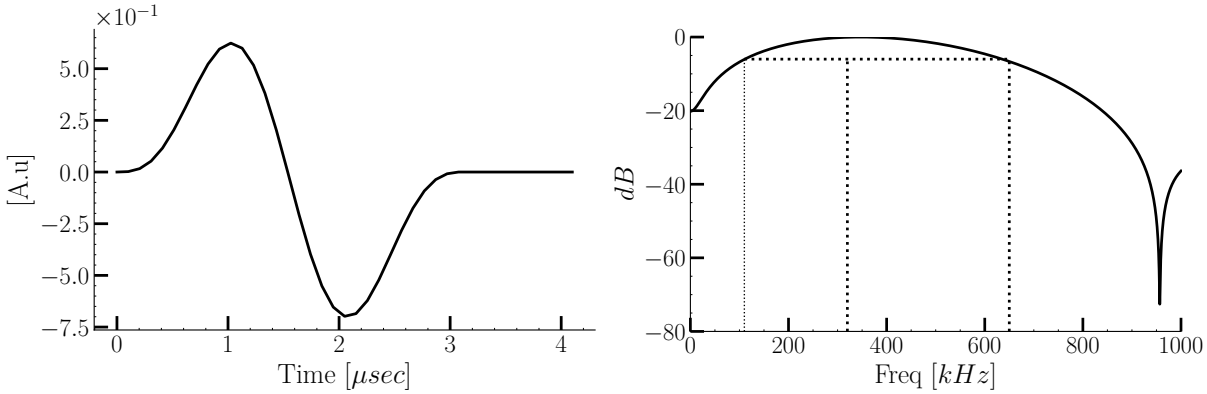

(a) ω_c= 320 kHz with $N = 1$ (b) FFT of excitation signal $g(d)$

Figure 2.6: (a) Excitation signal $g(t)$ and (b) FFT of actuation signal $g(t)$.

Material	E_1 [GPa]	E_2 [GPa]	E_3 [GPa]	ν_{23} -	ν_{13} -	ν_{12} -	ρ [kg m^{-3}]
Aluminum	70	70	70	0.33	0.33	0.33	2700
Adhesive	3.0	3.0	3.0	0.2	0.2	0.2	1600
PZT [137]	120.14	120.41	110.10	0.35	0.35	0.35	7750

Table 2.1: Mechanical properties.

range from 110 kHz to 650 kHz (above 6 dB), as shown in Figure 2.6.

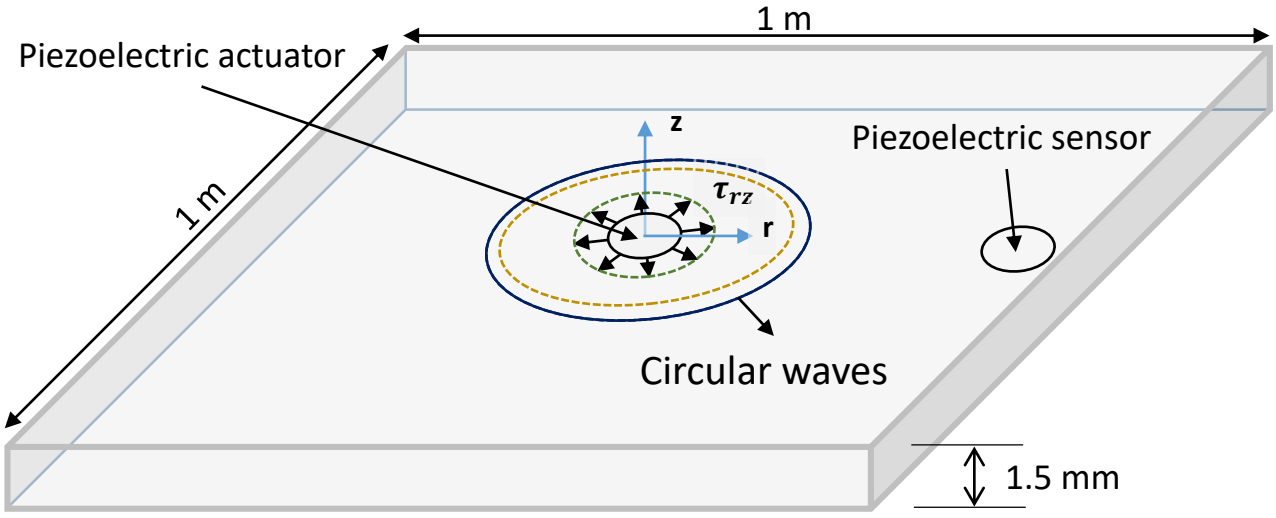

Figure 2.7: A schematic of surface-bonded circular piezoelectric actuator and sensor on the aluminum plate in CIVA.

In order to verify the transduction model, both displacements $u_r(r,d)$ and $u_z(r,d)$ are measured on a line in r-direction (B-scan) from 550 mm to 650 mm with a spacing of 0.5 mm on the top of the surface, as shown in Figures 2.8(a) and 2.8(b). A two-dimension displacement matrix denoted as $U_r(r,d)$ and $U_z(r,d)$ of size (M,N) are formed, where M and N are a number of points in space and time, respectively. The time sampling frequency is 10 MHz. The dispersion curves for both displacements are obtained from

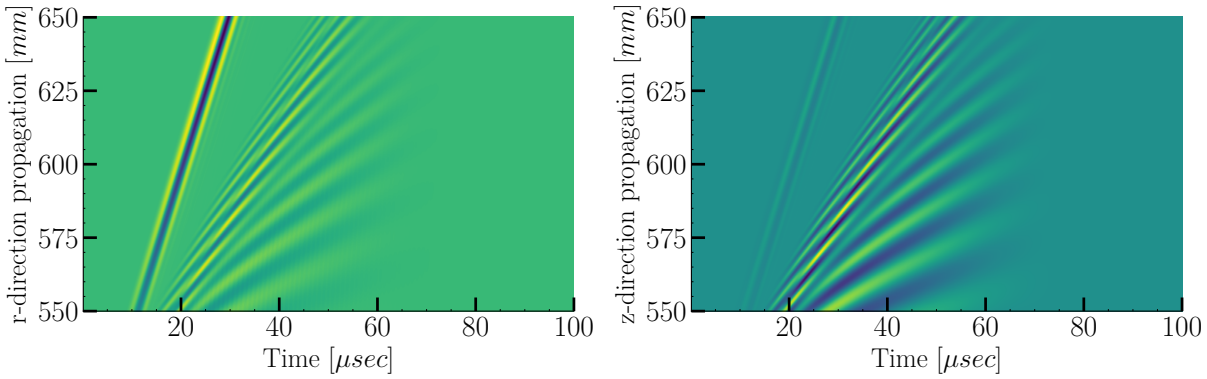

(a) $U_r(r,d)$ (b) $U_z(r,d)$

Figure 2.8: (a,b) Image of B-scan displacement matrix of $U_r(r,d)$ and $U_z(r,d)$.

two dimensional Fourier transformation [138] of the given two displacements matrix, as mentioned below:

$$\bar{U}_r(\xi,\omega) = \int_{-\infty}^{\infty} U_r(r,d)e^{-i(\xi r+\omega t)}drdt$$
$$\bar{U}_z(\xi,\omega) = \int_{-\infty}^{\infty} U_z(r,d)e^{-i(\xi r+\omega t)}drdt$$

The magnitude of $\bar{U}_r(\xi,\omega)$ and $\bar{U}_z(\xi,\omega)$ are represented in Figures 2.9(a) and 2.9(b) with theoretically computed wavenumber and frequency relationship. It exhibits two lower-order modes (S_0 and A_0) and a cut-off frequency of around 1100 kHz for A_1 mode. The amplitude of S_0 and A_0 modes from $|\bar{U}_r(\xi,\omega)|$ and $|\bar{U}_z(\xi,\omega)|$ are compared with the theoretical amplitude response from Equations 2.26 and 2.26. Similarly, the sensor amplitude response in CIVA is compared with theoretical Equation 2.32, as shown in Figures 2.10(a), 2.10(a), and 2.11. It shows that the transduction of waves through the Pin Force actuator model in CIVA correctly measures the wave amplitude from the sensor and both displacements. Note that in the above analysis, we removed the reflection signal from the boundaries in CIVA since the theoretical model is considered infinitely long, meaning that there is no reflection from boundaries. Figures 2.10(a), 2.10(a), and 2.11 are also called excitability curves. From these curves, Lamb waves can be tunned to a particular wave mode at a particular frequency, as mentioned in [131], which becomes very useful in signal processing for SHM in identifying defects or image reconstruction. Tunning of wave modes depends upon parameters such as the radius of a piezoelectric transducer, plate thickness, adhesive thickness, and material properties of both transducer and structure.

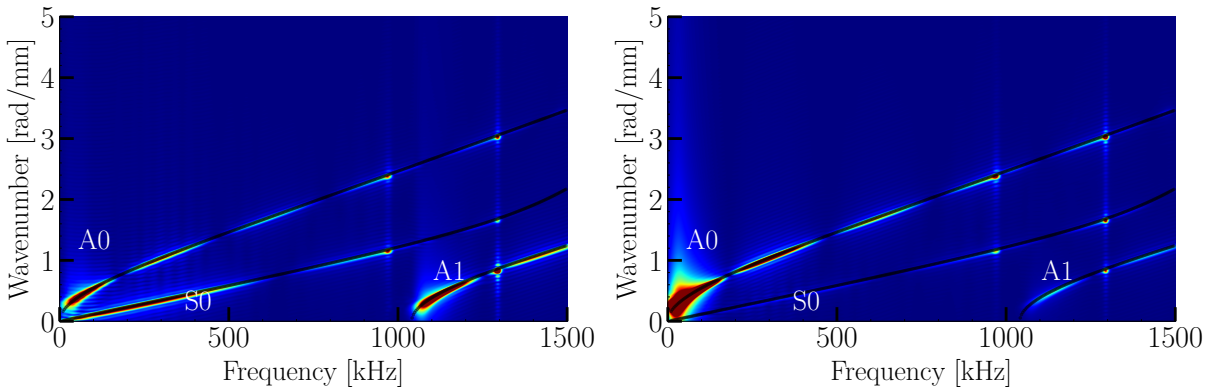

(a) $|\bar{U}_r(\xi,\omega)|$ (b) $|\bar{U}_z(\xi,\omega)|$

Figure 2.9: $|\bar{U}_r(\xi,\omega)|$ and $|\bar{U}_z(\xi,\omega)|$ represented with dispersion curve in (a,b). The black line with points $\circ$ denote the wavenumber computed from D_s and D_A, calculated from the SAFE code.

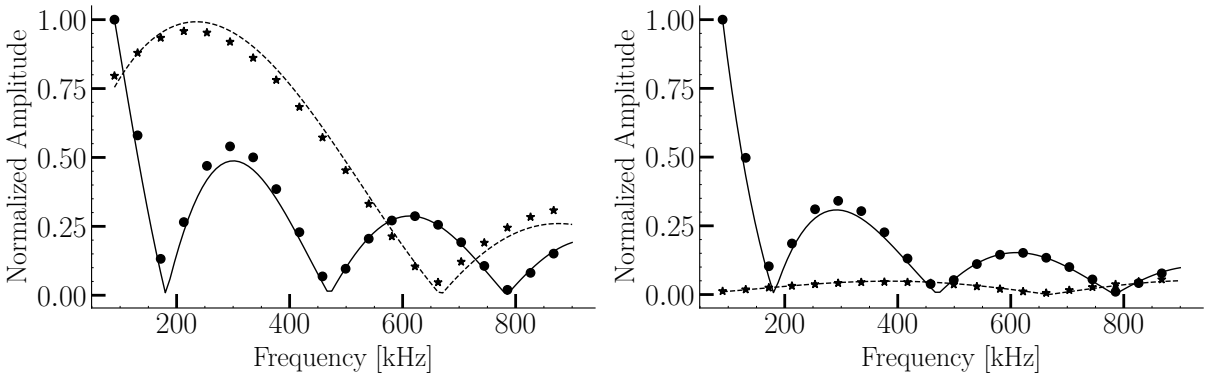

(a) $\max_\omega|\bar{U}_r(\xi,\omega)|$ for $S0$ and $A0$ (b) $\max_\omega|\bar{U}_z(\xi,\omega)|$ for $S0$ and $A0$

Figure 2.10: (a,b) Comparison of amplitude response from $|\bar{U}_r(\xi,\omega)|$ and $|\bar{U}_z(\xi,\omega)|$ of the maximum value for a given frequency ω (denoted as $\star$ points for S_0 and $\circ$ for A_0) with analytical amplitude response from Equations 2.26 and 2.27(denoted as dash line $(--)$ for S_0 and solid line $(-)$ for A_0).

So far, we have verified the PF transduction model in CIVA with the analytical formulation. However, the PF model is limited in excitation frequency, as mentioned in literature [10, 139]. The limitation of the PF model hinges on the selection of thickness ratio of structure to a piezoelectric transducer, adhesive thickness, and material properties. PF assumes that coupled dynamics of transducer (dynamics of the transducer when attached to a structure by an adhesive) are insignificant, which is fulfilled by a thin transducer and minimum adhesive thickness. However, as excitation frequency increases and reaches the nearby foremost electromechanical resonance frequency of the coupled transducer, it begins influencing the GW signals. Experimentally, it becomes cumbersome to follow the assumptions since it is challenging to keep the minimum adhesive thickness between the

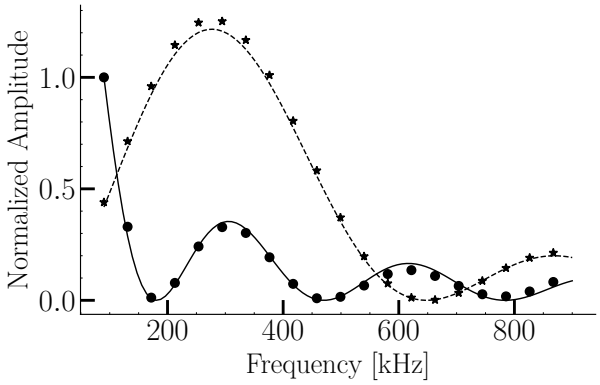

Figure 2.11: Comparison of sensor amplitude response from CIVA (denoted as $\star$ points for S_0 and $\circ$ for A_0) and theoretical Equation 2.32 (denoted as dash line $(--)$ for S_0 and solid line $(-)$ for A_0).

structure and transducer. Therefore, sometimes PF fails far below the first resonance frequency; for example, Quaegebeur et al. [140] have mentioned the 60 kHz upper limit of the PF model validity for their configuration. However this result cannot be directly extrapolated to other configurations. Therefore, in the next section, we have presented the effect on GW signals through the Finite element modeling (FE) of a piezoelectric transducer as the frequency of excitation increases.

2.4 Comparison of PF model and full piezoelectric transducer model

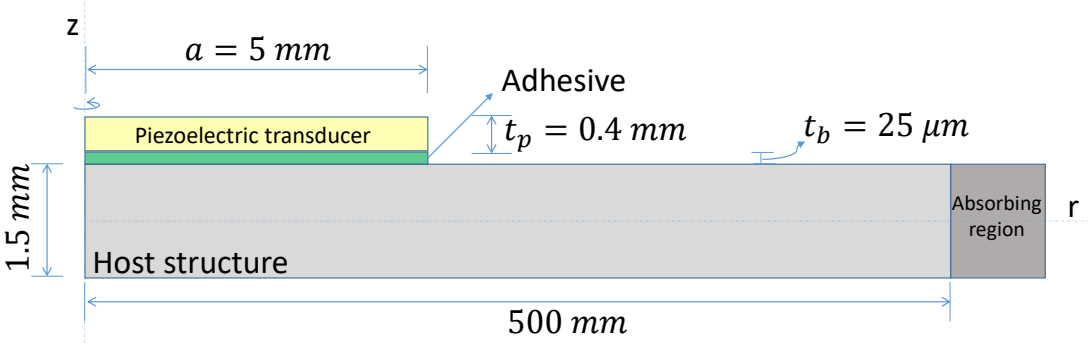

Figure 2.12: 2D axisymmetric configuration in FE.

This section demonstrates the limitations of the PF model with excitation frequency by comparing the Finite element model of an entire piezoelectric transducer. The configuration considered in COMSOL is similar to the one used in the previous section. Since the piezoelectric transducer disc is polarized in the thickness direction and the material properties of the host structure and adhesive are isotropic, an axisymmetric configuration is considered in COMSOL with a 5 mm radius of piezoelectric transducer attached with

an adhesive layer of 25 μm,, as shown in Figure 2.12. This study is performed in the time domain at the four central frequencies of 100, 200, 300, and 500 kHz with five cycles in both simulation devices, while the other conditions are assumed to be the same in both.

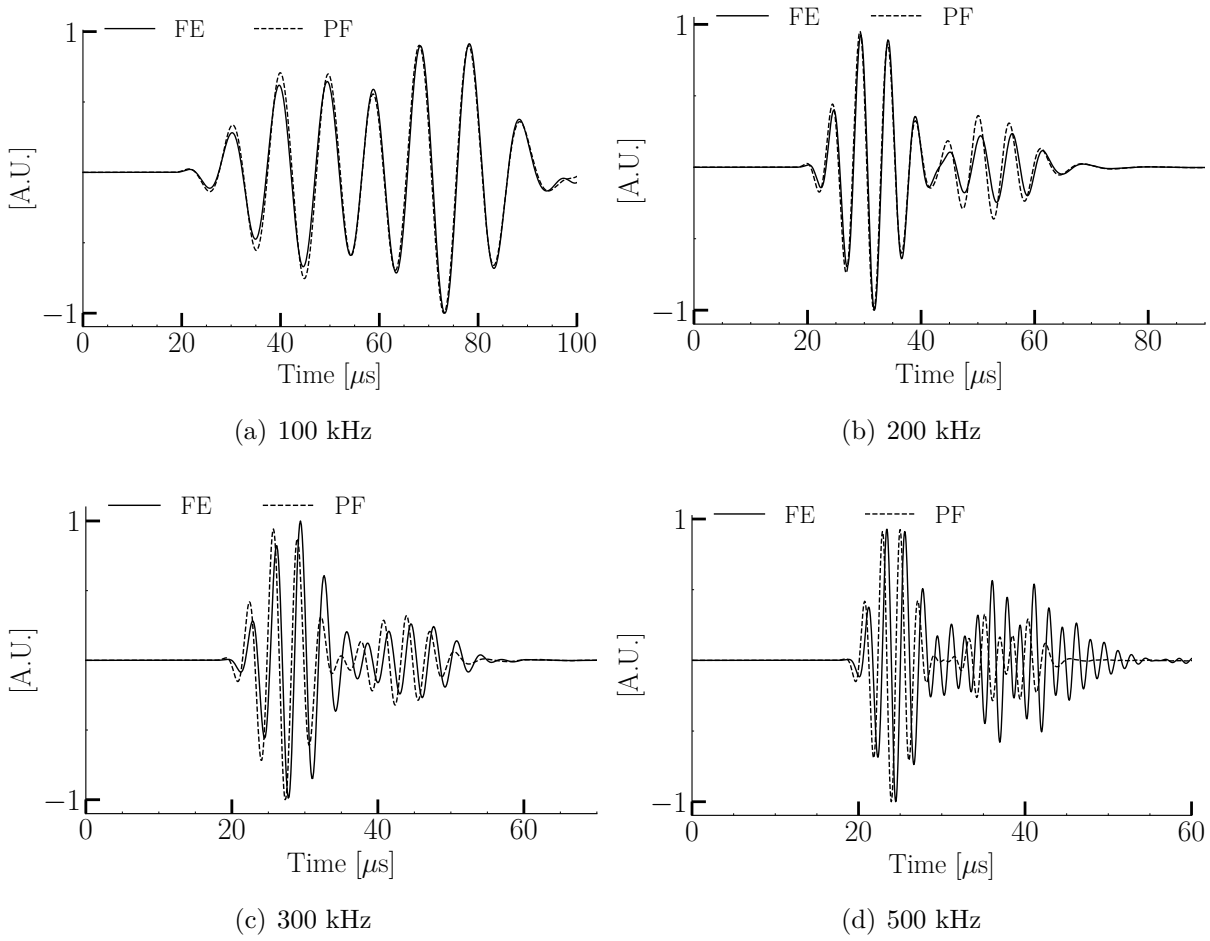

(a) 100 kHz (b) 200 kHz

(c) 300 kHz (d) 500 kHz

Figure 2.13: Time domain signal of u_r comparison between PF and full piezoelectric model in FE at 100, 200, 300, and 500 kHz.

The displacement signals in the radial direction (u_r) are measured corresponding to excitation frequencies at 100 mm from the actuator and compared with the PF model used in CIVA, as shown in Figure 2.13. It can be seen that at 100 kHz, both the PF and FE signals show a good fit, while little change is observed, especially in the A0 mode when the excitation frequency is increased to 200 kHz. Furthermore, at 300 and 500 kHz, the PF model fails to observe phase shifts, amplitude variations, and additional cycles in the signals. It can be seen that considering a complete model of the transducer in FE affects the phase and amplitude of the GWs signals after a specific excitation frequency, as the other conditions were ensured the same in both simulation tools. Therefore, it is concluded with this analysis that we need a new model for modeling high excitation frequencies that are often of practical interest for defect monitoring.

2.5 Conclusion

This chapter presented an introduction to axisymmetric guided waves in isotropic plate-like structures. The PF model, widely used in the literature, has been implemented in CIVA to excite and sense the guided waves. However, the PF model limits the use of a large frequency excitation range in the simulation tool. Therefore, a new transducer model is presented in the next chapter to overcome the limitations of the PF model to allow the use of CIVA simulations in a much broader range of practical applications.

Part I

Transducer model for simulations

CHAPTER 3

Development of hybrid actuator model

Outline

3.1 Introduction

In GWs based SHM, a transducer plays a significant role in exciting and receiving guided waves in a structure. Modeling a piezoelectric transducer coupled with adhesive for GWs based SHM simulation is challenging, except to model the entire configuration with finite element modeling (FE). However, the computational cost associated with fully describing the transducer using finite elements does not allow performing a large number of simulations. Currently, the time-domain transient spectral finite element scheme in CIVA uses an approximate transducer model, i.e., the pin force (PF) model, to account for coupled piezoelectric transducers, as mentioned in the previous chapter. The PF model consists of constant stress traction applied in the radial direction at the periphery of a circular piezoelectric transducer. It relies on two main assumptions: first, the coupling between the transducer and the host structure is ideal (i.e., the adhesive layer is zero thickness). Second, the thickness of the transducer is small compared to the one of the instrumented structure. These assumptions hold at a low-frequency region, i.e., below the first electromechanical resonance frequency of the piezoelectric transducer, due to not considering the dynamics and normal stress of the transducer. Therefore, the constant radial stress traction is limited in excitation frequency [132], which may limit the range of validity and, therefore, the value of the simulation tool for performance demonstrations.

Therefore, this chapter presents a hybrid actuator model that considers frequency-dependent complex stresses in radial and normal directions computed from finite elements. These surface stresses are compatible with the time domain transient spectral finite element schemes without affecting the performances required for intensive simulation campaigns. Simulation and experimental studies are performed in order to validate the proposed approach. A parametric study is performed to quantify the hybrid actuator model's validity in a large range of excitation frequencies. It is shown that the proposed hybrid actuator model accurately models the transduction signal above the first free electromechanical resonance frequency of a piezoelectric transducer.

This chapter is organized as follows. Section second presents state-of-the-art piezoelectric transducer modeling for GWs based SHM simulations. Section three describes the formulation of the proposed hybrid actuator model. Finally, the fourth section presents the numerical and experimental validation of the proposed model and discusses the validity limits.

3.2 State of the art of circular piezoelectric transducer modeling for GWs based SHM

The main challenge in GWs based SHM transducer modeling is the coupling of the transducer to the host structure through an adhesive layer. This has been addressed to a certain extent by the shear lag solution of the interfacial stress between the transducer and host structure. Crawley and De Luis [135, 136] were the first to introduce the shear lag solution where, as the thickness of the adhesive decreases and the stiffness ratio between the host structure and the transducer increases, the interfacial stress transfer is

focused at the circumference of the transducer. Since then, many shear lag formulations have been proposed [141–144], particularly in the modeling of the transducer coupling to the host structure. However, these models are primarily suitable for a directional wavefield (e.g., from a rectangular transducer), where the wavefield propagates mainly in one or two directions. However, to ensure large area cover, omnidirectional transducers are used in general [145]. The following section contains some notable articles on the circular piezoelectric transducer modeling for GWs based SHM.

3.2.1 Pin force model

Giurgiutiu [131] studied the coupling of one piezoelectric transducer to a host structure through an adhesive layer and introduced the PF model. The PF model is an idealized model under the assumptions of zero adhesive thickness and negligible transducer thickness. As the thickness of the adhesive decreases, the interfacial stress between the circular piezoelectric transducer and the host structure is concentrated at the edges of the piezoelectric transducer [10]. This interfacial stress is represented by $\bar{\tau}_{rr} = \tau_0 \delta(r-a)/a$, where a is the radius of a transducer, and τ_0 is a constant. Therefore, it can readily be applied as a traction boundary condition in order to obtain the dynamic response of the GWs based SHM [117]. The PF surface load τ_{PF} is defined as:

$$\boldsymbol{\tau}_{PF}(r,t) = \begin{bmatrix} \bar{\tau}_{rr}(r,t) \\ \bar{\tau}_{zz}(r,t) \end{bmatrix} = \begin{bmatrix} g(t)\delta(r-a)/a \\ 0 \end{bmatrix} \tag{3.1}$$

where $\bar{\tau}_{rr}$ and $\bar{\tau}_{zz}$ are surface loads in radial and normal directions, respectively.

However, the PF model assumes a static interfacial stress between the transducer and host structure and does not consider the transducer frequency dependent behavior and the adhesive thickness. Thus, it should be noted that the PF model is limited in terms of the excitation frequency and the transducer size [139].

3.2.2 Lamb wave tuning curve model

Sohn and Lee [146] improved the PF model by introducing two calibration methods for the excitability curve of the transducer in order to expand the validity range of the model. The first method is an amplitude adjustment based on the frequency dependent strain energy distribution in the host structure. The second method is the effective area calculation of the circular piezoelectric transducer based on the linear admittance ratio of the bonded and unbonded transducer. This is equivalent to reducing the transducer's effective area. For example, in [146], the effective area of a transducer is 59% of the original area of the given transducer at the excitation frequency of 250 kHz. This model takes into account the adhesive effect and provides limited improvement to the excitability curve. However, the calibrated PF model does not consider the normal stress between the transducer and host structure, as well as the frequency-dependent behavior of the transducer, as mentioned in [146].

3.2.3 Hybrid-empirical sensor model

Quaegebeur et al. [140] proposed a variable separation method for hybrid sensor modeling with an empirical calibration of the transducer dynamics estimation using FE computation and transducer impedance. The transducer stresses are computed in both radial and normal directions, which becomes essential as the excitation frequency increases. Therefore, this model proposes bi-direction complex load functions with six hyperparameters. These hyperparameters are computed by best fitting the complex stress distribution computed by FE over the proposed analytical traction functions. This hybrid model is validated below the second electromechanical resonance frequency of the transducer. However, this model is limited to specific values for the thickness ratio, frequency range, wavenumber, and host structure properties. For every new configuration, expensive calibration and validation steps are required.

3.2.4 Equivalent pin force model

Li et al. [147] proposed a two directions equivalent pin force model. This model is similar to the hybrid-empirical sensor model mentioned in the previous section. However, it is applied in the Laplace domain on a boundary element formulation to model the S_0 and A_0 modes below the first cutoff frequency. This model computes the radial and normal tractions from FE and then projects them to the S_0 and A_0 modes using an integral transformation. This model is validated up to 300 kHz frequency in the configuration of the paper.

Hybrid-empirical sensor and equivalent pin force models are applied in simulations in which the mode decomposition of GWs are possible. These models are hence not suitable for a 3D time domain spectral finite element method with no possibility of mode decomposition, which is why a new model is presented in this chapter. To discuss the results, the proposed model is compared to the PF model, i.e., the most widely used model in the literature.

3.3 Theoretical framework for the hybrid actuator model

3.3.1 Hybrid actuator model (HAM)

The stress between a transducer and a structure is made of radial and normal components, as shown in the Figure 3.1. The stress distributions vary with the frequency, and as mentioned in the previous subsections 3.2.3 and 3.2.4, the normal component increases with the excitation frequency. These stresses are assumed omnidirectional:

$$\begin{aligned} \bar{\tau}_{rr}(r,\omega) &= \widetilde{\tau}_{rr}(\omega)\delta(r-a_e^{rr})/a_e^{rr} \\ \bar{\tau}_{zz}(r,\omega) &= \widetilde{\tau}_{zz}(\omega)\delta(r-a_e^{zz})/a_e^{zz} \end{aligned} \tag{3.2}$$

where $\widetilde{\tau}_{rr}(\omega)$ and $\widetilde{\tau}_{zz}(\omega)$ capture the frequency dependent behavior of the transducer in radial and normal directions, respectively, $\bar{\tau}_{rr}(r,\omega)$ and $\bar{\tau}_{zz}(r,\omega)$ are complex loads in radial

and normal directions, and a_e^{rr} and a_e^{zz} are effective radii of the transducer in radial and normal directions. In this study, finite elements are used to pre-compute the complex stress

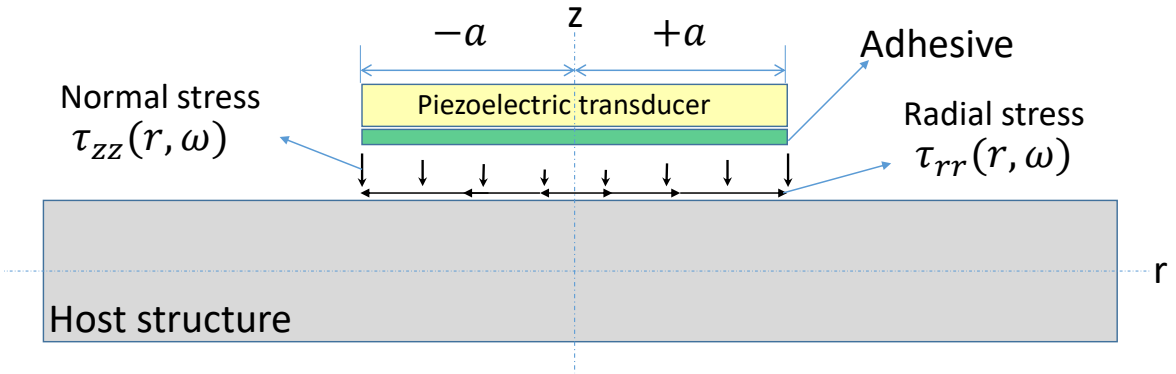

Figure 3.1: Side view of a circular piezoelectric transducer attached through an adhesive layer to a host structure. Radial $\tau_{rr}(r,\omega)$ and normal stresses $\tau_{zz}(r,\omega)$ under the transducer are shown by the black arrows.

distributions under the transducer in the normal $\tau_{zz}(r,\omega)$ and radial $\tau_{rr}(r,\omega)$ directions for a given excitation frequency ω as shown in Figure 3.1 and described in the following section. The HAM assumes that the effect of the loads in Equation 3.2 are the same as the effect of the stresses obtained from finite elements. Therefore:

$$\begin{aligned}\int_0^a \widetilde{\tau}_{rr}(\omega)\frac{\delta(r-a_e^{rr})}{a_e^{rr}}2\pi r\,\mathrm{d}r &= \int_0^a \tau_{rr}(r,\omega)2\pi r\,\mathrm{d}r \\ \int_0^a \widetilde{\tau}_{zz}(\omega)\frac{\delta(r-a_e^{zz})}{a_e^{zz}}2\pi r\,\mathrm{d}r &= \int_0^a \tau_{zz}(r,\omega)2\pi r\,\mathrm{d}r\end{aligned} \tag{3.3}$$

This leads to:

$$\begin{aligned}\widetilde{\tau}_{rr}(\omega) &= \int_0^a \tau_{rr}(r,\omega)r\,\mathrm{d}r \\ \widetilde{\tau}_{zz}(\omega) &= \int_0^a \tau_{zz}(r,\omega)r\,\mathrm{d}r\end{aligned} \tag{3.4}$$

The effective radius in the radial direction is estimated from the admittance ratio of the bonded (Y_{bonded}) and unbonded (Y_{unbonded}) transducers by,

$$a_e^{rr} = \sqrt[2]{\left[\frac{Y_{\text{bonded}}}{Y_{\text{unbonded}}}\right]}a \tag{3.5}$$

The effective radius in the normal direction is chosen such that $a_e^{zz} = 0.99 \times a_e^{rr}$, based on [140], where the ratio between normal and radial radii is 0.99. This value has been proven effective in the configurations and validations presented hereafter but this parameter might be adjusted accordingly in other cases.

To obtain the surface load to apply in HAM, the Fourier transform of the excitation function $\widetilde{g}(\omega)$ is multiplied by the frequency-dependent behavior terms, leading to two

modified frequency domain actuation signals in radial $\widetilde{S}_{rr}(\omega) = \widetilde{g}(\omega)\widetilde{\tau}_{rr}(\omega)$ and normal $\widetilde{S}_{zz}(\omega) = \widetilde{g}(\omega)\widetilde{\tau}_{zz}(\omega)$ directions. The inverse Fourier transformation then leads to the modified actuation signals $S_{rr}(t)$ and $S_{zz}(t)$ in the time domain:

$$\tau_{HAM}(r,t) = \begin{bmatrix} \bar{\tau}_{rr}(r,t) \\ \bar{\tau}_{zz}(r,t) \end{bmatrix} = \begin{bmatrix} S_{rr}(t)\delta(r-a_e^{rr})/a_e^{rr} \\ S_{zz}(t)\delta(r-a_e^{zz})/a_e^{zz} \end{bmatrix} \tag{3.6}$$

3.3.2 Computation of the dynamic behavior of the transducer

Recently, Kapuria et al. [148] have analytically estimated the complex stress distribution of a transducer as a function of the frequency; however, this model is not applicable to a circular transducer. Therefore to pre-compute the $\tau_{rr}(r,\omega)$ and $\tau_{zz}(r,\omega)$, this study uses COMSOL Multiphysics. Since the transducer is polarized in the thickness direction and

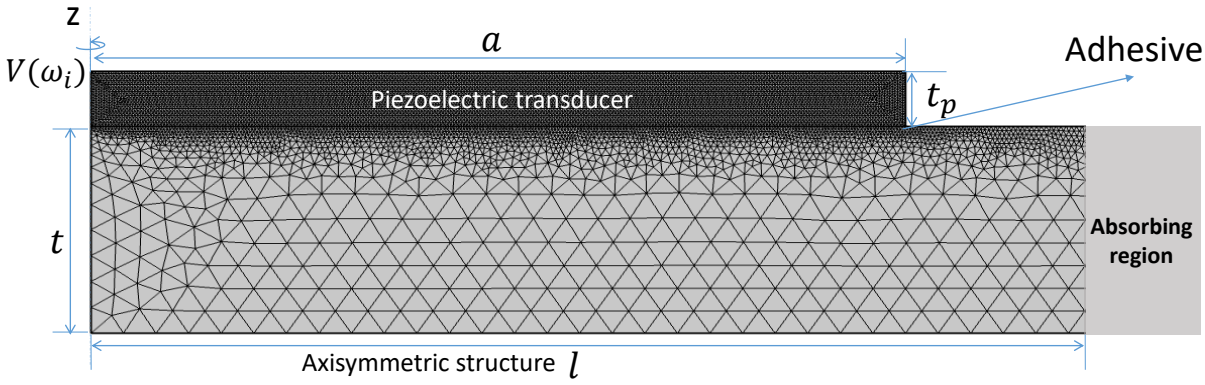

Figure 3.2: Scheme of a 2D axisymmetric finite element model to compute the frequency dependent behavior of the transducer.

the material properties of the structure and the adhesive are isotropic, a 2D axisymmetric model is considered to compute the stress distribution under the transducer, as shown in Figure 3.2. A thin elastic layer condition is assumed between the transducer and the host structure to model the adhesive layer with a normal (k_n) and tangential (k_t) stiffnesses as follows:

$$k_n = \frac{E_a(1-\nu_a)}{h_a(1+\nu_a)(1-2\nu_a)}, \qquad k_t = \frac{E_a}{2h_a(1+\nu_a)}$$

where E_a, ν_a, and h_a are the elastic modulus, Poisson's ratio, and thickness of the adhesive, respectively. The mesh is defined with 15 elements per wavelength of the mode with the smallest wavelength and free quadratic triangles are used. A local refinement of mesh is made around the transducer to extract the stresses under the transducer. The absorbing region (AR) is used to avoid the reflection from the boundaries as defined in [149]. The frequency-domain analysis is computed on a desktop computer in a few minutes, and the complex stresses ($\tau_{rr}(r,\omega)$and$\tau_{zz}(r,\omega)$) under the transducer are extracted at every excitation frequency ω for an applied voltage $V(\omega)$. These complex stresses are then used in Equation 3.4.

3.4 Validation

Two configurations denoted C1 and C2, shown in Table 3.1, are studied for the validation of the HAM. Each is an isotropic aluminum plate with a permanently bonded piezoelectric transducer in its center. To ensure a relatively large validation range, distinct elastic and piezoelectric properties, dimensions, and coupling conditions are studied. The host structure, piezoelectric transducer, and adhesive properties for both configurations are mentioned in Tables 3.2 and 3.3. Additionally, the adhesive damping values for C1 and C2 are used as 0.05 and 0.018 [140], respectively. The energy velocity curves for both

Configuration	Plate size $(l \times w \times t)$ [mm^3]	Piezoelectric transducer size $(a \times t_p)$ [mm^2]	Adhesive thickness (h_a) [µm]
C1	600 × 600 × 1.5	5 × 0.4	25
C2	1200 × 1200 × 3	5 × 0.4	100

Table 3.1: Dimensions of C1 and C2.

Material	E_1 [GPa]	E_2 [GPa]	E_3 [GPa]	ν_{23} -	ν_{13} -	ν_{12} -	ρ [kg m^{-3}]
Aluminum-C1	70	70	70	0.33	0.33	0.33	2700
Adhesive-C1	3.0	3.0	3.0	0.2	0.2	0.2	1600
PZT-C1 [137]	120.14	120.41	110.10	0.35	0.35	0.35	7750
Aluminum-C2	75	75	75	0.33	0.33	0.33	2660
Adhesive-C2	3.1	3.1	3.1	0.4	0.4	0.4	1600
PZT-C2 [150]	112.14	112.41	86.10	0.35	0.35	0.35	7900

Table 3.2: Mechanical properties.

Material	d_{31} $\times 10^{-12}$ [m V^{-1}]	d_{33} $\times 10^{-12}$ [m V^{-1}]	ϵ_{11}/ϵ_0 -	ϵ_{22}/ϵ_0 -	ϵ_{33}/ϵ_0 -
PZT-C1 [137]	-1.71	3.74	1730	1730	1700
PZT-C2 [150]	-1.40	3.20	1475	1475	1250

Table 3.3: Electrical properties of piezoelectric transducer. The electrical permittivity of air $\epsilon_0 = 8.854 \times 10^{-}12$ F m^{-1}.

configurations are shown in Figure 3.3, in which it is visible that the first cutoff frequency is approximately 1.1 MHz for C1 and 550 kHz for C2.

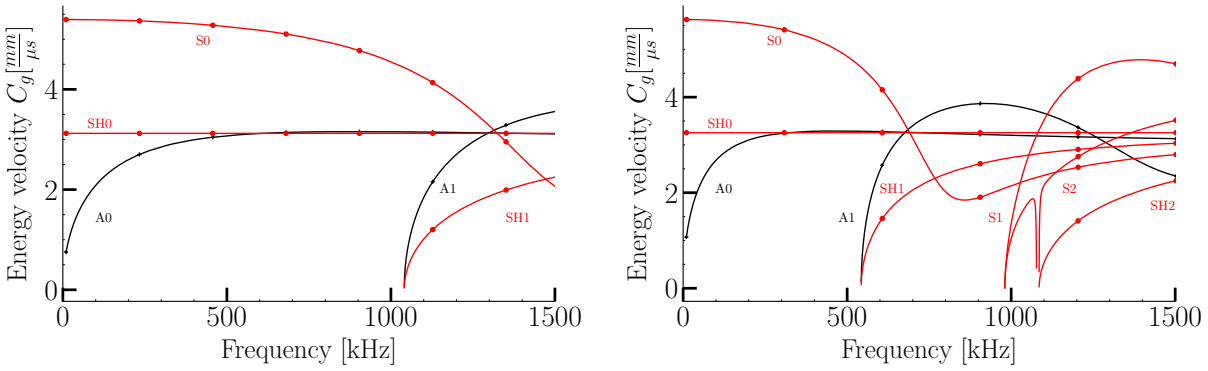

(a) C1 (b) C2

Figure 3.3: Energy velocity dispersion curves for (a) C1 and (b) C2.

3.4.1 Computation of the frequency-dependent behavior terms of the piezoelectric transducer

The requirement for the HAM is to pre-compute the frequency-dependent behavior terms of the piezoelectric transducer in radial $\widetilde{\tau}_{rr}(\omega)$ and normal $\widetilde{\tau}_{zz}(\omega)$ directions, as well as the effective radius of the transducer over the entire range of excitation frequency, thus allowing the computation of the loads defined in Equation (3.2). The stress distributions $\tau_{rr}(r,\omega)$ and $\tau_{zz}(r,\omega)$ are estimated based on section 3.3.2 for both configurations. After that, the frequency-dependent behavior terms for configurations C1 and C2 are estimated through Equation (3.4), where the numerical computation is performed from 30 kHz to 1000 kHz with a 5 kHz step. The results are plotted in Figure 3.4.

For configuration C1, the normal stress $\widetilde{\tau}_{zz}(\omega)$ is near zero until 250 kHz and increases to be equal to the radial stress $\widetilde{\tau}_{rr}(\omega)$ at 550 kHz. In contrast, radial stress grows linearly and shows a local maximum at 300 kHz. Similarly, for configuration C2, radial stress exhibits a similar trend to C1 with higher values. The normal component is near zero up to 150 kHz and shows a local maximum at 300 kHz. The local maximum in both configurations is observed due to the first electromechanical resonance of the coupled piezoelectric transducers, as shown in Figures 3.5(a) and 3.5(b). Hence, the modeling of the normal stress becomes necessary at high excitation frequencies, i.e., around 300 to 500 kHz in the cases under consideration.

The effective radii of the transducers, shown in Figures 3.5(c) and 3.5(d), are computed based on the ratio of the slopes at $f = 0$ kHz of admittances of the bonded and unbonded transducers. The slope at the origin is computed by a linear fit of the admittance up to 140 kHz to ensure a regression coefficient around 0.99, as shown in Figures 3.5(a) and 3.5(b). It can be observed that, as the excitation frequency increases, the effective radius decreases, therefore, it is required to compute Equation (3.2) at every excitation frequency. The estimated loads are then applied as a surface load in the time domain spectral finite element schemes, with frequency dependent support.

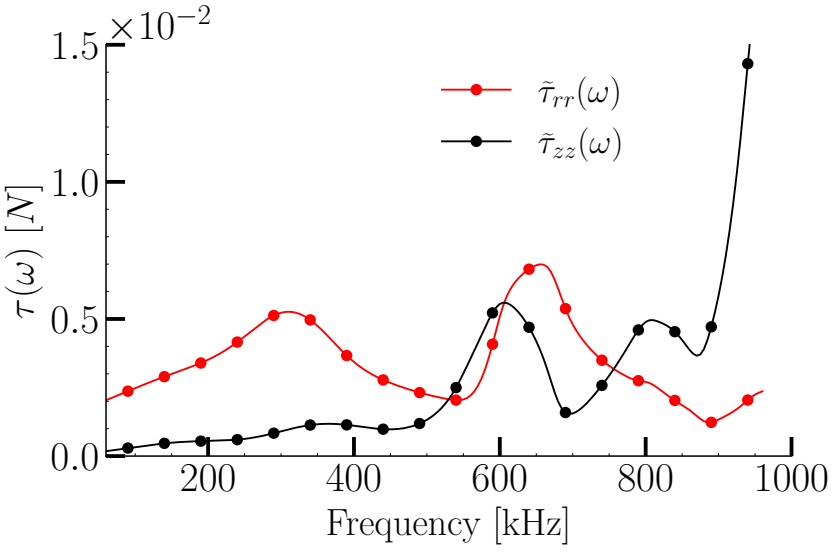

(a)

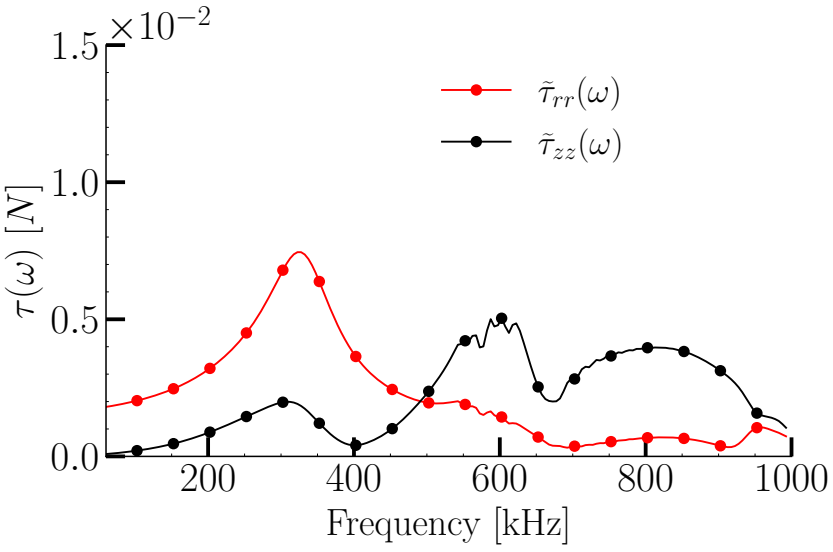

(b)

Figure 3.4: Frequency-dependent behavior terms for configurations (a) C1 and (b) C2.

3.4.2 Validation with simulations

This section compares the radial U_{rr} and transverse U_{zz} displacements computed by finite elements for two transducer models: PF and HAM. A 2D axisymmetric model is used to compute the FE time domain displacement signal. The computed loads from the previous section are imported into the full 3D spectral finite element model implemented in CIVA.

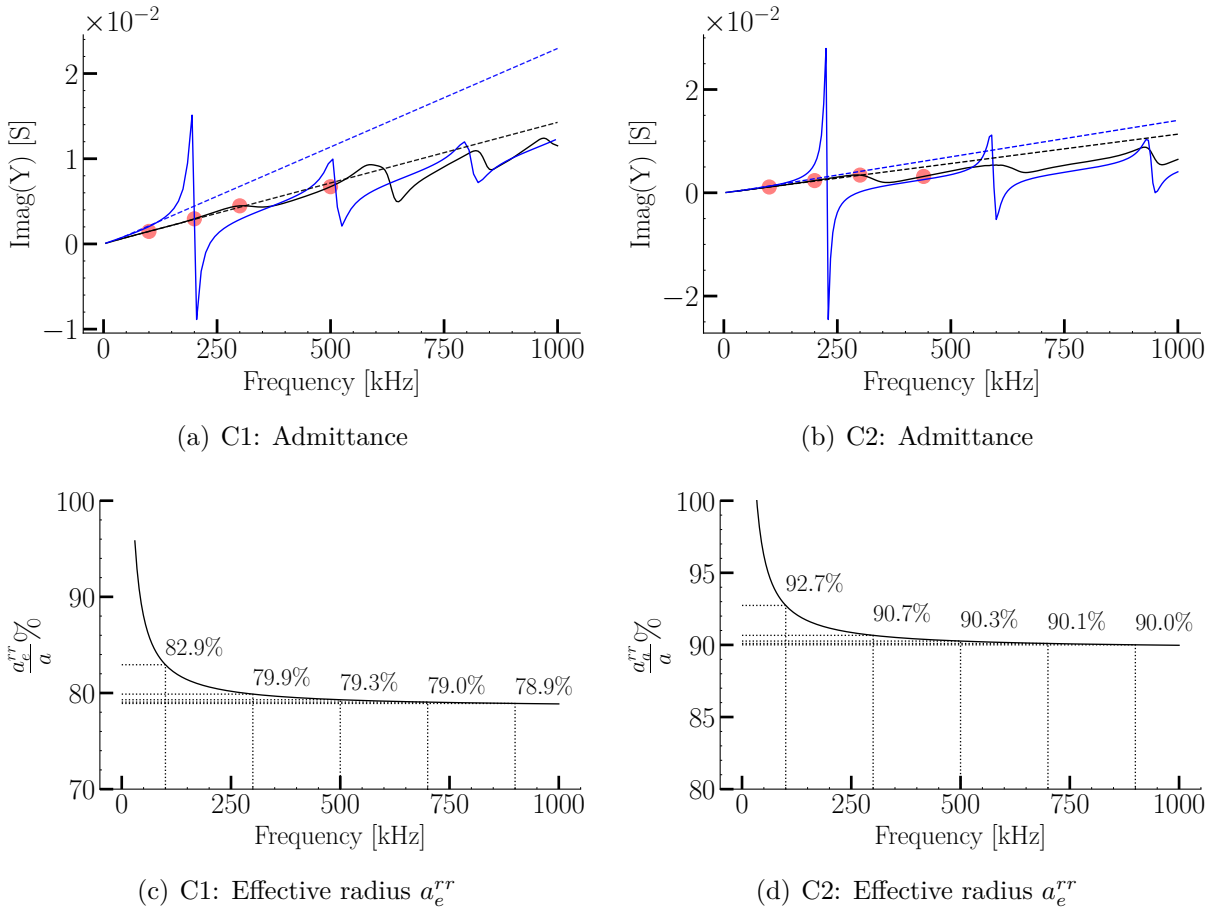

(a) C1: Admittance

(b) C2: Admittance

(c) C1: Effective radius a_e^{rr}

(d) C2: Effective radius a_e^{rr}

Figure 3.5: (a,b) The imaginary part of the admittance for bonded (black line) and unbonded (blue line) piezoelectric transducers obtained from finite element simulations and their linear fit (dashed line) and (c,d) ratio of the effective radius to the physical radius a of the piezoelectric transducer.

The excitation function is a 5-cycle sinusoidal tone burst described as:

$$g(t) = A\sin(\omega_c t)\left[1 - \frac{\cos(\omega_c t)}{N}\right] H\left(\frac{2\pi N}{\omega_c} - t\right),$$

where N, A, and ω_c denote the number of cycles, signal amplitude, and central frequency, respectively, while H is the Heaviside function.

The normalized displacements in both directions at 100 mm from the transducer are shown in Figures 3.6 and 3.7 for C1 and Figures 3.8 and 3.9 for C2. The first two signals are shown at 100 and 200 kHz, i.e., below the transducers first electromechanical resonance. In the other two displacement signals, the first signal is shown at the first resonance frequency of 300 kHz for both configurations, and the second is shown at 500 kHz for C1, i.e., at the second resonance frequency and 440 kHz for C2 near the second resonance frequency. The selected frequency locations are shown with the red circles in Figures 3.5(a) and 3.5(b).

For C1 at 100 and 200 kHz, both PF and HAM concur with the finite element results,

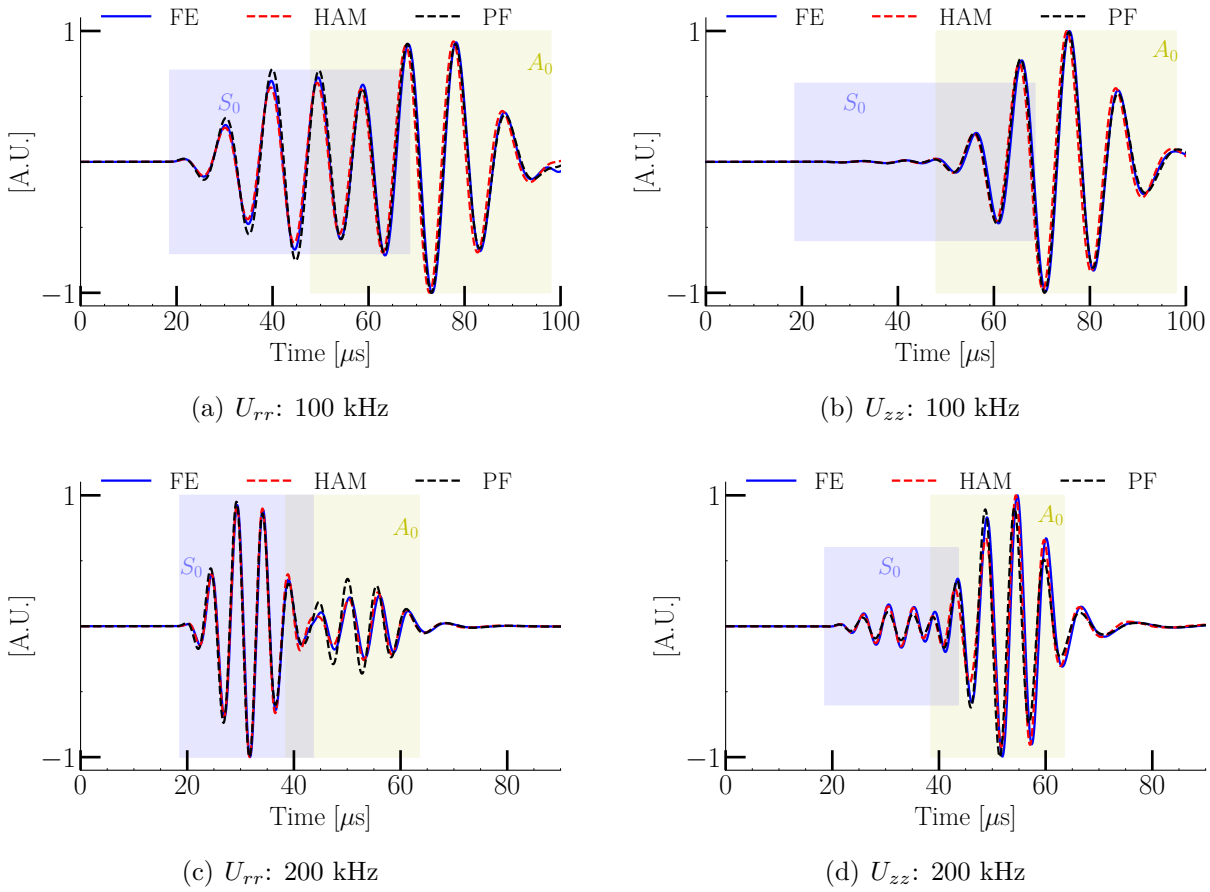

(a) U_{rr}: 100 kHz

(b) U_{zz}: 100 kHz

(c) U_{rr}: 200 kHz

(d) U_{zz}: 200 kHz

Figure 3.6: Comparison of displacement signals (U_{rr} and U_{zz}) computed from FE, PF, and HAM for C1 at 100 mm.

as shown in Figures 3.6(a) to 3.6(d). This is due to the fact that up to 200 kHz, the normal stresses are nearly zero, as shown in Figure 3.4(a); therefore, the PF assumptions remain valid. Furthermore, at 300 and 500 kHz (shown in Figures 3.7(a) to 3.7(d)), phase and amplitude differences are observed between the FE and the PF. At the same time, the HAM model captures these variations effectively. It is also noted that at 500 kHz, the A_0 mode is longer than 5 cycles, due to the high admittance value, leading to a local resonance phenomenon. Similar conclusions can be made for C2 at 100 and 200 kHz, as shown in Figures 3.8(a) to 3.8(d). The same variations between the signals obtained with PF and the finite elements are observed at 300 kHz and 440 kHz, as shown in Figures 3.9(a) to 3.9(b). In contrast to PF, HAM captures the phase-amplitude variations considerably well at 300 kHz. However, little phase and amplitude variations are observed at 440 kHz in the HAM result compared to the finite element results. It should be noted that the bandwidth centered on 440 kHz goes from 300 to 600 kHz, meaning that the first cutoff frequency of C2 is excited. In this case, the assumption of spatial and frequency independence (Equation (3.2)) is inadequate. Additionally, the signal at 500 kHz for C2 is added to highlight the limits of the model in Figures 3.9(e) and 3.9(e). In this case, the match between both models and the FE signals is poor because the excitation bandwidth at

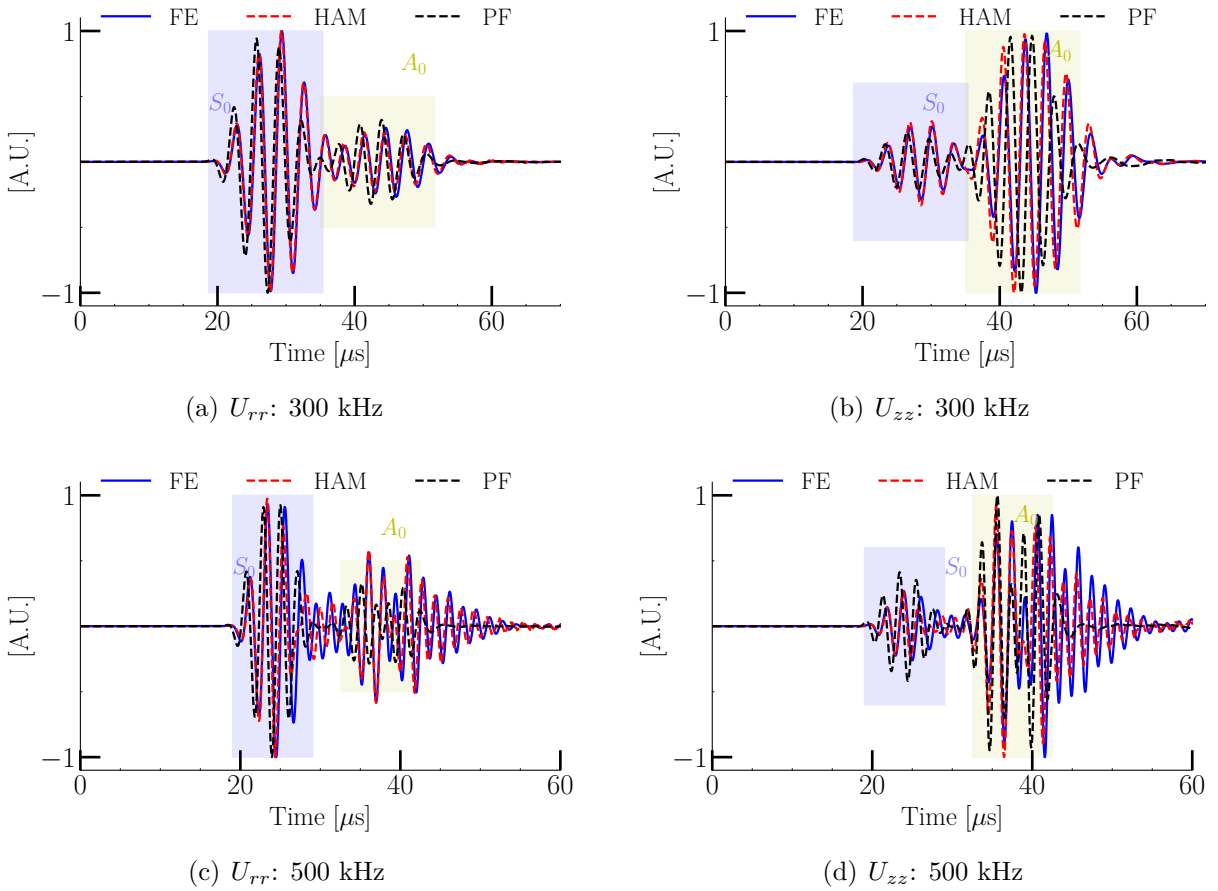

(a) U_{rr}: 300 kHz

(b) U_{zz}: 300 kHz

(c) U_{rr}: 500 kHz

(d) U_{zz}: 500 kHz

Figure 3.7: Comparison of displacement signals (U_{rr} and U_{zz}) computed from FE, PF, and HAM for C1 at 100 mm.

ranges from 350 to 700 kHz, thus exciting multiple modes, including A_1 with zero velocity, as shown in Figure 3.3(b). Moreover, the S_0 mode group velocity also drastically changes from 5 to 2 $mm/\mu s$, meaning that the S_0 mode is highly dispersive and is superimposed with other modes. Therefore, locating the modes and transducer effect is impossible. Nevertheless, HAM is in phase with FEM results, whereas PF is out of phase.

Hence, this simulation study shows that the frequency-dependent behavior term affects the propagated wavepackets in terms of both phase and amplitude. Particularly, additional cycles are observed when an electromechanical resonance is excited. The HAM successfully reproduces these phenomena while the PF does not.

3.4.3 Experimental validation

An aluminum plate of 1200 × 1200 × 3 mm^3 is used for validation. A circular piezoelectric transducer of diameter $a = 5$ mm and thickness $t_p = 0.4$ mm is attached at the center of the plate with epoxy adhesive, as shown in Figure 3.10. A waveform generator is used to excite a five-cycle sinusoidal tone burst of varying center frequencies from 60 kHz to 440 kHz with a 20 kHz step. The transverse displacement U_{zz} is measured by a Laser-Doppler

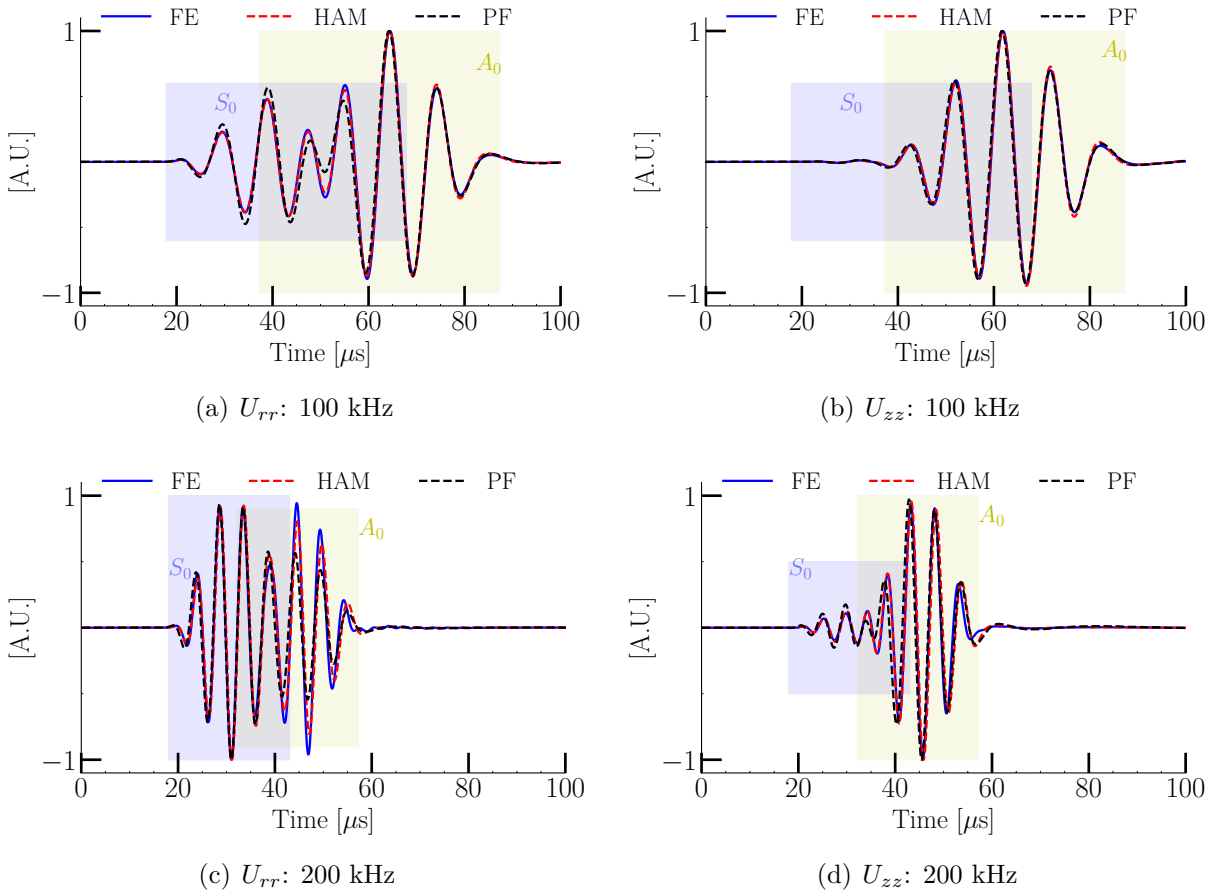

(a) U_{rr}: 100 kHz

(b) U_{zz}: 100 kHz

(c) U_{rr}: 200 kHz

(d) U_{zz}: 200 kHz

Figure 3.8: Comparison of displacement signals (U_{rr} and U_{zz}) computed from FE, PF, and HAM for C2 at 100 mm.

vibrometer at a distance of 60, 100, and 200 mm from the center of the piezoelectric transducer. The experimental configuration is similar to the C2 configuration shown in Table 3.1, and the same parameters are used. Therefore, the frequency-dependent behavior terms of C2 shown previously are used as an input to the HAM. The effective radius is computed based on the linear fit of the admittance curve ratio of bonded and unbonded transducers measured with an impedance analyzer, as shown in Figure 3.11. Figure 3.11. The recorded displacements are compared with the signals simulated with PF and HAM computed through CIVA. Similarly to the simulation study, four displacement signals at 100 kHz, 200 kHz, 300 kHz, and 440 kHz are shown in Figures 3.12 and 3.13 at three distances from the transducer. It has been observed that the experimental signals have a constant time delay with respect to the simulated results, which is likely due to the uncertainty of the material properties. The time difference between experimental and simulated signals is equal to 1.5 μs and is compensated in the plots by a constant shift of the time axis.

The conclusion of the experimental study is analogous to the one of the simulation study at all frequencies and at all locations. More specifically, at 100 and 200 kHz, both PF and HAM match the experimental signals, as shown in Figure 3.12. Furthermore, at

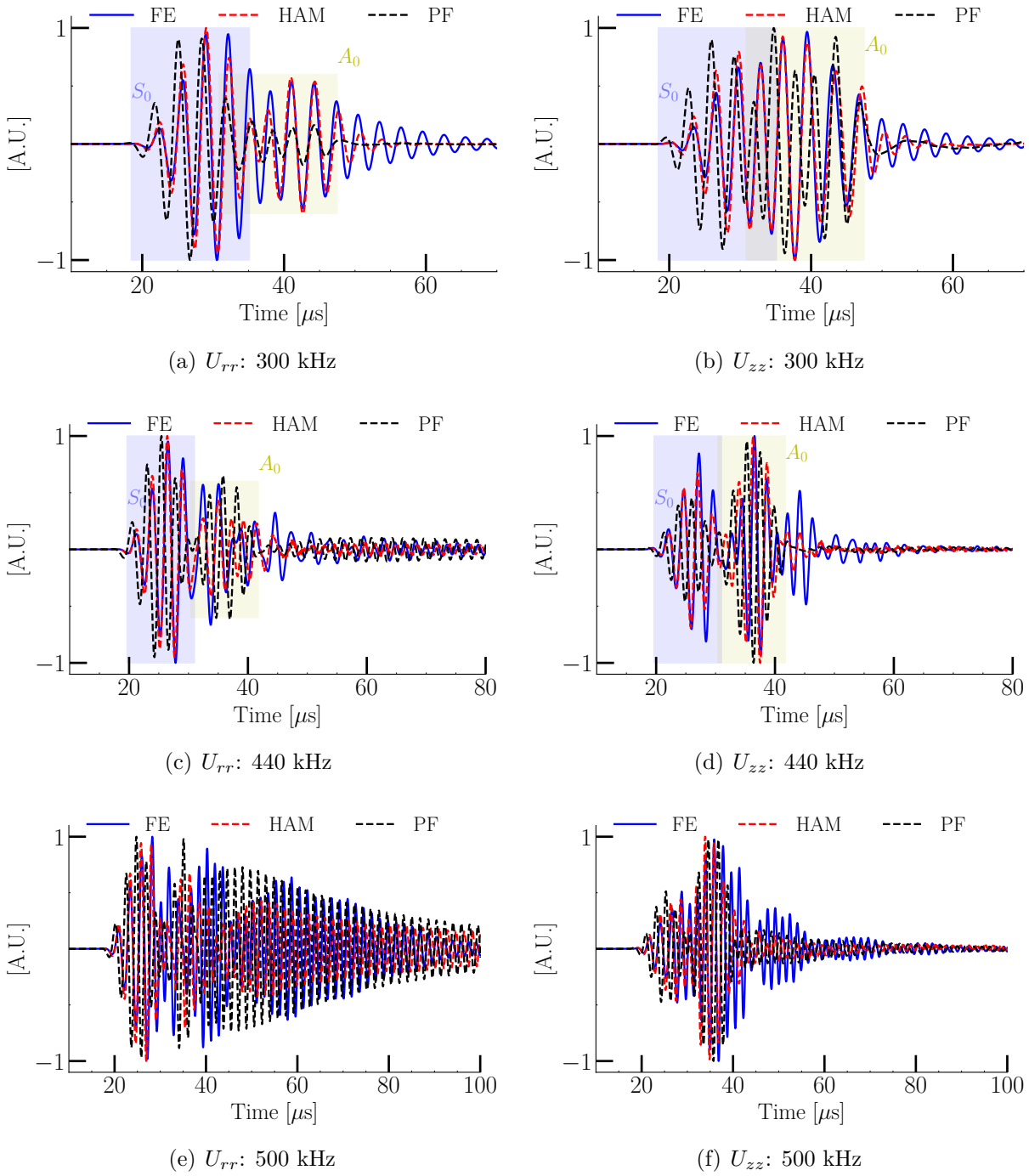

(a) U_{rr}: 300 kHz

(b) U_{zz}: 300 kHz

(c) U_{rr}: 440 kHz

(d) U_{zz}: 440 kHz

(e) U_{rr}: 500 kHz

(f) U_{zz}: 500 kHz

Figure 3.9: Comparison of displacement signals (U_{rr} and U_{zz}) computed from FE, PF, and HAM for C2 at 100 mm. (e,f) The high amplitude signals are the superimposition of multi modes of guided waves at 500 kHz.

300 kHz and 440 kHz, shown in Figure 3.13, the same phase-amplitude variations and additional cycles in the experimental signals are observed. These are correctly modeled by HAM for both modes but not by PF. Nevertheless, small differences in terms of phase

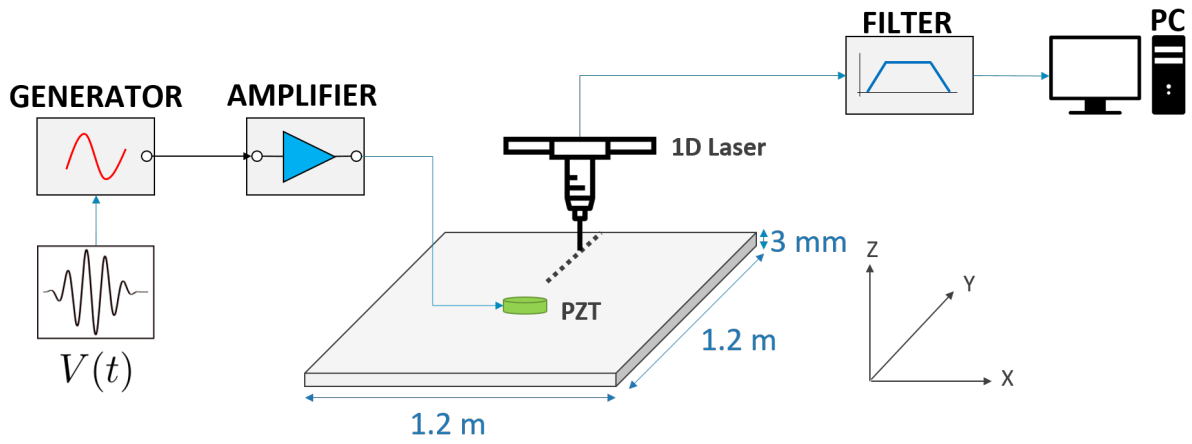

Figure 3.10: Experimental setup

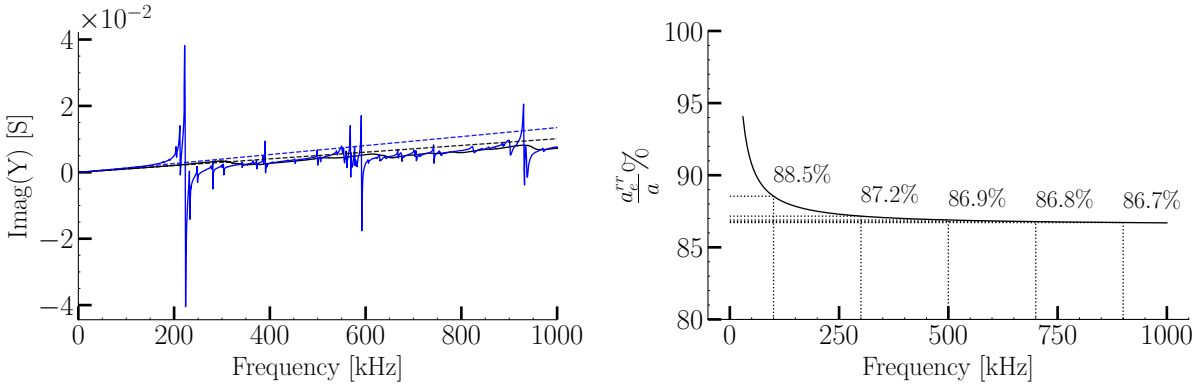

(a) Admittance curve

(b) Effective radius (a_e^{rr})

Figure 3.11: (a) The imaginary part of the admittance for bonded (black line) and unbonded (blue line) piezoelectric transducers measured by an impedance analyzer and their linear fit (dashed line) and (b) effective radius as a percentage of the original radius a.

and amplitude are observed between the HAM and experimental signal at the end of the A0 wave packet.

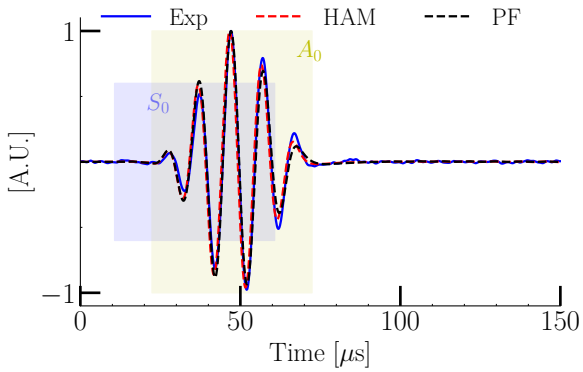

(a) U_{zz}: 100 kHz (60 mm)

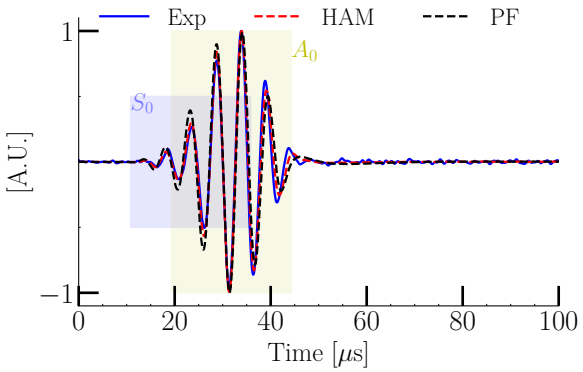

(b) U_{zz}: 200 kHz (60 mm)

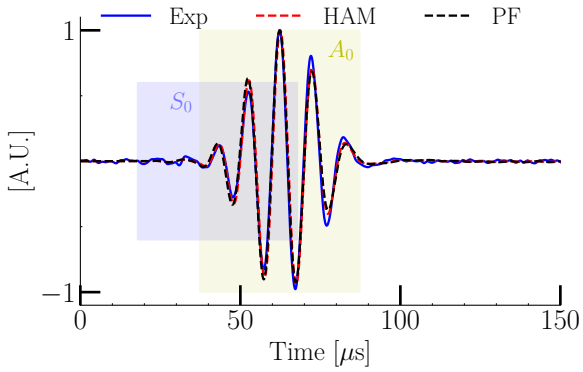

(c) U_{zz}: 100 kHz (100 mm)

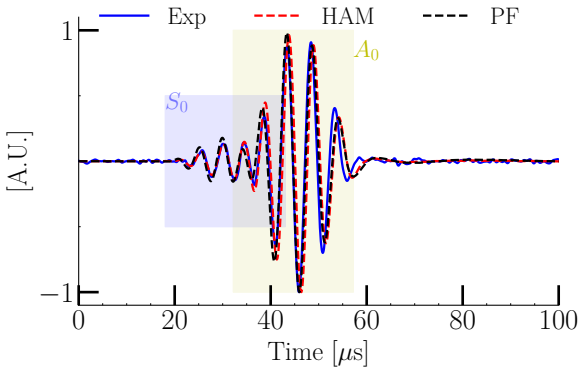

(d) U_{zz}: 200 kHz (100 mm)

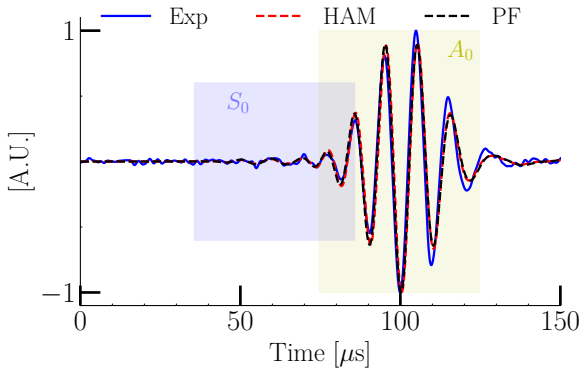

(e) U_{zz}: 100 kHz (200 mm)

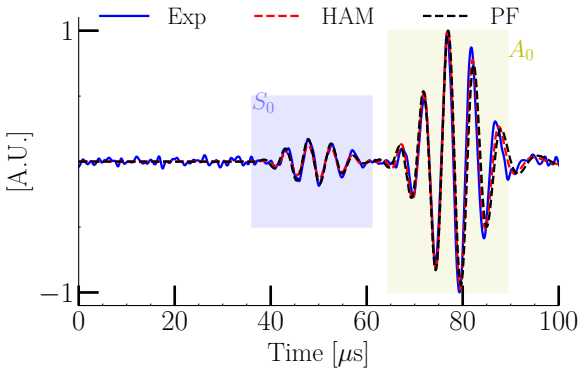

(f) U_{zz}: 200 kHz (200 mm)

Figure 3.12: Comparison of experimental U_{zz} with PF and HAM at 100 kHz (left) and 200 kHz (right).

Additionally, at 440 kHz, an additional wave packet is observed in the experimental signals at all three locations, as shown in Figure 3.13 (b,d,f), while there is no sign of such an additional wave packet in the simulated signals for C2, as shown in Figure 3.9(d). The simulations confirm that the additional wave packet is not due to an echo from the edge of the plate. To explain this phenomenon, the admittance of the bonded piezoelectric trans-

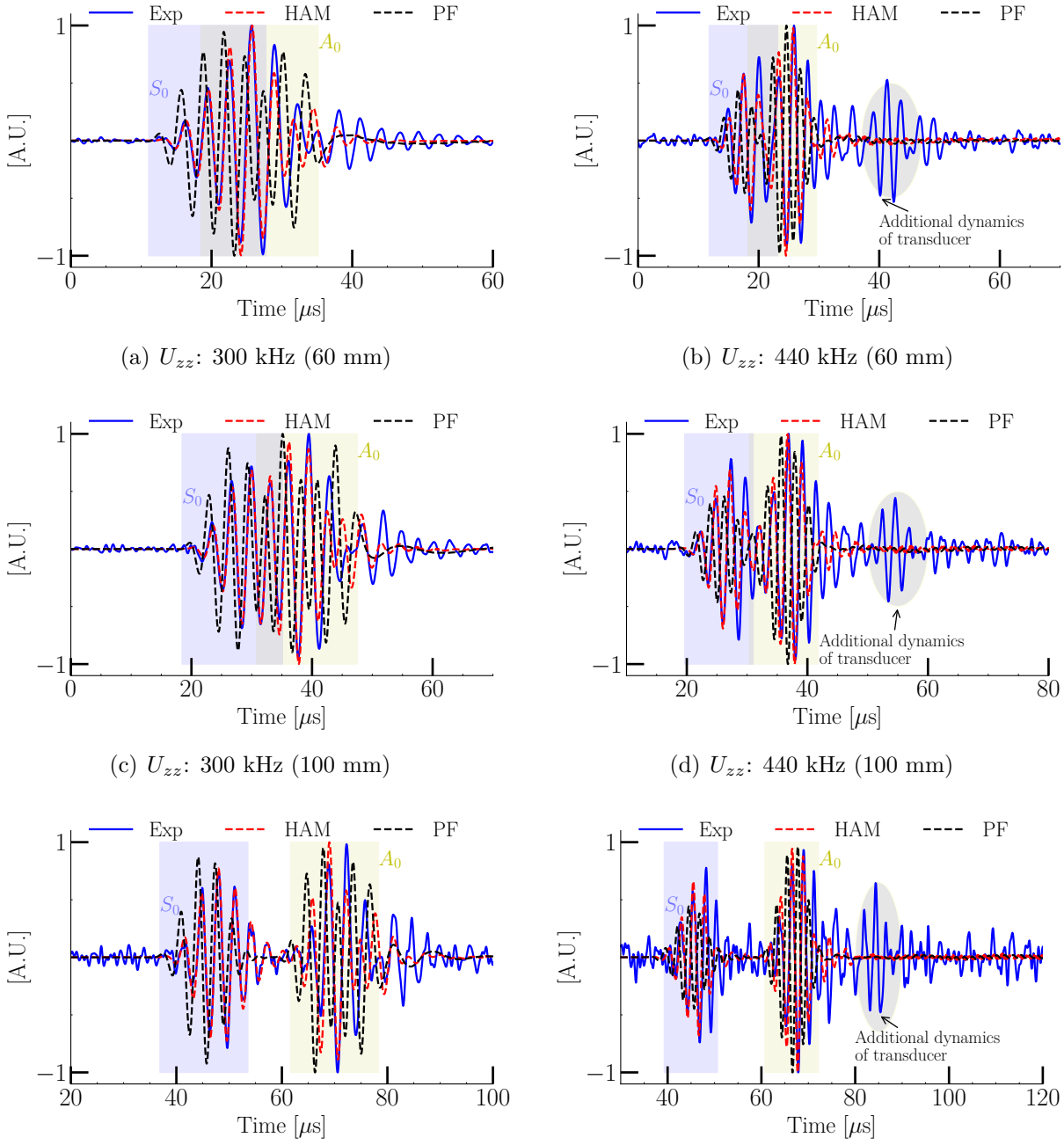

(a) U_{zz}: 300 kHz (60 mm)

(b) U_{zz}: 440 kHz (60 mm)

(c) U_{zz}: 300 kHz (100 mm)

(d) U_{zz}: 440 kHz (100 mm)

(e) U_{zz}: 300 kHz (200 mm)

(f) U_{zz}: 440 kHz (200 mm)

Figure 3.13: Comparison of experimental U_{zz} with PF and HAM at 300 kHz (left) and 440 kHz (right).

ducer is compared between the finite element and the experimental cases in Figure 3.14. While the imaginary part is well matched, the real part shows a significant mismatch at high frequencies, potentially due to the uncertainty of the material properties. The two main electromechanical resonance peaks around 320 kHz and 650 kHz are observed in both results with a good match. However, an additional peak is also observed in the

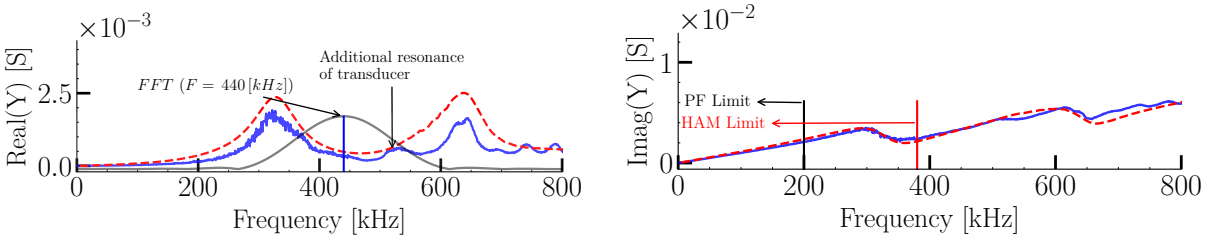

Figure 3.14: Comparison of admittance of bonded piezoelectric transducer obtained from finite element (denoted in red) and recorded experimentally (denoted in blue) where the bandwidth of the excitation signals $g(t)$ at 440 kHz is shown in light black: (a) real part (b) imaginary part.

experimental admittance around 500 kHz, but not in the simulated admittance. This additional peak could be due to an incomplete bonding between the transducer and the host structure or, more probably, to the asymmetry of the piezoelectric transducer electrodes, as discussed in [151]. Since the bandwidth of the 440 kHz excitation ranges from 300 kHz to 600 kHz approximately, as shown in Figure 3.14, the additional wave packet is assumed to be due to this additional resonance frequency of around 500kHz, thus explaining the mismatch.

3.4.4 Parametric study

Previous results show that the quality of the models is better at low frequencies than at higher frequencies. The goal of this section is to validate the models over a range of frequencies quantitatively. A normalized running correlation coefficient (C_Y^X) is defined, where X denotes the experimental signal and Y denotes signals obtained with either PF or HAM. The coefficient is calculated by:

$$C_Y^X = \max_k \left(\frac{R_Y^X[k]}{\sqrt{R_X^X[k] R_Y^Y[k]}} \right)$$

where $R_Y^X[k] = \sum_{m=0}^{n} X[m]Y[m-k]$ is the cross-correlation between X and Y, n is the number of time samples in the signals, and k is an integer between 0 and n. In addition, the time delay at maximum correlation ΔT_Y^X is also calculated as $T_X[k_{max}] - T_Y[k_{max}]$, where T_X and T_Y are the time vectors of X and Y, and k_{max} is $\underset{k}{\text{argmax}}\, R_Y^X[k]$. The calculation of C_Y^X is conducted twice over normalized signals, first windowed signals to avoid boundary reflections from the plate edges, and second, signals windowed up to the end of the A0 wave packet, as shown in Figures 3.15(a) and 3.15(b). For the first, the correlation is above 0.9 up to 250 kHz at all the locations for the HAM, while this value reached 150 kHz for PF. For the second, the 0.9 correlation value is crossed at 350 kHz for HAM and 200 kHz for PF. In addition, the time delay, shown in Figures 3.16(a) and 3.16(a), is nearly constant for HAM, while its curve is discontinuous for PF because the signals are out of phase at higher frequencies. The constant but non-zero value for HAM is likely due to the

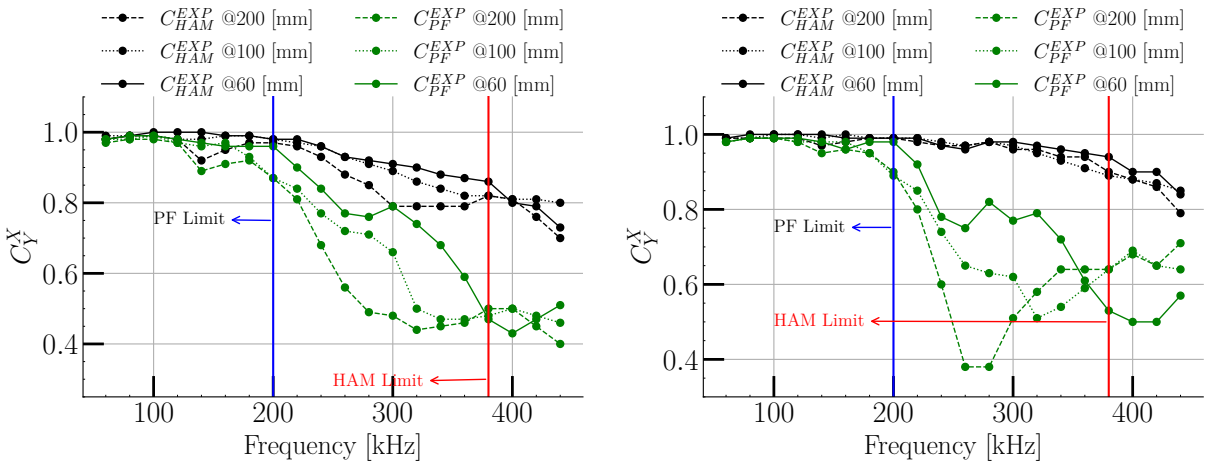

Figure 3.15: Normalized running correlation coefficient C^X_Y at three locations 60, 100, and 200 mm for the (a) full time domain signal and (b) signal windowed up to end of A_0 wave packet.

uncertainty of the material and piezoelectric properties. Hence, the validity range of the

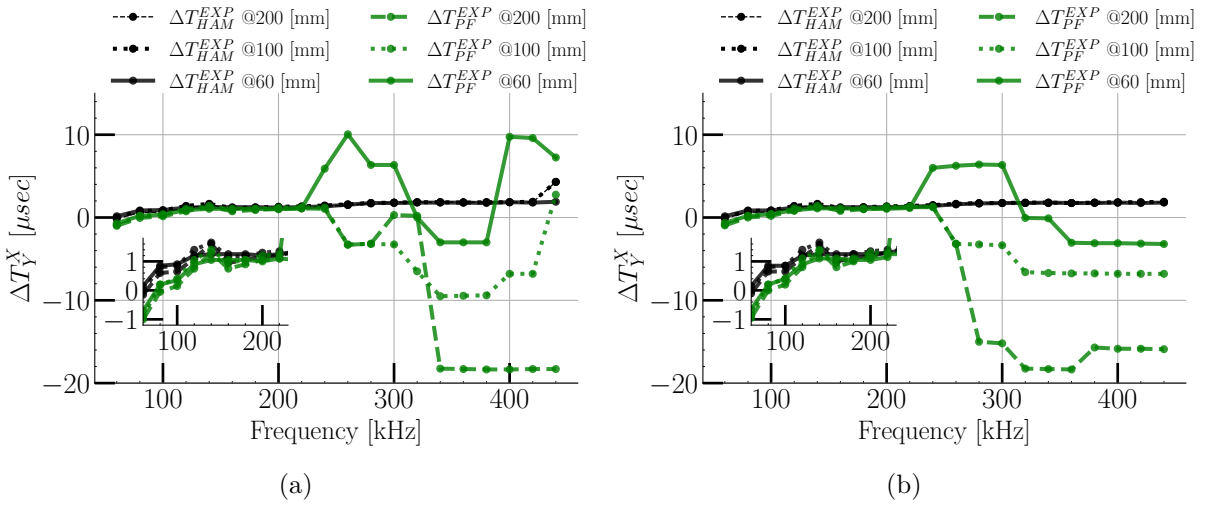

Figure 3.16: Time delay at maximum correlation ΔT^X_Y of (a) full time domain signal and (b) up to end of A_0 wave packet.

PF model is limited below the first electromechanical frequency of the coupled transducer, as shown in Figure 3.14(b), while HAM remains valid beyond this resonance. However, it should be noted that the correlation for HAM decreases beyond this resonance, which is either due to the aforementioned asymmetric electrodes of the transducer or imperfect bonding.

3.4.5 Discussion

Through the simulation, it has been observed that as excitation frequency increases, the loads applied to the plate become more and more different compared to the actuation signal $g(t)$. This effect is shown in the Figures 3.17(a) and 3.17(b) at 100 and 300 kHz; in which the surface loads $S_{rr}(t)/\max(|S_{rr}(t)|)$ and $S_{zz}(t)/\max(|S_{rr}(t)|)$ are represented, as defined in Equation 3.6. At 100 kHz, the loads are similar to the actuation signal $g(t)$. At 300 kHz and due to the transducer effect, the loads are different in both phase and amplitude from $g(t)$ at a higher frequency. This is why it is essential to consider the bi-directional loads as well as to take into account the frequency-dependent behavior of the transducer for modeling the GWs, near or beyond the first resonance frequency.

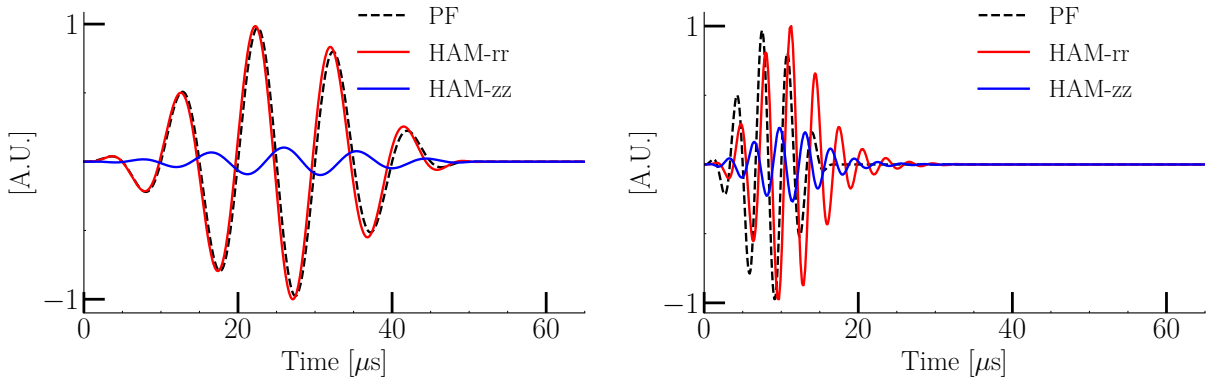

(a) 100 kHz (b) 300 kHz

Figure 3.17: Comparison of PF actuation signal $g(t)$, and HAM actuation signals $S_{rr}(t)/max(|S_{rr}(t)|)$ and $S_{zz}(t)/max(|S_{rr}(t)|)$ at 100 and 300 kHz.

3.5 Conclusion

This chapter proposed a new circular piezoelectric actuator model (denoted HAM for Hybrid Actuator Model). The model is based on 1) the use of the radial and normal stresses between the transducer and the host structure, pre-computed by finite elements taking into account the adhesive layer, and 2) an effective area calibrated with an experimentally-measured electromechanical impedance. The HAM is compared with the Pin Force (PF) model and validated on both numerical and experimental data. In the low-frequency regime, i.e., well below the first free resonant frequency of the transducer, both models match fairly well the experimental data. However, in the vicinity of the first free resonant frequency, the PF model fails while the HAM successfully reproduces the experimental signals up to the first free resonant frequency. For precise quantification of the domain of validity of both models, a criterion is proposed and evaluated. This new hybrid model is valuable as it is fully compatible with computation using a surface load as a source in the time domain, in particular for computationally-efficient explicit spectral finite element

codes. It will therefore be a crucial enabler of the model-assisted probability of detection or other computation-intensive studies beyond the PF validity range.

Part II

Performance demonstration for SHM

CHAPTER 4

Model assisted POD methodology

Outline

4.1 Introduction

The objective of an inspection/monitoring system is to identify the condition of a structure, i.e., to decide whether critical flaws are absent or present in the structure. The decision-making process is influenced by many factors that affect the response from an inspection system, for example, multiple inspections of the same structure can lead to different responses due to minimal setup changes. Even defects of the same type and size can produce different responses due to variability of defects (shape, roughness, location, material, etc.), inspection system (hardware, process, algorithms), and many others (temperature, humidity, wind, moistures). Therefore, performance demonstration of an inspection/monitoring system is essential for increasing reliability and reducing false maintenance calls before

their implementation in industries. Performance demonstration is achieved by repeating the inspection procedure several times on similar configurations in the presence of representative variabilities and making a decision based on observed responses on the presence and absence of defects. The procedure of performance demonstration of NDE techniques is well documented in the MIL-HDBK-1823A and ENIQ report 41 [86] and quantified through the determination of probability of detection (POD) curves.

Similarly, for SHM systems, the POD curve determination is identified as a key enabler of SHM in the aerospace industry. For example, Sandia National Laboratory, Boeing, and Delta Airlines [152] demonstrated the performance of the Comparative Vacuum Monitoring based SHM system (explained in introduction section 1.1.1) on a thin panel of aircraft under fatigue loading based on the POD curve and finally FAA certified their use in aircraft in 2017 [20]. Apart from this SHM system, there is no other SHM system in civil aircraft industry that has been certified so far. This is because of two major challenges in the performance demonstration of SHM system (more details are presented in the introduction section 1.2.2). The first is that due to the fixed nature of the sensor, multiple instrumented structures are required to evaluate the performance, so the cost is prohibitive. And, the second is to address the issue of statistical dependency in the observed responses from the sensor (explained more precisely in the next chapter). Therefore, a cost-effective procedure based on simulation, called a model-assisted probability of detection (MAPOD), and inspired by the same approach developed in NDE, has become an essential requirement for the quantitative evaluation of SHM systems. For this, as mentioned in the previous chapters, the CIVA simulation tool has the potential to produce many repeated measurements: recently, Mesnil et al. [153] has presented a MAPOD computation by creating a metamodel for GWs based SHM imaging by using CIVA. However, an essential step of MAPOD procedure is to evaluate the accuracy of the simulation tool to produce consistent results under the range of variation of the influencing variabilities for successful use in real cases [134]. This study was limited in the previous MAPOD studies, i.e., no actual link was established between experimental and simulation POD studies.

Therefore, this chapter proposes both experimental and simulation methodological steps to obtain performance demonstration of GWs based SHM responses for a use case under multiple variabilities. The simulation methodology allows for reproduced variation in output response even if deterministic software is used for the numerical simulation. Four basic methodological steps are proposed to measure the performance of the SHM system in terms of the probability of detection curve, as shown in Figure 4.1. The first step is basically to define the configuration of interest under consideration for the POD study, such as specimen (geometry and material properties), monitoring system, sensor location and positions, and, more importantly, the targeted defect type (geometry, position, and orientation) and sources of variabilities (with their statistical distribution). The second step is to obtain, generate and validate the SHM POD data under the considered influencing variabilities. SHM POD data can be generated through experimental, simulation, or both. However, before using a simulation-based study, it is highly recommended to use an experimental study where multiple identical structures are needed to validate the simulation-based approach under the considered influencing variabilities. If the simulation-based responses do not agree with the experimental study, some calibration methods can be used to associate the simulation responses with the real-case scenario. The third step

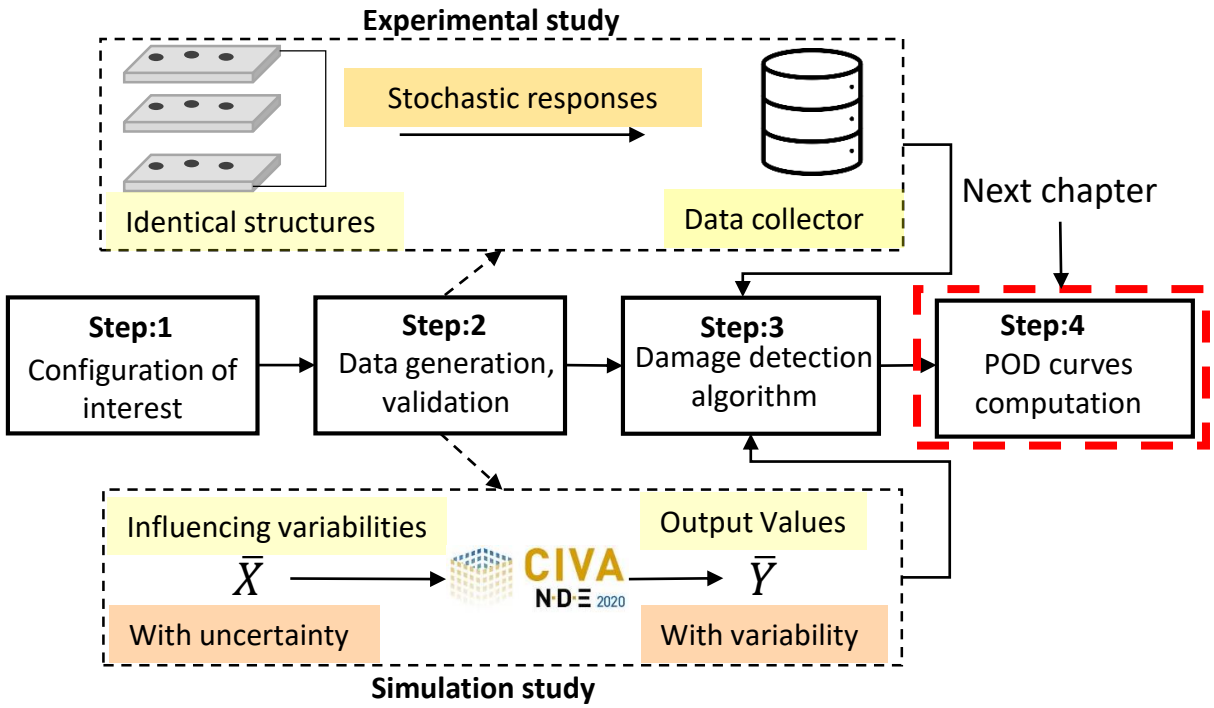

Figure 4.1: Methodological steps to obtain experimental and model-based probability of detection curves for GWs based SHM.

is based on the damage detection strategy to measure the damage response from the acquired signal, which is directly related to step four of the POD curve estimation since inappropriate damage detection algorithm will result in the unacceptable performance of the SHM system established by the POD curve. Some specialized statistical methods are needed to estimate the relationship of the measured response to damage characteristics. However, before developing the POD curve determination, i.e., step 4, in the next chapter, this chapter focuses on creating the required data. The data on a specific use case is generated through experimental and simulation studies. Specific care is given to validation to ensure data quality confidence before POD computations.

4.2 Objective

The objective here is to compare simulation output response to a well-controlled experimental estimation and validate that it is possible to apply model-based POD assessments for GWs based SHM. The use case under study is similar to the use case of Kabban et al. [109] and Meeker et al. [110], where a crack grows from a hole of an isotropic aluminum plate under a fatigue load. Although much research emphasizes the detection and localization of crack length through GWs based SHM, fewer articles show the probability of crack length detection or localization. Because of influencing variabilities, the GWs based SHM signals tend to be stochastic in response. Therefore, twelve identical aluminum plates with

a hole where a crack grows with the help of a saw tooth are considered in this study to elicit GW stochastic responses. Furthermore, variabilities, e.g., temperature, crack length, and material properties, are recorded during experiments and used to determine variability limits for a MAPOD study. Then the complex stochastic GW signals measured from both experimental and simulation studies are compared to guarantee the validity of simulation results. Both experimental and simulated signals are mapped to the damage index (DI) as a scalar quantity to identify the relation between crack length and DI. Lastly, a study of DI variation with normalized crack length by wavelength is presented to exhibit higher sensitivity towards crack length with frequency.

4.2.1 Specimen description

A simplified structure of a square aluminum plate 600 × 600 × 3 mm^3 with a hole in the center is considered to monitor crack growth via GWs based SHM. Four circular transducers of radius 5 mm are permanently glued to the structure, denoted as #1, #2, #3, and #4, where two transducers (#1 and #2) are in direct paths and the other two transducers (#3 and #4) are in the diagonal path of crack initiation and the entire configuration is represented as a single unit, as shown in Figure 4.2.

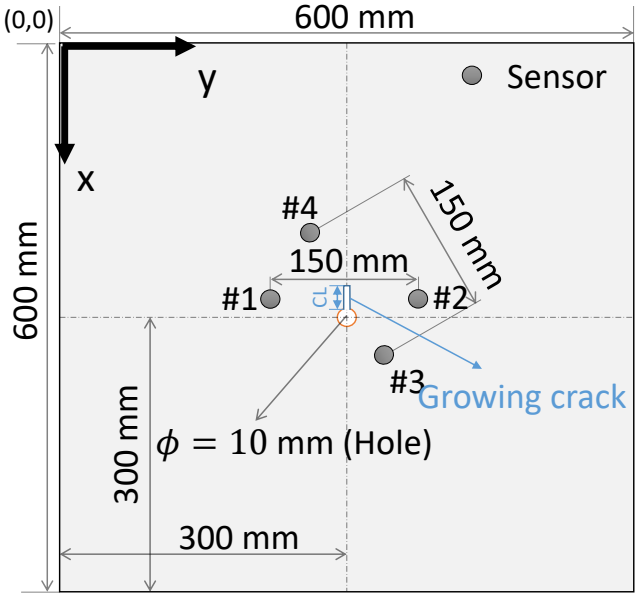

Figure 4.2: Configuration of interest (twelve of such units are created experimentally).

4.2.2 Actuation signal and frequency selection

A transducer is actuated by an actuation signal to transmit guided wave signals into the structure. A sinusoidal tone burst modulated by the Hahn window is chosen because it limits the bandwidth of the frequency in the actuation signal, reducing dispersion in GWs.

The mathematical form of the actuation signal is represented below:

$$g(t) = A\sin(\omega_c t)\left[1 - \frac{\cos(\omega_c t)}{N}\right] H\left(\frac{2\pi N}{\omega_c} - t\right)$$

where N, A, and ω_c denote the number of cycles, signal amplitude, and central actuation frequency, respectively, while H is the Heaviside function. In isotropic plate-like structures, guided waves always have at least two propagating modes, denoted as S_0 and A_0. As the actuation frequency ω_c or thickness of the structure increases, the number of modes increases simultaneously, as reported in chapter section's 2.2.3. The selection of ω_c depends on the wavelength of propagating wave modes because wave modes are only sensitive to those damage sizes that exceed half the wavelength of the wave mode [107]. While as ω_c increases, the wavelength of modes decreases, which increases the chance of detecting smaller defects. However, identifying defect signatures at a higher actuation frequency is complex work due to the multimode nature of guided waves. Therefore, ω_c is typically kept below the first cut-off frequency, meaning that only two modes (S_0 and A_0) are allowed to propagate. Furthermore, the amplitude trade-off between S_0 and A_0 wave modes depends on the excitability curve, which can be estimated based on transducer response (Equation 2.32 in chapter 1) or explained in [131], as shown in Figure 4.3(a).

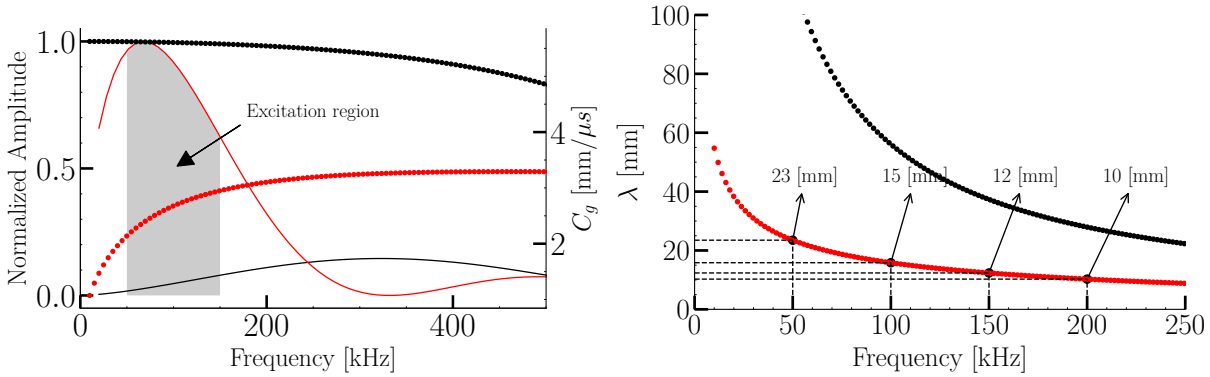

Figure 4.3: (a) Transducer excitability curve (solid line) for 5 mm radius piezoelectric transducer, and on the right axis energy velocity curve (marker ∘) computed from SAFE (red and black colors denote A_0 and S_0 modes, respectively) (b) Wavelength of guided waves as a function of frequency.

In order to obtain the maximum response of guide wave signals after interaction with minimum damage size while keeping the maximum amplitude of mode, this study is selected a 100 kHz central frequency with five cycles based on the A_0 mode since the wavelength of A_0 mode is lower than S_0 mode, as shown in Figure 4.3(b).

4.2.3 Experimental study

Twelve identical and independent aluminum units based on the configuration described in the previous section 4.2.1 are considered for the SHM POD study. The experimental setup is shown in Figure 4.4, where four Steminc piezoelectric transducers [150] were glued to each aluminum plate using epoxy adhesive. A round-robin condition is used, which means one transducer acts as an actuator, whereas all others act as receivers. A series of five-cycle tone burst actuation signals of central frequencies of 60 to 340 kHz are generated by a wave generator (Keysight Technologies) with a step size of 20 kHz. These actuation signals are amplified to a peak-to-peak amplitude of 40 volts with the help of a power amplifier. The signals measured by the receivers are first filtered analogically and amplified by a low-noise preamplifier (Stanford Research Systems) with a second-order high-pass filter with a cutoff frequency of 10 kHz. Then, the signals are digitized using NI-DAQ at a 2 MHz sampling frequency and averaged 50 times to increase the signal-to-noise ratio. The overall acquisition process is fully automated thanks to a LABVIEW code and multiplexers that allow switching between the piezoelectric transducers.

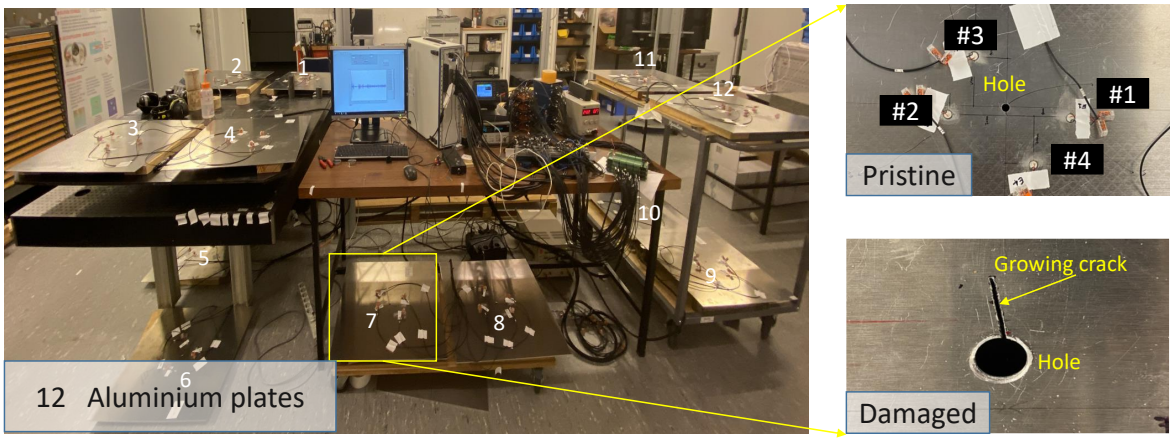

Figure 4.4: Experimental setup of 12 aluminum plate units for GWs based SHM.

Experimental GW signals are recorded on two configurations denoted as pristine and damaged units. A pristine unit represents an aluminum unit with a hole, and a damaged unit represents when a crack begins on the pristine unit and progresses. Firstly, pristine signals, i.e., baseline signals, are acquired on the 12 pristine units and stored in a multi-dimensional array (dimension is $12 \times 4 \times 4$)[1], denoted as experimental pristine signals. After that, GW signals are acquired on the 12 damaged units, where a saw tooth helps to cut a through-thickness slit as a crack at the one side of the hole. This process is repeated for 21 days, and on each day, a 1 mm to 1.5 mm slit length, i.e., crack length, is increased to make representative of a growing crack under fatigue load. These damaged signals are stored in another multidimensional array (dimension is $21 \times 12 \times 4 \times 4$)[2], denoted as experimental damaged signals. The crack length distribution (measured on each unit with

[1]It represents 12 units, 4 emitters, and 4 receivers.
[2]It represents, 21 crack lengths, 12 units, 4 emitters, and 4 receivers.

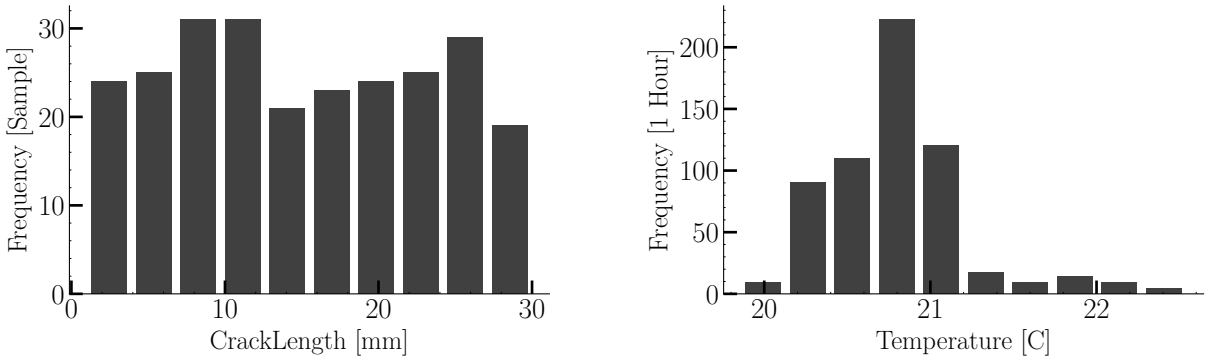

(a) Crack length (b) Temperature

Figure 4.5: Distribution of crack length and temperature measured during the experiment. The temperature is recorded every hour in the laboratory on three different days. First when the transducer is attached, second when a hole is drilled, and third at a crack length of 5 mm.

the help of a ruler during the growing crack) and temperature distribution (recorded by a thermocouple in the laboratory) are shown in Figure 4.5.

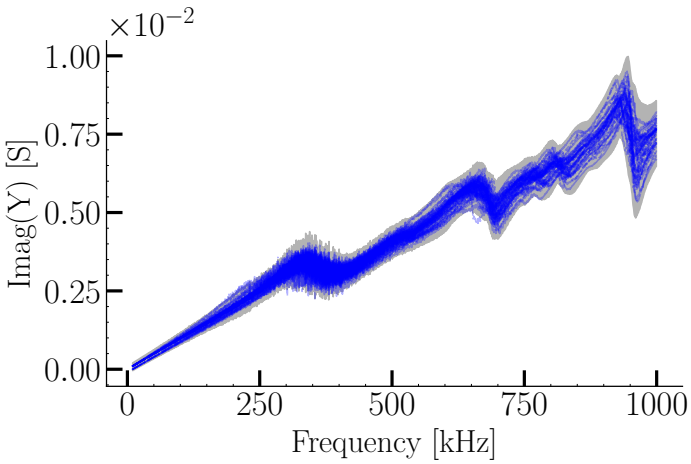

Figure 4.6: Transducer admittance curve of all 48 bonded piezoelectric transducers in blue and their ±3 standard deviation bound in light black colors.

Additionally, it is essential to check the admittance curve for each attached transducer in GWs based SHM to ensure a sufficient bond between the transducer and structure, as mentioned in [10]. Therefore, admittance curves are recorded from each transducer of each pristine unit (total of 48 transducers) with the help of an impedance analyzer and represented with a bound of their ±3 standard deviations in Figure 4.6. This figure shows a good bond between transducers and all the aluminum plates, while variation in admittance curves is due to uncertainty in the properties of piezoelectric transducer and adhesive materials and different thicknesses of an adhesive layer on each unit, as mentioned in chapter section 3.3.1. It is also worth noting that debonding, degradation, and transducer

breakage also change the admittance curve amplitude and resonance points, as mentioned in [154], but are not observed in the data.

4.2.4 Simulation study

This study describes obtaining GWs based SHM stochastic responses by simulation, i.e., through the MAPOD methodology. As mentioned earlier, such SHM systems are affected by the variability of various influencing parameters, such as damage characteristics (e.g., size, orientation, positions...), inspection variables (e.g., transducers positions, geometry, materials...), and environmental variables (temperature, humidity, moisture...). These variables result in the stochastic nature of the SHM system, i.e., the variability in their responses. Variability of the various influencing parameters is always associated with uncertainty due to a lack of knowledge of the parameters (i.e., the limited amount of data). Therefore, a simulation model should adequately represent the actual response under influencing variabilities, i.e., reproduce the variability of the response in the SHM system. This could be achieved by introducing uncertainties on the model's input parameters, which are identified as influencing variabilities to generate a large number of slightly different configurations representative of actual usages of the SHM system. An efficient and validated simulation tool, such as CIVA [153], is required to simulate many configurations. To induce the variability in the output of the GWs based SHM response, a detailed simulation study with three levels is carried out as follows.

Level 1: Define all nominal input parameters

This defines all the necessary information about all nominal input parameters (e.g., dimension, geometry, transducer locations, elastic properties...) for monitoring structure in the simulation tool. This study considered the configuration described in the previous section 4.2.1 and listed their important nominal parameters in Table 4.1.

Input Parameters	Values
Mechanical properties of structure	E=75 [GPa] ρ=2660 [kg m^{-3}] ν=0.33
Transducer location in mm	#1=(220,310) #2=(370,310) #3=(340,240) #4=(265,370)
Hole location in mm	(300, 300)
Hole diameter	5 mm
Central frequency	100 kHz with 5 cycles

Table 4.1: Nominal input parameters of configuration of interest.

Level 2: Identity influencing variabilities

Based on a previous study by Janapati et al. [104], the five most influencing variables have been considered in the simulation tool for the MAPOD study of growing cracks on an aluminum plate. Then, each variability is assigned a statistical distribution by its functional forms (e.g., normal, uniform...) and associated parameters (e.g., mean, variance...). It should be ensured that the variation range of the statistical distribution bounds all values of the source of the variability encountered during the inspection due to lack of control. However, the choice of a statistical distribution and its parameters are often based on previous studies, experimental studies, or engineering judgment. Some variability ranges and distributions are recorded during the experiment, such as crack length, temperature, and transducer admittance, as mentioned in Figures 4.5 and 4.6.

Variability	Distribution	Parameters	Unit
Transducer and Hole Location	Normal	μ=Table 4.1 σ=2	mm
Temperature	Normal	μ=25 σ=5	°C
Effective radius	Normal	μ=4.4 σ=0.1	mm
Crack length (CL)	Uniform	min CL=1 max CL=30	mm

Table 4.2: Variabilities and their uncertainty parameters with distribution characteristics (μ: mean, σ: standard deviation).

Variability in transducer installation and hole location: An approximately ±5 mm transducer and hole location variations in X and Y coordinates were observed from their nominal values when attaching 48 piezoelectric transducers and drilling holes on 12 aluminum plates. A normal distribution with a mean value of their nominal values and a standard deviation of 2 mm is a reasonable assumption to represent transducer installation and hole location variabilities.

Variability in temperature: Variation in temperature is counted as one of the most influencing variability for GWs, as explained in [57]. The temperature changes in the simulation tool are obtained by changing the elastic properties of the structure, i.e., the change in longitudinal and shear wave velocities. It can be modeled based on a linear relationship between the temperature and the two elastic wave velocities, as noted in [155] and the mathematical form of their linear relationship is shown below:

$$C_s = C_{s0} + k_S(T - T_0)$$
$$C_p = C_{p0} + k_L(T - T_0)$$

where C_s and C_p denote shear and longitudinal velocity, respectively, C_{s0} and C_{p0} are the velocities at reference temperature (T_0 is assumed to be 25 °C), k_s and k_p are the

temperature dependence constants, while T is a measured temperature. The k_s and k_p are -0.752 and -1.089 $\mathrm{m\,s^{-1}\,{}^{\circ}C^{-1}}$ [155], and C_{s0} and C_{p0} values are 3130 $\mathrm{m\,s^{-1}}$ and 6132 $\mathrm{m\,s^{-1}}$ (computed based on C_p and C_s explained in the chapter 2.2).

The temperature variability is recorded in a close laboratory and varies from 20 to 22.5 °C, as shown in Figure 4.5(b). A normal distribution is again assumed to describe the temperature variability with a mean temperature of 25 °C and a standard deviation of 5 °C, enclosing the recorded temperature range. Note that this is a conservative assumption of the temperature distribution that may influence the results, whereas the recorded temperature distribution was only for three days. Therefore, we expect a temperature distribution at standard room temperature.

Variability in transducer as effective radius: Variation in the transducer admittance can be representative of many variabilities due to transducers such as degradation, aging, breakage, and adhesive thickness in between transducers and structure that directly affect GWs propagation in the structure. As discussed in previous chapters, an approximate transducer model called the Pin Force (only radius of excitation can be varied in this model) is used in the CIVA simulation tool. Therefore, experimentally, the measured transducers admittance curve variations are converted into an effective radius calculated based on a bonded and unbonded transducer admittance ratio, as explained in Equation (3.5). It is worth noting that some of the calculated effective radii appear to increase with frequency, while others appear to decrease with frequency. This is highly likely due to using only the single transducer unbonded admittance curve in calculating the effective radius. While other 47 transducers' unbonded admittance curves were unfortunately not recorded prior to attachment to the structure during the experiment, as all transducers were assumed to be similar in characteristics. Indeed, they have larger variability than initially thought.

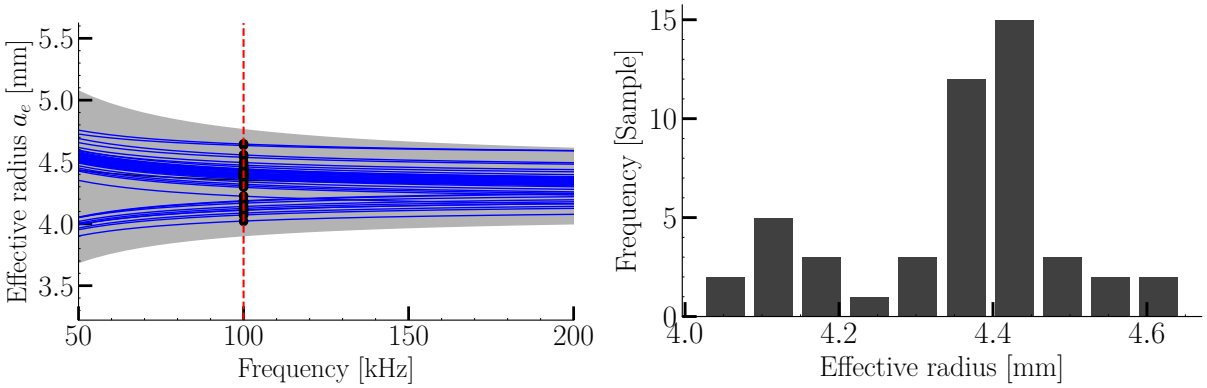

Figure 4.7: a) The effective radius of all 48 piezoelectric transducers is displayed in blue lines with their ±3 standard deviations bounded in light black color. It is computed based on the admittance ratio of the bonded and unbonded piezoelectric transducers. (b) Computed effective radius distribution at 100 kHz.

It should also be noted that the effective radius variation is lower than the transducer's actual radius (5 mm) at a 100 kHz frequency, as shown in Figure 4.7. Similarly, a normal distribution is assumed to represent transducer variability as effective radius with a mean of effective radius 4.4 mm with a very small standard deviation of 0.1 mm. Note that the estimated effective radius distribution is not fully representative of a Normal distribution but more toward double Normal distribution with two peaks (smaller at 4.1 mm and larger at 4.4 mm).

Variability in crack length: This variability considers a uniform distribution of crack lengths similar to the experimentally recorded crack length distribution, as shown in Figure 4.5(a). The minimum crack length is 1 mm, and the maximum is considered 30 mm, e.g., to illustrate the crack length with meshed configuration in CIVA a configuration of 15 mm crack length is shown in Figure 4.8.

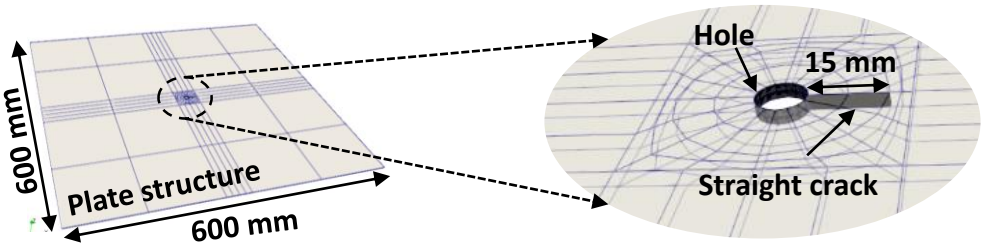

Figure 4.8: Crack length of 15 mm from hole mesh configuration obtained from CIVA.

Level 3: Simulation run

A Monte Carlo simulation-based strategy is used to take the uncertainty distribution for each variable as input to determine the variability in the output response from deterministic software. A complete strategy of the simulation run is shown in Figure 4.10, where 100 random units are first selected from the transducer and hole distributions. The simulation run is performed over two configurations which are represented as pristine and damaged units. Similar to the experimental study, a pristine unit represents an aluminum unit with a hole and a damaged unit when a crack begins on the pristine unit and progresses in the simulation. A Monte Carlo simulation is used to run pristine unit, where the two inputs from two variability distributions, temperature and effective radius, are randomly selected in the simulation. This process is repeated 100 times to run the simulation for a total of 100 pristine units, and each time with a sampling frequency of 2 MHz, the simulation output is stored in a multidimensional array (dimension is $100 \times 4 \times 4$)[3] as a time domain signal, denoted as simulated pristine signals.

Similarly, for damaged units, first, twenty crack lengths from the crack length variability are selected based on jittered sampling [156] for each unit. This sampling samples a crack length from a uniform distribution in such a way that it covers the entire area of interest while ensuring some randomness in the process. As shown in Figure 4.9, the

[3]It represents 100 units, 4 emitters, and 4 receivers.

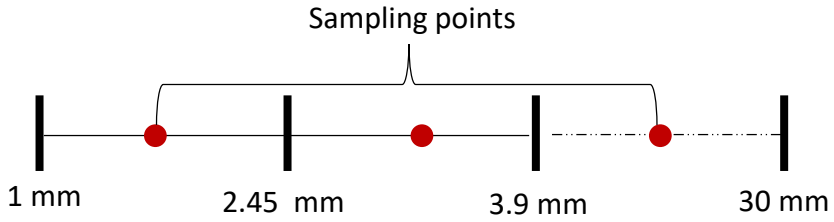

Figure 4.9: A jittered sampling of the cracklength: the region of interest is split into segments (black lines), and one measurement (red circles) is taken randomly within each segment.

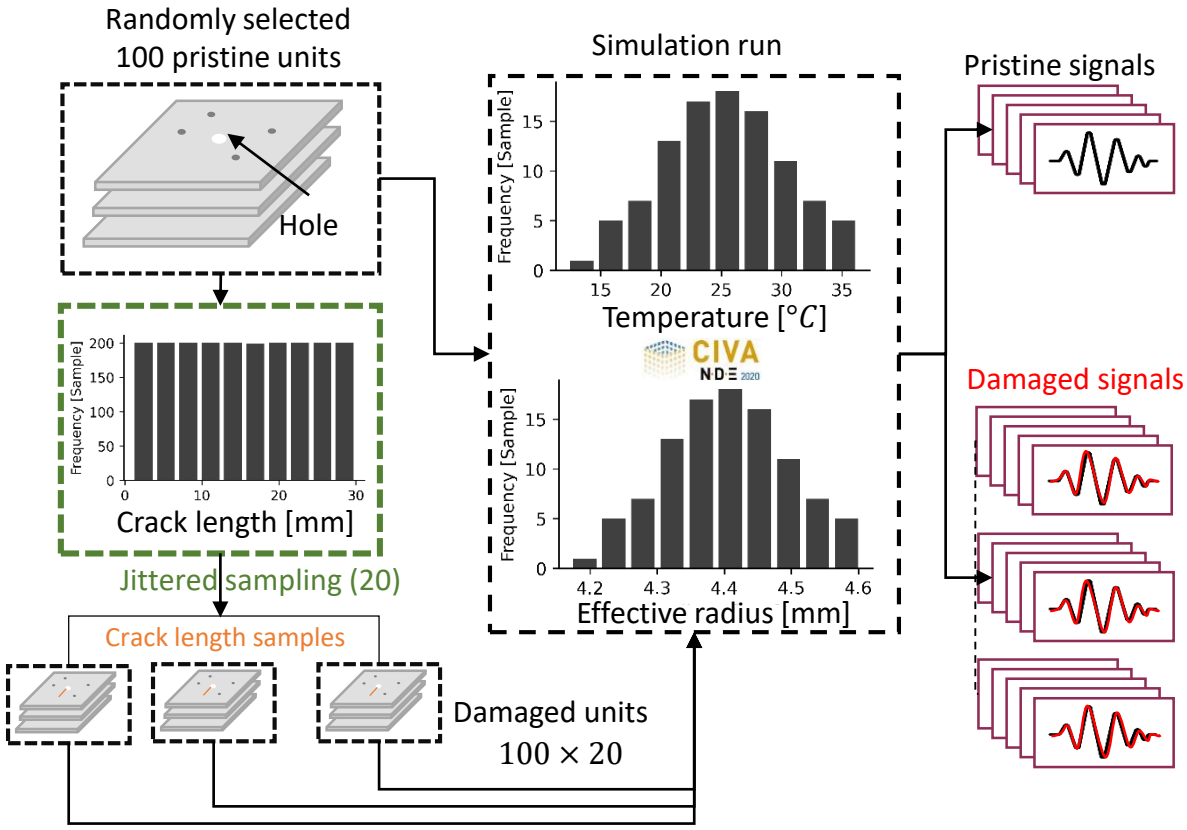

Figure 4.10: Simulation run strategy for MAPOD study of a growing crack on an aluminum plate.

crack length from 1 mm to 30 mm is divided into 20 segments, and sampling points are randomly selected between each segment in order to compromise between randomness and regularity. Now, each damaged unit contains 20 crack length samples (refer to the Figure 4.10 at the left bottom) and covers the entire region of interest. Like the pristine units simulation, a Monte Carlo simulation is used to run damaged unit, where two inputs from two variability distributions, temperature and effective radius, are chosen randomly in the simulation. This process is performed for 100 × 20 times to run the simulation for a total of 100 × 20 damaged units, and each time with a sampling frequency of 2 MHz, the

simulation output is stored in another multidimensional array (dimension is 20 × 100 × 4 × 4)[4] as a time domain signal, represented as simulated damaged signals.

4.2.5 Comparison of experimental and simulation signals

This section compares simulated and experimental time signals of pristine and damaged units. Only four out of twelve paths on each unit of simulated pristine and experimental pristine signals are compared at 100 kHz, as shown in Figures 4.11 and 4.12, as other path signals show similar findings. Also, these signals are normalized with their maximum amplitude and windowed to the complete cycle of A0 mode. In addition, the electromechanical coupling is also removed from all experimental signals. For a better understanding of path signals, a notation Path #E to #R is used, indicating that transducer E acts as an emitter and transducer R acts as a receiver, while E and R represent transducers number from 1 to 4.

It is indeed visible, as the blue signals are included inside the grey area, that the simulated signals capture all the variabilities of the output of the GW response signals from the experiments. The simulation also provides more significant signal variation, which has not been observed in experimental studies due to the non-availability of large variation in variability during the experiment (e.g., temperature variation, number of units...). It is also observed that GW signals have time shifts and amplitude variations among all identical pristine units due to influencing variabilities in the SHM system.

Furthermore, simulated damaged and experimental damaged signals with increasing crack length from the hole are shown in Figure 4.13. A direct path of one unit, i.e., Path #1 to #2 signal for both simulated and experiment is displayed for simplicity. Note that these damaged signals are normalized with the same normalization factor as their pristine signals. As crack length increases, a monotonic reduction of the signal amplitude and a monotonically increasing delay in both simulated and experimental damaged signals are observed. These signals exhibit similar effects that were observed due to the variabilities among pristine signals.

4.2.6 Damage Index

Identification of damage in signals is defined as the third step of the POD methodology study, as mentioned in Figure 4.1. In GWs based SHM systems, it is an essential consideration how to decode complex SHM signals into damage features. A damage index (DI) based strategy for damage identification has become very popular since it is simple, fast, and repeatable. As mentioned earlier, GWs are either reflected, scattered, or converted to other wave modes if structural integrity changes or damage occurs between the path of propagation of waves in the structure. DI measures these changes to identify the damage severity in the working structure. Several DI estimation methods exist in the literature [64, 157]. But the DI chosen for this study is based on high sensitivity to the crack length

[4]It represents 20 crack lengths, 100 units, 4 emitters, and 4 receivers.

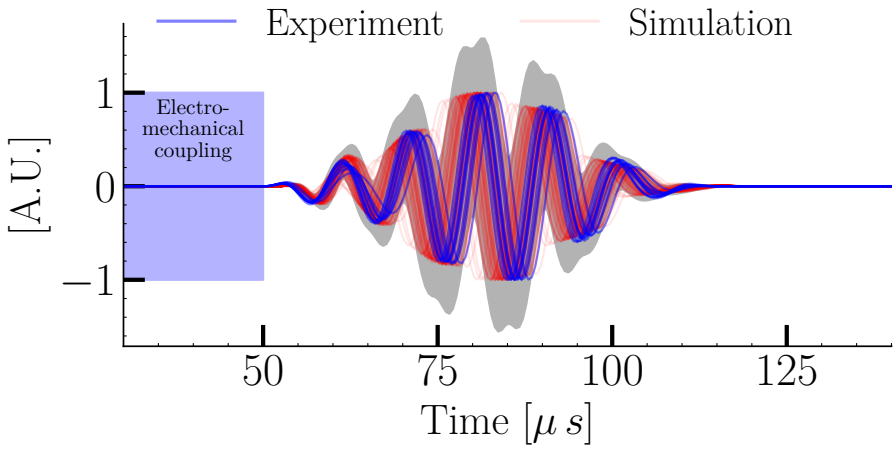

(a) Path #1 to #2

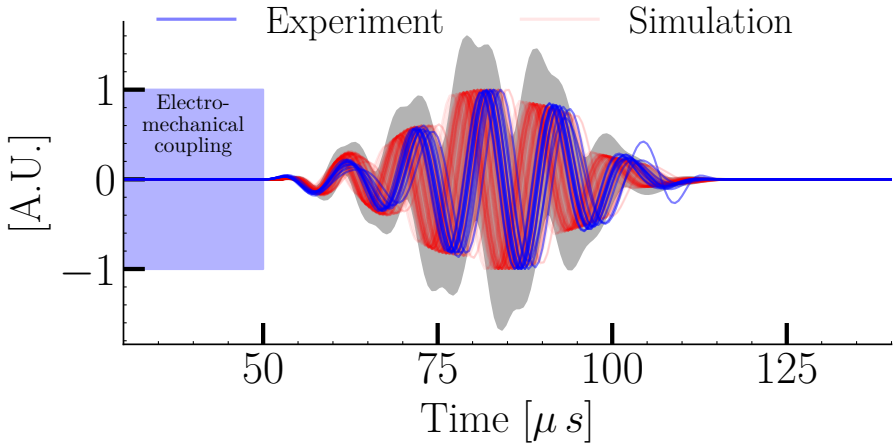

(b) Path #3 to #4

Figure 4.11: Comparison of experimental and simulated time signals of direct and diagonal paths of all pristine units. A bound of ±2 standard deviations of the simulation signal is represented by light black color.

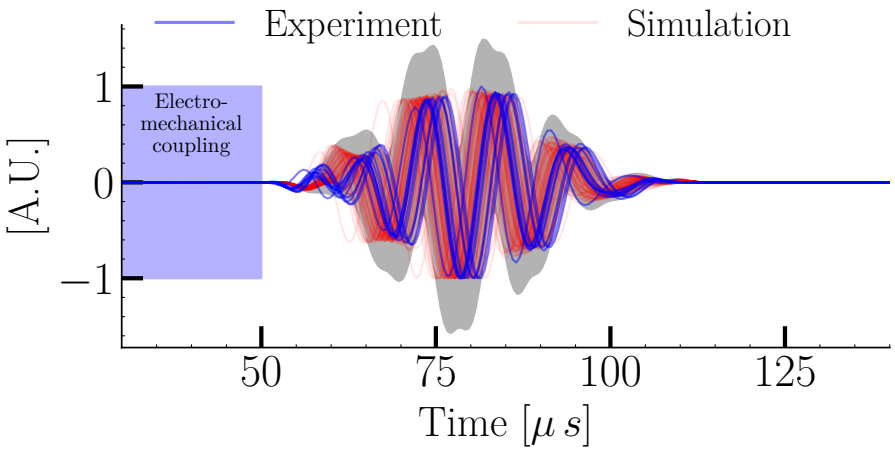

(a) Path #1 to #3

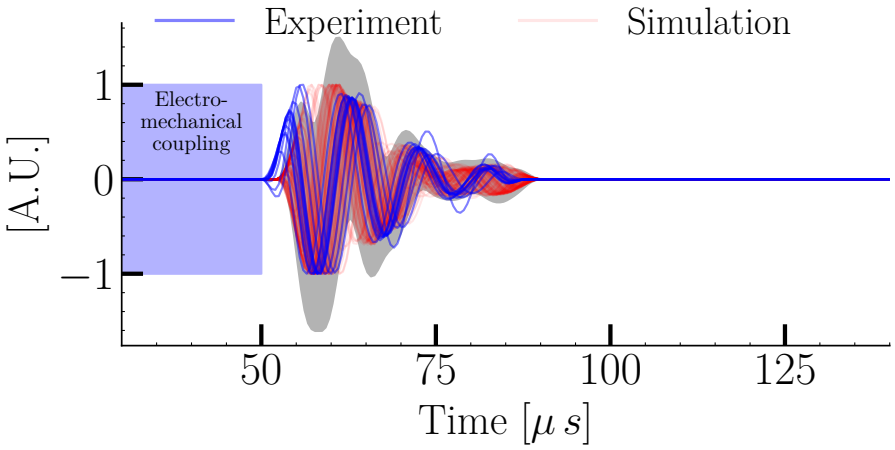

(b) Path #1 to #4

Figure 4.12: Comparison of experimental and simulated time signals of indirect paths of all pristine units. A bound of ±2 standard deviations of the simulation signal is represented by light black color.

as defined below:

$$DI = \frac{\|R_p(t) - R_D(t)\|_2}{\|R_p(t)\|_2} \tag{4.1}$$

where $\|\cdot\|_2$ denotes L2-norm, while $R_p(t)$ and $R_D(t)$ represent pristine and damage signals, respectively. DI is calculated for both simulated and experimental time signals of pristine and damaged units and are denoted as simulated DI and experimental DI datasets. Both simulated and experimental DI datasets show a good agreement in Path #1 to #2 and Path #1 to #3, as shown in Figure 4.15. In contrast, the entire experimental DI dataset in Path #3 to #4 and Path #1 to #4 is slightly smaller than the simulated DI dataset, which may be due to the crack not being straightly elongated during the increment of the

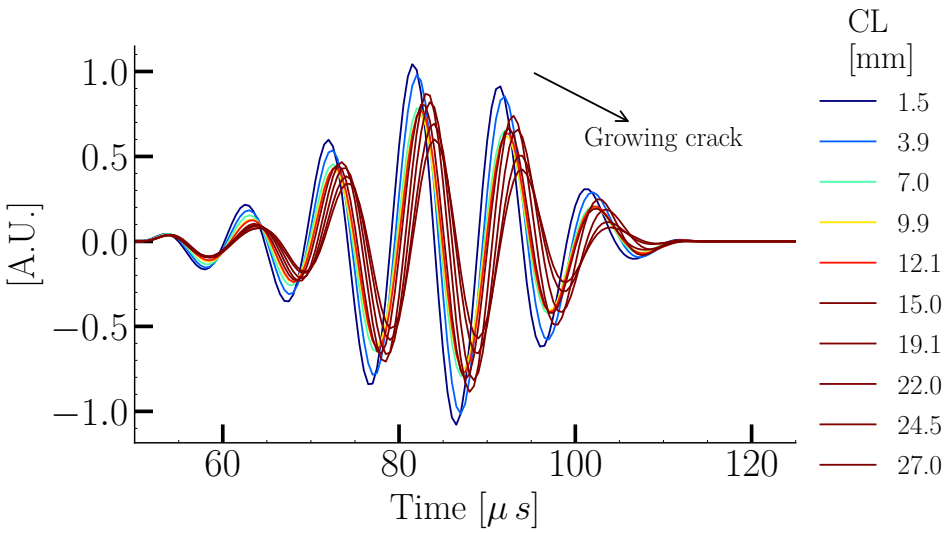

(a) Experimental damaged signal

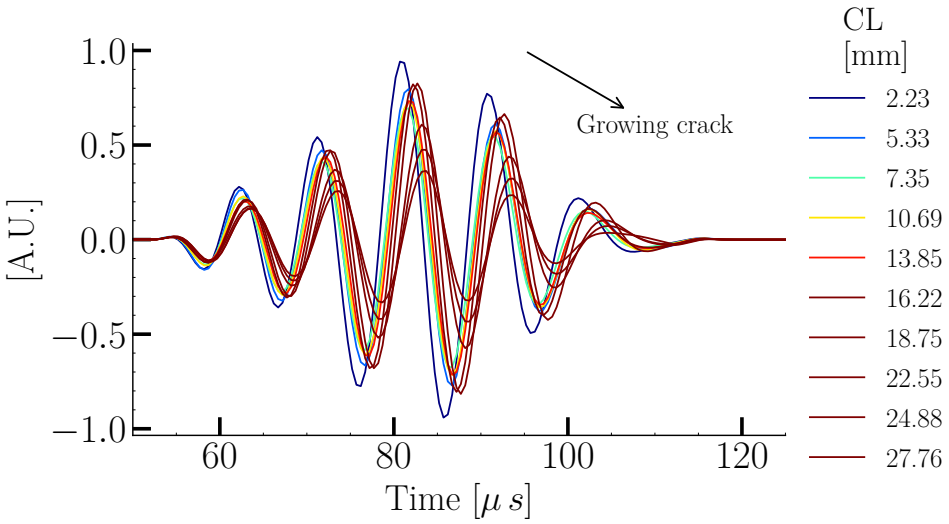

(b) Simulated damaged signals

Figure 4.13: Crack length effect over the damaged signals of Path #1 to #2 of simulated and experimental damaged units for any randomly selected one unit.

crack length in the experiment, as shown in Figure 4.14(a). Furthermore, Figures 4.15(a) and 4.15(b) show that the DI increases with the crack length when a crack is between the emitter and receiver transducer path, i.e., direct path (Path #1 to #2) and diagonal path (Path #3 to #4). Note that DI increases rapidly along the crack length in the direct path up to 4.5 mm crack length, then gradually increases to 21 mm, and then begins to decrease with crack length. In comparison, the DI in the diagonal path exhibits smaller oscillations with the crack length while maintaining an increasing trend. A similar oscillating effect is observed in two other paths, Path #1 to #3 and Path #1 to #4, while the amplitude of DI is much lower than that of the direct and diagonal paths, as shown in Figures 4.15(c)

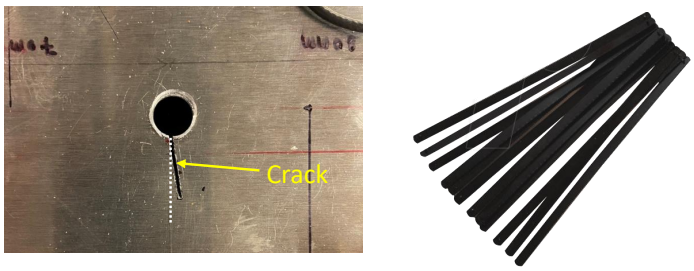

(a) Carck length (b) Thin saw cutter

Figure 4.14: Crack growth during experiment with a thin saw tooth cutter.

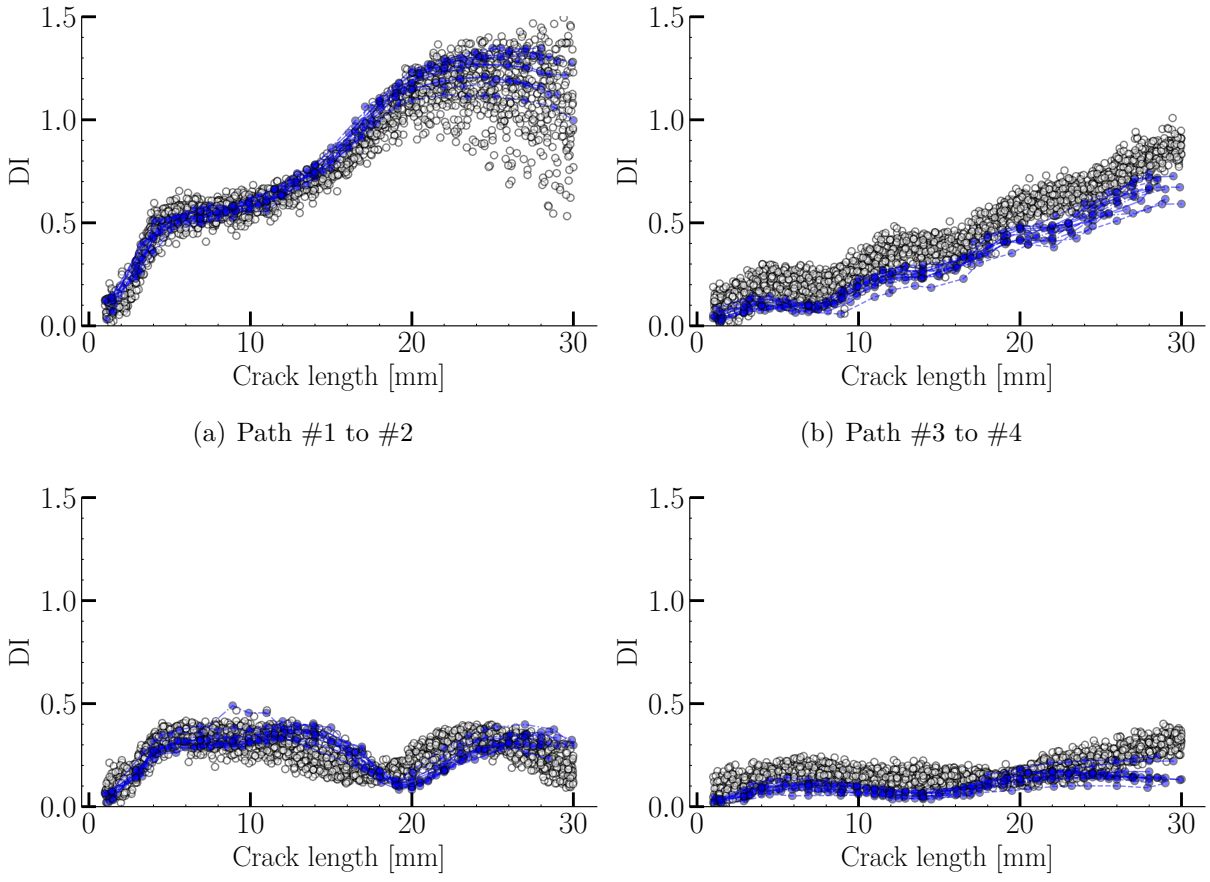

(a) Path #1 to #2 (b) Path #3 to #4

(c) Path #1 to #3 (d) Path #1 to #4

Figure 4.15: Experimental (blue ∘ marker) and simulated (white ∘ marker) damage index variations with crack length in the presence of variabilities at 100 kHz presented for all units (Experimental units are 12 and simulation units are 98[6]).

and 4.15(d).

This oscillating, i.e., non-linear behavior depends on the crack interaction with GWs, which means that the received GW signals can undergo diffraction (from the tip of the crack length), transmission, reflection, mode conversion, and interference, depending on

how waves incident the crack, as mentioned in [158]. To understand more about crack

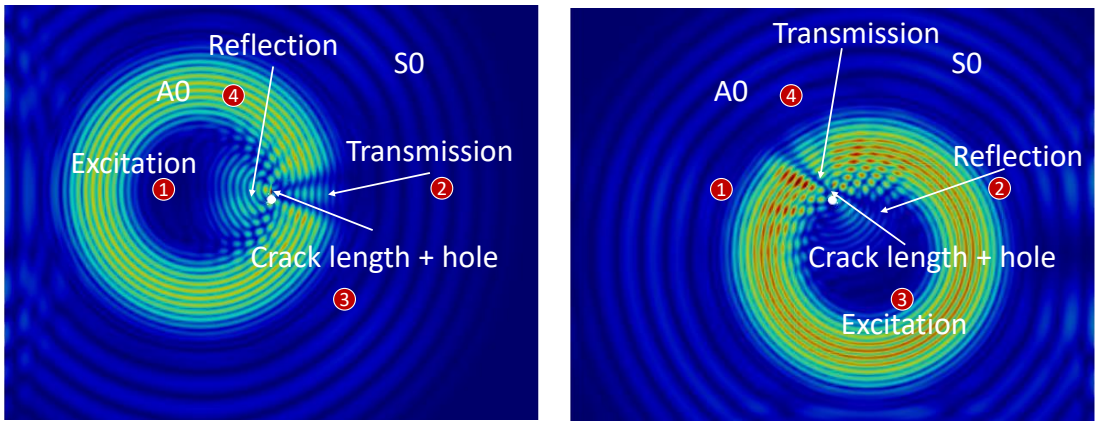

(a) Emitter #1 (b) Emitter #3

Figure 4.16: Two snapshots of GWs interaction with hole and crack length (15 mm) obtained from CIVA (a) Emitter #1 and (b) Emitter #3.

interactions with GWs, two snapshots of crack lengths of 15 mm from the CIVA simulation tool are shown in Figure 4.16. It is observed in Figure 4.16(a) that when the emitter is #1, then receiver #2 records primarily the transmission of waves from the crack. At the same time, receivers #3 and #4 record the reflection and transmission of waves or interference. Similarly, Figure 4.16(b) can be explained that when the emitter is #3, then receiver #4 records interference of transmission, reflection, and may diffraction of waves from the tip of the crack as it follows a diagonal path. Therefore, non-linear behavior is observed in DI because of their constructive and destructive interventions.

Moreover, it should also be noted that the DI of Path #1 to #2 has a higher sensitivity to the crack length than the other DI paths. These DI slopes are steeper for shorter crack lengths (up to 4.5 mm) than for higher ones. Although, at 100 kHz excitation frequency, only the A_0 mode dominates, i.e., the amplitude of the A_0 mode is greater than that of the S_0 mode while the half-wavelength of A_0 mode is 7.5 mm, which exceeds the crack size, which means that DIs are effective even for short crack length. Therefore, a DI study is carried out with different wavelengths by changing the excitation frequency from 60 to 340 kHz. Two kinds of DI studies are performed based on the amplitude of the modes in the transducer excitability curve (i.e., assumed that low amplitude mode does not appear in the signal, as shown in Figure 4.3(a)), denoted as A_0 mode DI (up to 200 kHz) and S_0 mode DI (from 280 to 340 kHz). The A_0 and S_0 mode DIs are divided into four regions based on the DI trend with normalized crack length (normalized by corresponding A_0 and S_0 modes wavelength), as shown in Figure 4.17. Based on these four regions, the following points are described below:

Region 1 ($CL/\lambda < 1/4$): This region ranges from 0 to 1/4 and shows that the relation between DI and CL/λ is linear for both mode DIs, but A_0 mode DI slopes steeper than the S_0 mode DI. It is worth noting that there is significantly less effect on the slope of

[6]Two simulation unit results were corrupted during data transfer.

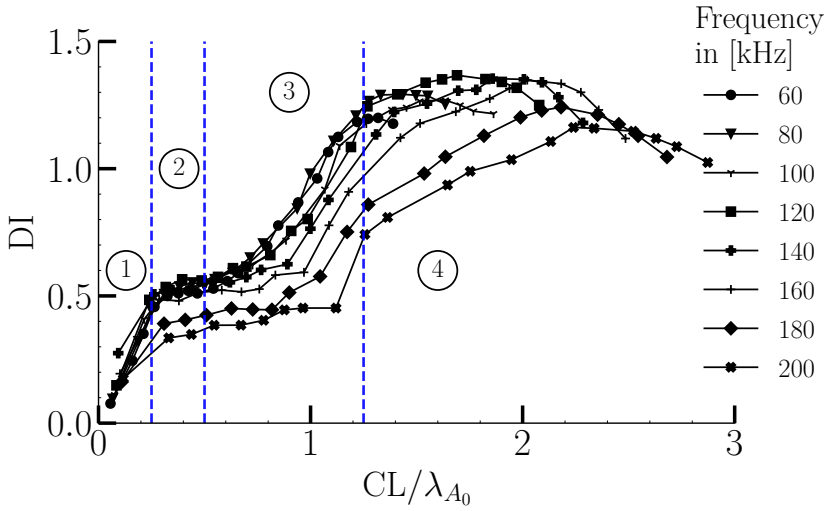

(a) A_0 mode DI

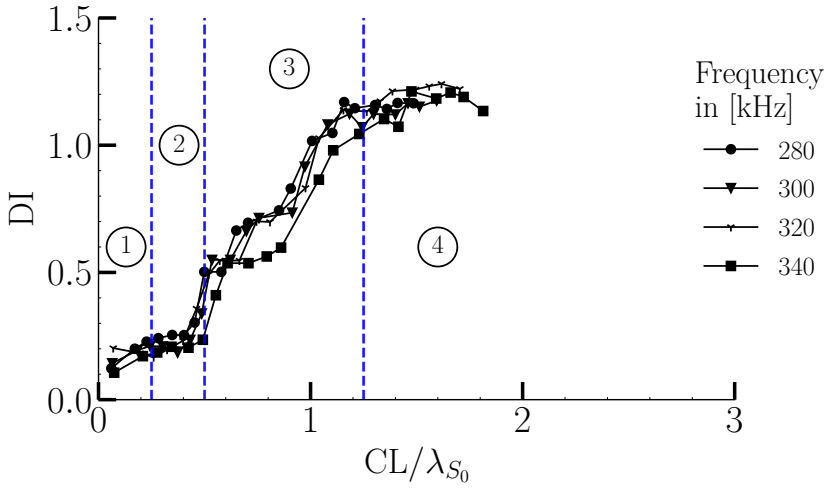

(b) S_0 mode DI

Figure 4.17: The damage index variation in Path #1 to #2 with the wavelength (λ) of the wave mode calculated on a single unit.

both mode DIs with frequency.

Region 2 ($1/4 \leq \mathrm{CL}/\lambda < 1/2$): This region starts at 1/4 and ends at 1/2, indicating that the relationship between DI and CL/λ is stable for both modes of DI. As the frequency increases, both A_0 mode DI up to 160 kHz and S_0 mode DI do not change. Whereas above 160 kHz, the A_0 mode DI begins to decrease as the amplitude of the A_0 mode decreases in the transducer excitability curve.

Region 3 ($1/2 \leq \mathrm{CL}/\lambda < 5/4$): This region is between 1/2 and 5/4 and over half the wavelength of the wave mode. It exhibits a slow increase in DI with CL/λ, but DI reaches its highest level for both modes. However, A_0 mode DI decreases with increasing frequency, while S_0 mode DI is significantly less affected by frequency.

Region 4 ($\mathrm{CL}/\lambda \geq 5/4$): This region is above 5/4, and DI reaches its maximum value with CL/λ and then begins to decrease for both modes due to the destructive and constructive interference of the waves. As the frequency increases, the peak point of the A_0 mode DI shifts to the right with decreasing values, while the S_0 mode DI is not significantly affected by the frequency.

It can be concluded that lower frequencies are more effective for A_0 mode DI with crack length, while for higher frequencies, S_0 mode DI is more effective. However, the DI values trend is not much changed in both modes when both modes have the highest amplitude in the transducer excitability curve. For example, as shown in Figure 4.17, 100 kHz (highest wave amplitude for A_0 mode) and 300 kHz (highest wave amplitude for S_0 mode) behave similar DI trend with CL/λ in both modes DI. Note that when the signal has both modes with roughly the same ratio of amplitude, then it is impossible to say which mode is interacting with the crack and their associated wavelengths. Therefore, three in between frequencies (220, 240, and 260 kHz) are not described here.

4.3 Conclusion

A complete methodology is presented for the MAPOD and experimental POD study of a crack growing from a hole in an aluminum plate to obtain the stochastic response in GW signals. It is observed that the MAPOD strategy with influencing variability reproduces all sources of variability in their output response, similar to an experimental study. The variability obtained in both the DI and time domain signals from the simulation study agrees well with the experimental study. Even the simulation study provides a wider range in output variability, thanks to considering the large temperature variation in the simulation study. The study also identified that the direct and diagonal paths are the most sensitive for crack growth detection with this definition of DI. Furthermore, a wavelength interaction with the crack length is studied, and four regions are indicated based on their DI change with the crack length in the direct path and the excitation frequency. It is found that S_0 mode DI is less effective than A_0 mode DI for lower frequencies, but both show roughly equal response in DI for higher frequencies. In the next chapter, i.e., step 4, the performance is quantified through a POD curve based on two recent statistical methods on experimental and simulated DI datasets computed from this study.

CHAPTER 5

Probability of detection curves for SHM

Outline

5.1 Introduction

Probability of detection (POD) applied in Nondestructive Testing was started at NASA in the early 1970s, while the concept imported from other technology sectors such as telecommunications, radar, and medicine [159]. To illustrate the POD, suppose an operator wishes to guarantee that no defect of size above 10 mm lies in several similar structures using an inspection technique. Will he always detect a 10 mm defect, or will he only catch it 80% of the time? POD is the answer to this question, ensuring the reliability of inspection technology. Initially, POD for the evaluation of NDT methods was based on the ratio of the number of defects n_d detected (or above a given detection threshold) by the number

of defects/samples N_d inspected. Then, POD can be estimated using the probability law $\frac{n_d}{N_d}$, which assigns one POD value for each set of defect sizes in the samples. Later on, it is found that separating cracks by length makes more sense since larger defect sizes are more accessible to detection than smaller ones [100]. Subsequently, two statistical POD computation methods performed on a continuous scale of defect size: 1) Hit and miss and 2) Signal response, have been introduced, as reported in MIL-HDBK-1823A [86]. Of these two statistical methods, the signal response is one of the most widely accepted and currently used methods for POD calculation in the NDT system. However, conventional statistical methods cannot be directly applied to SHM systems, especially for monitoring repeated measurements of cracks growing over time due to the statistical assumption of data independency that is not respected, as explained in chapter 4.

Therefore, this chapter uses two alternatives and suitable statistical methods recently proposed by Meeker et al. [110] to estimate a POD curve for the SHM system. These methods have been modified and expanded on conventional statistical methods to handle repeated measures data properly. The purpose of this chapter is to describe how these methods can be applied in SHM POD studies and how they differ from existing methods. A complete POD curve illustration and terminology are mentioned in the introduction chapter (in Figure 1.5). Both experimental and simulated DI datasets from the use case of increasing crack length from a hole in an aluminum plate under the influencing variabilities obtained from the previous chapter are used as a measured response to make a detection decision through the POD curve. Note again that the experimental DI dataset consists of 12 units, each containing 21 crack length responses, whereas the simulated DI dataset contains 98[1] units and 20 crack length responses each.

This chapter is organized as follows: The first section presents all the assumptions and the process of POD curve estimation through the traditional signal response method. The second section describes the limitation of signal response and the need for a new statistical method for repeated measurements in the SHM system. Two revisited statistical methods follow this section: *length-at-detection* and *random effects*, which are described in detail and demonstrated on experimental and simulated DI datasets for POD curve estimation. Finally, both new statistical methods are compared qualitatively, and an additional study is presented to calculate a sample size to estimate $a_{90|95}$ based on the *random effects* method.

5.2 Signal response method

Signal response method for POD computation is also known as $\hat{a}$ vs. a, where $\hat{a}$ denotes measured response and a denotes the crack length. For simplicity here, we denote $\hat{a}$ as y and a as x. The signal response is a linear regression analysis between response y and crack length x, as mentioned below:

$$y = \beta_0 + \beta_1 x + \epsilon \tag{5.1}$$

[1]Two simulation unit results were corrupted during data transfer.

where β_0 and β_1 are regression coefficients of a linear model, and $\epsilon \sim \mathbb{N}(0, \tau^2)$ is an error term, which follows the Normal distribution having zero mean and standard deviation τ^2. The computation of the POD curve based on the signal response assumes that the response variable y follows the Normal distribution for an observed crack length x. This means that a linear model Equation (5.1) can be expressed in terms of $Pr\left(y \mid x, \theta\right) = \mathbb{N}\left(y \mid \mu(x), \sigma(x)\right)$, where $\mu(x) = \beta_0 + \beta_1 x$ and $\sigma(x) = \tau^2$ (constant with x) are the mean and variance values of a probability distribution of the response y at an observed x, while θ is a model parameter including of β_0, β_1, and τ^2. Therefore, the dataset, i.e., x and y for signal response analysis must respect certain assumptions:

1. Data linearity: linear relationship between x and y.

2. Homoscedasticity: variance σ in response y must be constant with the crack length x, meaning the scatter of data points must be uniform along a straight line.

3. The response/observation y should be independent and identically distributed (i.i.d), i.e., uncorrelated.

4. The error term must follow the Normal distributions.

Additionally, an inspection system always has inherent noise during real-time inspections which increases the response level even when damage is not present in the structure. Therefore, a threshold (y_{th}) is often needed to avoid background noise for computing the POD curve. Then, as shown in Figure 5.1, the POD estimate of an observed crack length x is an integration of the distribution of the response variable y over the threshold as shown below:

$$\begin{aligned} POD(x) &= Pr\left(y > y_{th} \mid x, \Theta\right) \\ &= 1 - Pr\left(y < y_{th} \mid x, \Theta\right) \\ &= 1 - \int_{-\infty}^{y_{th}} Pr(y \mid x, \Theta)\, dy \\ &\because Pr\left(y \mid x, \Theta\right) = \mathbb{N}\left(y \mid \mu(x), \tau^2\right) \\ &\implies \int_{-\infty}^{y_{th}} Pr(y \mid x, \Theta) dy = \Phi_{\text{Norm}}[\mathbf{Z}] \\ &= 1 - \Phi_{\text{Norm}}[\mathbf{Z}] \end{aligned} \tag{5.2}$$

where $\Phi_{\text{Norm}}[\mathbf{Z}]$ is a Cumulative Density Function (CDF) of standard Normal distribution, and $\mathbf{Z}$ is:

$$\begin{aligned} \mathbf{Z} &= \frac{y_{th} - \mu(x)}{\tau^2} \\ &= \frac{y_{th} - (\beta_0 + \beta_1 x)}{\tau^2} \end{aligned}$$

The model parameter $\Theta = [\beta_0, \beta_1, \tau^2]$ is generally estimated based on maximum likelihood estimation (MLE) from the best fit of observed datasets, denoted $\hat{\Theta}_{MLE}$. This allows

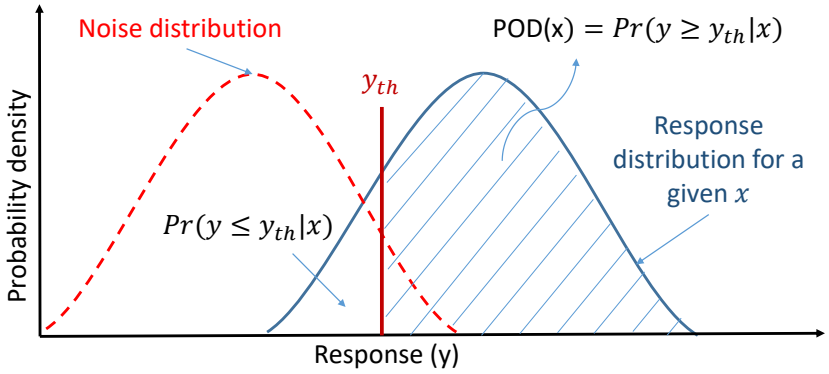

Figure 5.1: The illustration of Equation (5.2) for an observed x.

to estimate $\widehat{POD}(x)$ at a observed crack length x

$$\widehat{POD}(x) = 1 - \Phi_{\text{Norm}}\left[\frac{y_{th} - (\hat{\beta}_0 + \hat{\beta}_1 x)}{\hat{\tau}^2}\right] \tag{5.3}$$

In addition, a 95% confidence interval of $\widehat{POD}(x)$ at each x value, denoted as a $\widehat{POD}_{95}(x)$, is also generally estimated due to the limited amount of data. It provides lower uncertainty bound in the computation of $\widehat{POD}(x)$, which reduces as the number of data increases. The details about a confidence interval computation for the signal response can be found in MIL-HDBK-1823A and ENIQ report 41 [86].

5.2.1 Defining x_{90} and $x_{90|95}$ values

The different x values in Equation 5.3 can estimate the entire POD curve, while the two x_{90} and $x_{90|95}$ popular values are often calculated to compare different POD curves easily. The x_{90} value represents the crack length where the POD value is 90%, while the $x_{90|95}$ value represents a 95% confidence of upper bound for x_{90} value. The x_{90} value can be easily calculated from Equation 5.3 after substituting 0.9 at $\widehat{POD}(x)$, as shown below:

$$1 - \Phi_{\text{Norm}}\left[\frac{y_{th} - (\hat{\beta}_0 + \hat{\beta}_1 x_{90})}{\hat{\tau}^2}\right] = 0.9 \tag{5.4}$$

$$\frac{y_{th} - \hat{\beta}_0 + \hat{\tau}^2 \Phi^{-1}_{\text{Norm}}[0.1]}{\hat{\beta}_1} = x_{90} \tag{5.5}$$

where $\Phi^{-1}_{\text{Norm}}[0.1]$ is CDF value of Normal distribution at 0.1 that can be obtained from any standard statistical book. Similarly, $x_{90|95}$ is corresponding value of $\widehat{POD}_{95}(x) = 0.9$ in the curve, as explained in [86]. In practice, this value $x_{90|95}$ is generally used in industry to claim the performances of an inspection system. In addition, the absolute difference value between the $x_{90|95}$ and x_{90} helps in comparing the confidence interval thicknesses in the POD curves denoted as $\delta_{95|90-90}$.

5.3 Probability of detection methods for SHM

The assumptions of signal response method are similar to Normal linear regression, which can be found in many statistics books [160–162]. A major limitation of using the existing signal response method in SHM is the assumption of the independent responses, which is not verified in SHM. Since the sensors are permanently immobilized on the structure, they repeatedly measure the crack growth response, making the responses dependent. In the SHM system, these measurements form structured group data where a group is called a unit (aluminum plate with a sensor attached), and each unit contains responses to the crack length. Note that two randomly selected responses from the same unit are more similar than two responses selected from different units because the sensors are identical in one unit [163]. From a statistical perspective, this leads to a within-unit correlation[2]. Therefore, signal response analysis is not applicable for SHM POD calculation in the case of a growing crack. It is also worth noting that in the SHM system, dependent or independent responses depend on the type of inspections. For example, an inspection of a one-time impact load on a structure can yield only one response from a single unit, making responses independent. Therefore, a POD study can be performed using conventional statistical methods but would require one structure with a sensor network for each defect, making it extremely expensive too.

Nevertheless, two newly proposed statistical methods for SHM POD: *length-at-detection* and *random effects* [110], are explained and applied to the experimental and simulated DI datasets of repeated measurements in the following subsequent sections. Since these methods are more generalizations of traditional statistical methods, i.e., based on linear regression, they require linearity check between the crack length and the observed response.

5.3.1 Linearity and threshold decision

The relationship between x and y can be transform in four possible ways [165]: 1) y vs. x, 2) y vs. $\log(x)$, 3) $\log(y)$ vs. $\log(x)$, and 4) $\log(y)$ vs. x, as shown in Figure 5.2. Note that this study considers DI only for Path #1 to #2, which has a more significant sensitivity toward crack length, as mentioned in the previous chapter section 4.2.6. Generally, the choice of transformed relationship between x and y depends on the best fit parameter of the linear line, e.g., coefficient of determination (R^2) value. However, visually can be interpreted that Figure 5.2(d) is more linear compared to the other three plots for regions 2 and 3. It is also noted that region 1 in all four plots is linear but is far less than the half wavelength (7.5 mm) of the wave at 100 kHz, and corresponding DI values are much smaller. At the same time, region 4 shows heteroscedasticity, i.e., scatter of data points not uniform along the crack length. Therefore, at this moment, from Figure 5.2(d), both regions 1 and 4 have been dropped, and only regions 2 and 3 are considered for further

[2]As mentioned by Hoff [164], form an example, i.e., let y_{ij} be the i^{th} response of j^{th} unit, and $y_{ij} = \mu + \gamma_j + \epsilon_{ij}$, where $\{\gamma_1 \dots \gamma_m\}$ represent heterogeneity of group, μ is constant, and $\{\epsilon_{1j} \dots \epsilon_{n_j j}\}$ represent heterogeneity of samples within unit j. Suppose $var[\gamma_j] = \tau^2$ and $var[\epsilon_{ij}] = \sigma^2$ are variances of unit and within units. Then correlation between two random variables is $Cor[y_{i_1 j_1}, y_{i_2 j_2}] = \frac{\tau^2}{\tau^2+\sigma^2}$ if $j_1 = j_2$ otherwise is 0.

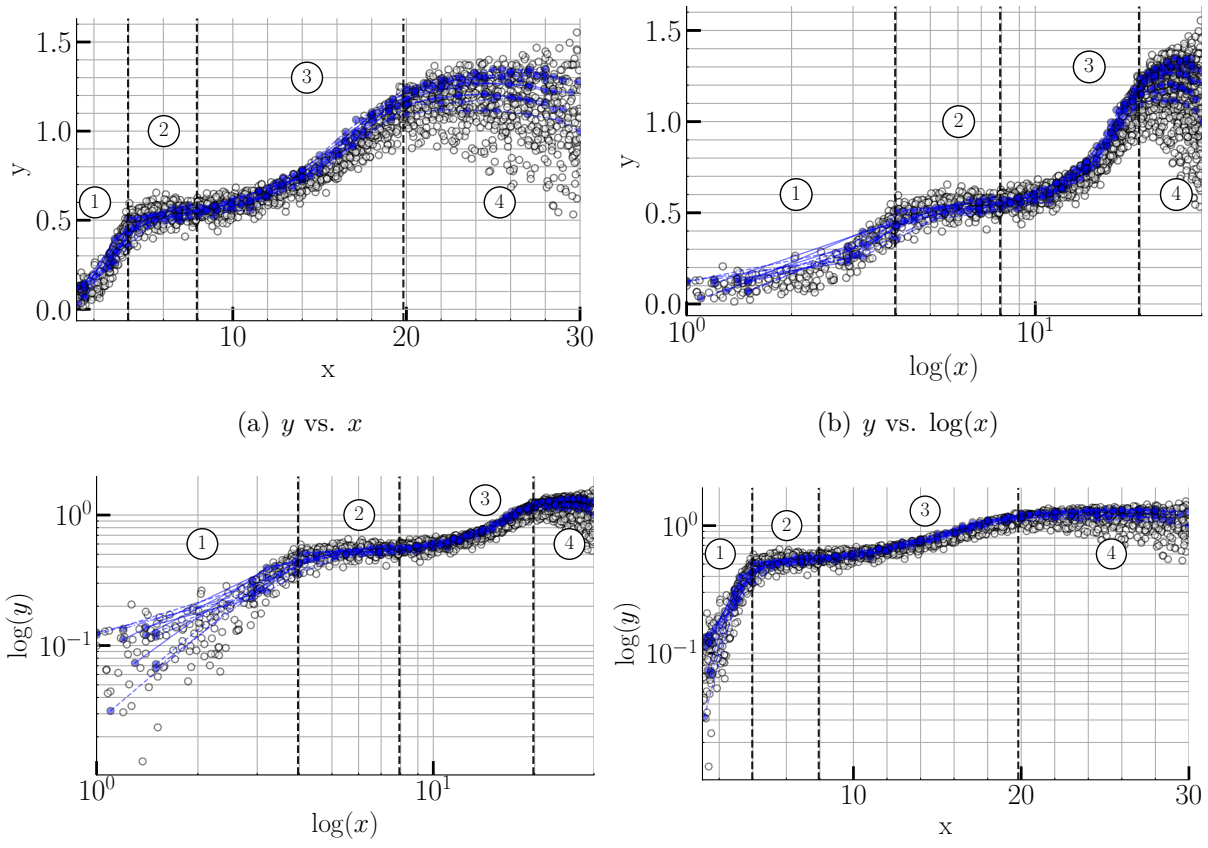

(a) y vs. x

(b) y vs. $\log(x)$

(c) $\log(y)$ vs. $\log(x)$

(d) $\log(y)$ vs. x

Figure 5.2: Four possible representations of experimental (blue ∘ marker) and simulated (white ∘ marker) DI of Path #1 to #2 with crack length.

SHM POD study. Note that R^2 values for each unit of Figure 5.2(d) are shown in Figure 5.3.

The arbitrary detection threshold is chosen to be 0.6, which is slightly above that in region 2. Ideally, the threshold should be fixed in real-time in the presence of environmental noise, but that study is not presented here. Although lowering the threshold will improve the POD curve, it also increases the probability of false alarms (PFA).

5.3.2 *Length-at-detection* method

The *length-at-detection* (LaD) method addresses the dependency issue in repeatedly acquired SHM responses during the growing cracks [110]. This method uses only the first detected crack length, i.e., when the response from each unit reaches the threshold line, the corresponding crack length value is called the first detected crack length. To achieve this, linear regression fits a linear line to each unit to calculate the intersection point between the linear line and a threshold line, i.e., computes only first-time threshold crossing response values of crack length. These crack length values are defined as LaD values. Since it uses only one crack length from each unit, the dependency in repeated responses

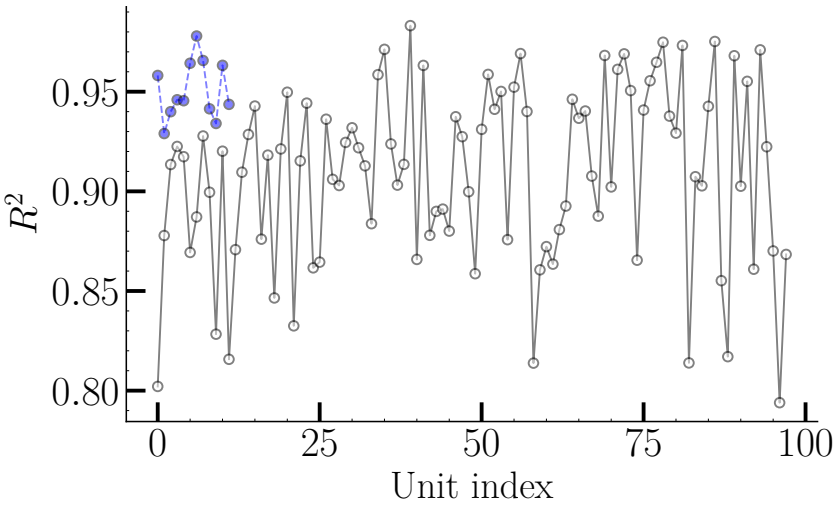

Figure 5.3: Coefficient of determination (R^2) values for both experimental (in light blue) and simulated (in gray) units linear regressions.

does not affect the POD computation, i.e., one unit provides only one LaD value.

LaD method based POD computation relies on an underlying statistical distribution of the first detected crack length, i.e., LaD values distribution. Suppose $x_1, x_2, \ldots x_N$ denote LaD values of N number of units and assume that these LaD values follow a normal distribution with a sample mean $\hat{\mu}$ and variance $\hat{\sigma}$ of LaD values. Then, the POD at crack length x_{LaD} can be estimated as,

$$\widehat{POD}(x_{LaD}) = Pr(x \leq x_{LaD}) = \Phi_{\text{Norm}}\left(\frac{x_{LaD} - \hat{\mu}}{\hat{\sigma}}\right) \tag{5.6}$$

where $\Phi_{\text{Norm}}[\mathbf{Z}]$ is a CDF of standard Normal distribution, and $\mathbf{Z}$ is $\frac{x_{LaD}-\hat{\mu}}{\hat{\sigma}}$. The 95% confidence interval of the lower bound for $\widehat{POD}(x_{LaD})$[3] can be calculated from the non-central-t distribution as follows:

$$\widehat{POD}_{95}(x_{LaD}) = \Phi_{\text{Norm}}\left(\frac{\delta}{\sqrt{N}}\right) \tag{5.7}$$

where δ is the non-central parameter, and the computation of δ relies on CDF of non-central-t distribution which is represented as $pt(k\sqrt{N}; N-1, \delta) = 1 - 0.05$, where pt is a symbol for the CDF function of non-central-t distribution and $k = \left(\frac{x_{LaD}-\hat{\mu}}{\hat{\sigma}}\right)$ represents the observed value. The value of δ for given k and N can be found in the textbook of Meeker et al. [166], which is substituted in Equation (5.7) to compute 95% confidence of $\widehat{POD}(x_{LaD})$ for each x_{LaD} values. Similarly, as mentioned in the section 5.2.1, x_{90} and $x_{90|95}$ popular values can be computed from Equations (5.6) and (5.7), respectively.

[3] $POD(x_{LaD})$ is represented as $\widehat{POD}(x_{LaD})$ because the POD on x_{LAD} is based on an approximate sample mean and standard deviation calculation.

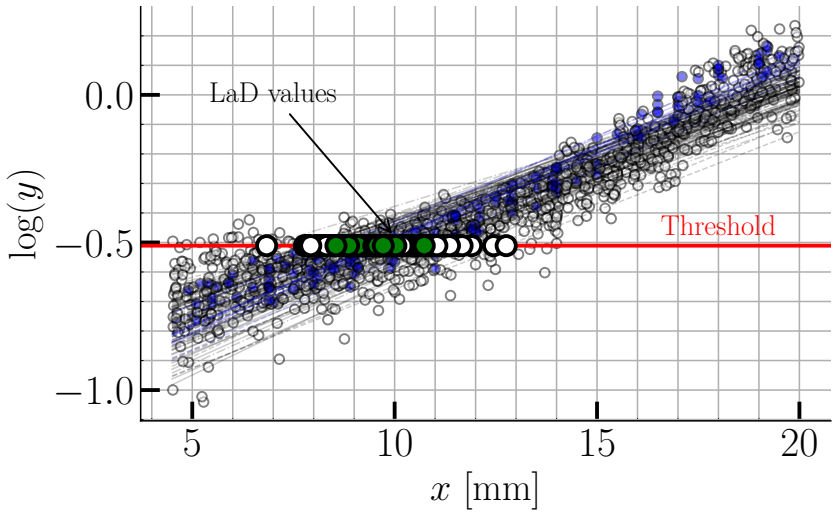

Figure 5.4: $\log(y)$ and x response plot with a linear regression line for each unit of both experimental (denoted in blue ∘ marker and dashed line --) and simulated (denoted in white ∘ marker and black dashed line --) DI datasets. The LaD values for both experimental (denoted in green ∘ marker) and simulated (denoted in bigger white ∘ marker) DI datasets at the threshold line (denoted in solid red -).

Application of LaD

Both experimental and simulated DI datasets are fitted with linear regression lines computed based on the ordinary least square method, as shown in Figure 5.4. The LaD values are calculated based on the intersections between all linear lines and a threshold line, i.e., those crack sizes in which the DI crosses the threshold for the first time.

A Quantile-Quantile (QQ), i.e., probability plot, is used to assess the adequacy of underlying statistical distribution for LaD values. QQ plot is a graphical method for comparing the distribution of observed value with a particular theoretical distribution through plotting their quantities against each other. If the quantile points lie approximately on a straight line, then the observed value distribution is similar to the theoretical distribution. As shown in Figure 5.5(a), LaD values as observed quantities are plotted against theoretical Normal distribution quantities, indicating that their quantile points lie on a straight line to provide sufficient justification that the LaD values follow a Normal distribution. Note that *length-at-detection* is not only restricted to the Normal distribution of LaD values but also for other distributions, such as Weibull, log-normal, and exponential. However, it is mandatory to check LaD values distribution once the threshold is fixed. It is also worth noting that both the experimental and simulated LAD values show an approximately Normal distribution while they are obtained from a different source of study.

The POD curve for the experimental and simulated LaD values can be estimated based on Equation (5.6) via the CDF of a Normal distribution from their sample mean and standard deviation. Similarly, their confidence intervals are calculated based on Equation (5.7), while their non-central parameter δ is obtained based on the values given in the

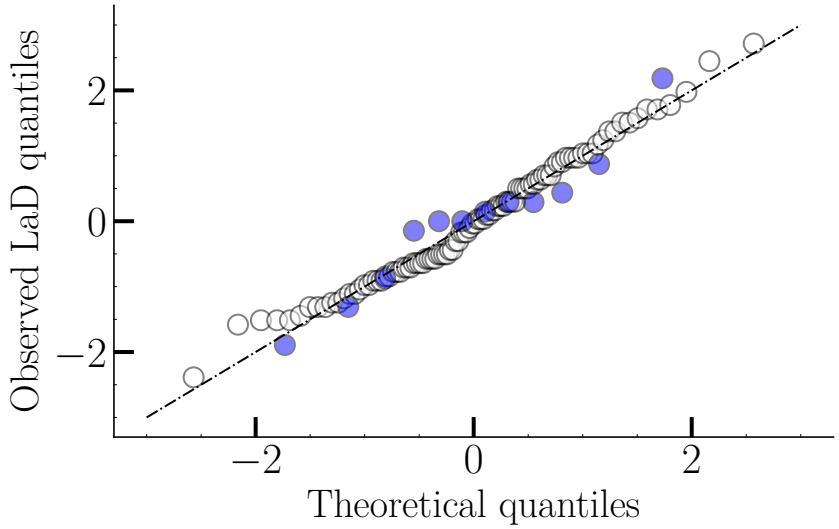

(a) QQ plot.

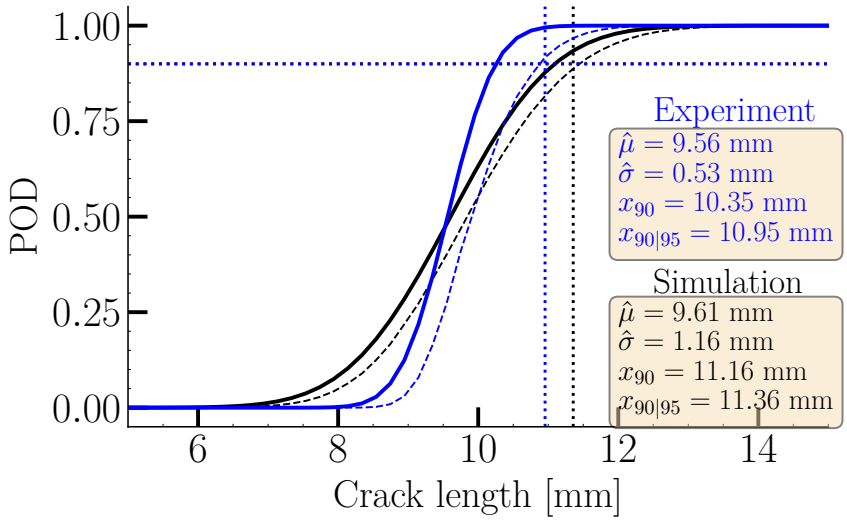

(b) POD curve with 95% confidence bound.

Figure 5.5: (a) A QQ plot of experimental (denoted in blue ∘ marker) and simulated (denoted in white ∘ marker) LaD values. (b) POD curve (denoted in solid line) with 95% confidence interval bound (denoted in dashed line - -) for both experimental (in blue) and simulated (in black) LaD values.

book [166] for each of k and N. Both the experimental and simulated POD curves with their confidence intervals are shown in Figure 5.5(b), where the confidence interval of the experimental POD is broader than that of the simulated POD due to a fewer units considered in the experimental study (N=12), i.e., the difference value $\delta_{90|95-90}$ (mentioned in section 5.2.1) value is around 0.60 mm and 0.20 mm for experimental and simulated POD curves, respectively. This is expected since the simulation study used 98 units (N=98), i.e., a large number of LaD values, that provides a narrow confidence interval

($x_{90} = 11.16\,\text{mm}$ and $x_{90|95} = 11.36\,\text{mm}$). It should also be noted that the simulation study, i.e., the MAPOD study, considered more variabilities, resulting in a larger sample standard deviation ($\hat{\sigma}$) that provides a conservative side of $x_{90|95}$ compared to the experimental POD study. Based on the *length-at-detection* POD curve study, it can be concluded that $x_{90|95}$ values for both experimental ($x_{90|95} = 10.95\,\text{mm}$) and simulated ($x_{90|95} = 11.36\,\text{mm}$) POD are pretty close, which presents good confidence in the potential of the MAPOD approach to demonstrate the performance of such an SHM system.

5.3.3 *Random effects* method

Basic principle

The *random effects* method is based on a statistical model similar to signal response which generalizes it to enable POD studies on repeated measurements in SHM [110]. It follows a similar linear relationship between the response and the crack length, as explained in the signal response method indicated in Equation (5.1). The basic idea is that each unit has its own slope and intercept, rather than just one slope and intercept for all units, i.e., model parameters are assumed to be random variables. This method assumes that each unit is sampled from a population of units; therefore, each unit is connected and contains valuable information for the other unit. It is then possible to perform a linear random-effects regression, a particular case of popularly known multilevel or hierarchical linear regression [167], so that the crack-to-crack variability of each unit can be connected through their intercepts and slopes. Therefore, a hierarchical linear regression is explained in the next section to understand properly this method.

Hierarchical linear regression

Some layers of analysis are associated with a hierarchical linear regression, as shown in Figure 5.6. The top layer is the population of units, not just the ones in the analysis, denoted as unit population. The middle layer is N units sampled from the above population. While the next layer of the hierarchy consists of multiple crack length responses per unit, often referred to as repeated measurements (on a growing crack). These layers ensure that the repeated measurements are conditionally independent at each layer. Once the unit-specific distribution is defined, such as each unit slope and intercept, the responses are independent of the top layer distribution, i.e., the responses are independent of unit population [168]. To understand appropriately, two subscripts, i and j, are used to track two pieces of information: j indicates a unit, and i indicates within each unit. For example, y_{ij} refers to a ith response in a jth unit due to x_{ij} crack length value of ith crack length in a jth unit. Then, a hierarchical linear regression analysis between response y_{ij} and crack length x_{ij} describes as follows:

$$y_{ij} = \beta_{0j} + \beta_{1j} x_{ij} + \epsilon_{ij}, i = 1 \ldots n_j, j = 1 \ldots N \tag{5.8}$$

where n_j denotes the number of crack length responses for the jth unit, while β_{0j} and β_{1j} denote intercept and slope, respectively, for the jth unit. Whereas $\epsilon_{ij} = \mathbb{N}(0, \tau^2)$ is an error term for a ith response in a jth unit, which follows a Normal distribution with

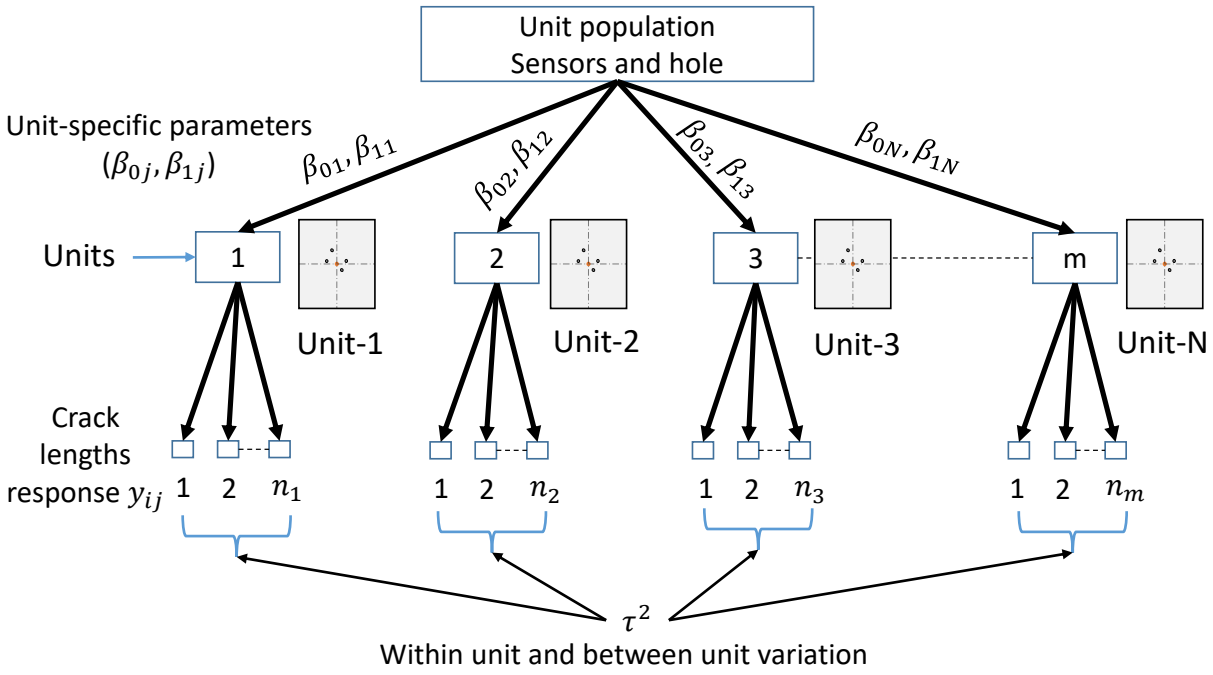

Figure 5.6: A graphical representation of a hierarchical linear regression for repeated measurements.

zero mean and standard deviation τ^2 around each response. Both β_{0j} and β_{1j} unit-specific parameters are random variables and sampled from the top layer of the hierarchy of unit population distribution assumed to have a bi-variate Normal distribution, as shown below:

$$\begin{pmatrix} \beta_{0j} \\ \beta_{1j} \end{pmatrix} \sim \mathbb{N} \begin{pmatrix} \mu_{\beta_0}, & \Sigma \\ \mu_{\beta_1} \end{pmatrix} \tag{5.9}$$

where Σ is a covariance matrix, represented as follows:

$$\Sigma = \begin{pmatrix} \sigma_{\beta_0} & 0 \\ 0 & \sigma_{\beta_1} \end{pmatrix} \begin{pmatrix} 1 & \rho \\ \rho & 1 \end{pmatrix} \begin{pmatrix} \sigma_{\beta_0} & 0 \\ 0 & \sigma_{\beta_1} \end{pmatrix}$$

where

1. μ_{β_0} and μ_{β_1} are mean of intercepts and slopes of all units, respectively.
2. σ_{β_0} and σ_{β_1} are the standard deviations of all intercepts and slopes, respectively.
3. τ^2 represents standard deviation of all response values irrespective of units.
4. ρ is a correlation coefficient between slopes and intercepts.

Then it is easy to calculate the joint distribution of the response y_{ij} after substituting the independently distributed error term ϵ_{ij} and the bi-variate distribution of the unit-specific parameters (β_{0j} and β_{1j}) (from Equation (5.9)) into Equation (5.8). Note that

the subscripts i and j can be dropped from y_{ij}. Which leads to a Normal distribution $\mathbb{N}(y_{ij} \mid \mu(x), \sigma(x))$ of y_{ij} with mean $\mu(x)$ and standard deviation $\sigma(x)$, where both $\mu(x)$ and $\sigma(x)$ can be estimated as follows:

$$\begin{aligned} E[y_{ij}] &= E[\beta_{0j} + \beta_{1j}x] + E[\epsilon_{ij}] \\ \mu(x) &= \mu_{\beta_0} + \mu_{\beta_1}x \end{aligned} \tag{5.10}$$

where E represents an expected mean symbol, $\mu(x)$ denotes the mean response of y_{ij} and x is a non-random variable (therefore dropping the subscripts i and j). While $\sigma(x)$ can be estimated by the variance $var(x) = \sigma(x)^2$ as follows:

$$\begin{aligned} var[y_{ij}] &= var[\beta_{0j} + \beta_{1j}x] + var[\epsilon_{ij}] \\ \sigma(x) &= \left(\sigma^2_{\beta_0} + \sigma^2_{\beta_1}x^2 + 2x\rho\sigma_{\beta_0}\sigma_{\beta_1} + \tau^2\right)^{1/2} \end{aligned} \tag{5.11}$$

where $\sigma(x)$ is a standard deviation of the response y_{ij}. Note that the variance of two dependent random variables (A and B), such as $var[A + kB]$ can represented as $\sigma^2_A + \sigma^2_B k^2 + 2\rho_{AB}\sigma_B\sigma_A$, where k is a constant and σ_A and σ_B are the standard deviations of A and B, respectively. While ρ_{AB} denotes the correlation coefficient between A and B.

Computation of POD

Based on the *random effects* method, the POD curve can be estimated in the same way as the signal response method. As mentioned, the response y_{ij} follows a Normal distribution that can be represented in terms of $Pr(y_{ij} \mid x, \theta) = \mathbb{N}(y_{ij} \mid \mu(x), \sigma(x))$ for an observed crack length x and θ, where θ denotes a model parameter. Then, the POD(x) value at x for a given threshold yth for the *random effects* model can be defined based on Equation (5.2) as follows:

$$POD(x) = 1 - \Phi_{\text{Norm}}(Z) \tag{5.12}$$

$\Phi_{\text{Norm}}(\mathbf{Z})$ is a CDF of standard Normal, and $\mathbf{Z}$ is:

$$\mathbf{Z} = \frac{y_{th} - \mu(x)}{\sigma(x)} = \left(\frac{y_{th} - (\mu_{\beta_0} + \mu_{\beta_1}x)}{\sqrt{\sigma^2_{\beta_0} + \sigma^2_{\beta_1}x^2 + 2x\rho\sigma_{\beta_0}\sigma_{\beta_1} + \tau^2}}\right)$$

leads to

$$POD(x) = 1 - \Phi_{Norm}\left(\frac{y_{th} - (\mu_{\beta_0} + \mu_{\beta_1}x)}{\sqrt{\sigma^2_{\beta_0} + \sigma^2_{\beta_1}x^2 + 2x\rho\sigma_{\beta_0}\sigma_{\beta_1} + \tau^2}}\right) \tag{5.13}$$

The model parameter θ, which includes $\mu_{\beta_0}, \mu_{\beta_1}, \sigma_{\beta_0}, \sigma_{\beta_1}, \rho$ and τ^2 for POD computation can be estimated by MLE or Bayesian analysis. However, using Bayesian analysis to characterize the uncertainty or confidence interval in the modeling parameters is highly recommended as suggested by Prof. Meeker [110], which is explained in the following section.

Application of *random effects* method based on Bayesian analysis

Bayesian analysis uses priors of the model parameters to calculate their posterior distributions based on Bayes' theorem [167, 168]. The aim of this study to compute the model parameters θ for POD curve computation from Equation (5.13). To achieve this, two layers of Bayesian estimation are required: in the first layer, the unit population parameters ($\mu_{\beta_0}, \mu_{\beta_1}, \sigma_{\beta_0}, \sigma_{\beta_1}$, and ρ) are denoted as hyper priors, and in the second layer, τ^2 and unit-specific parameters (β_{0j} and β_{1j}), i.e., each unit slope and intercept are considered as priors. Based on these priors and hyperpriors, the posterior distributions of model parameters are estimated on the same experimental and simulated DI datasets that were considered in *length-at-detection*, as described in section 5.3.2. As noted in [110], these priors and hyperpriors are considered weakly informative, i.e., diffuse, as mentioned below:

$$\left.\begin{aligned} \begin{bmatrix}\beta_{0j}\\ \beta_{1j}\end{bmatrix} &\sim \text{MvNormal}\begin{bmatrix}\mu_{\beta_0},\\ \mu_{\beta_1}\end{bmatrix}\quad \Sigma\begin{bmatrix}\\ \end{bmatrix}\\ \tau^2 &\sim \text{HalfCauchy}(100) \end{aligned}\right\} \quad \text{Priors} \tag{5.14}$$

$$\left\{\begin{aligned} \mu_{\beta_0} &\sim \text{Normal}(0, 100)\\ \mu_{\beta_1} &\sim \text{Normal}(0, 100)\\ \sigma_{\beta_0} &\sim \text{Exponential}(100)\\ \sigma_{\beta_1} &\sim \text{Exponential}(100)\\ \rho &\sim \text{LKJcorr}(\eta = 1) \end{aligned}\right\} \quad \text{Hyper priors} \tag{5.15}$$

The weakly informative priors and hyperpriors are associated with a much larger standard deviation of Normal distribution than measured responses in datasets. The correlation ρ hyperprior is based on the LKJcorr distribution [167], which is controlled by only a constant value parameter η. When the η value is one, the correlation prior is a uniform distribution between -1 and 1.

Then, the computation of marginal posterior distributions of the model parameters and unit-specific parameters is performed based on the PyMc3 package in a python programming language [167, 169]. A No-U-Turn (NUTS) sampling strategy based on Hamilton Monte Carlo with two chains is used to sample a large number of draws around 20000 from their marginal posterior distributions. This procedure is performed over both experimental and simulated DI datasets.

The marginal posterior distribution of model parameters with their median value[4] and highest density interval (HDI) are shown in Figures 5.7 and 5.9, respectively, for both the experimental and simulation datasets. The HDI summarizes a distribution specifying an interval that spans most of the distribution. All draws within this interval have a higher probability density than draws outside the interval. Generally, the HDI is used in the uncertainty characterization of posterior distributions as credible or confidence interval. Note that unit-specific parameters have a large number of marginal posteriors, therefore, they are not presented here. In addition, a scatter pair-plots of marginal distributions of model parameters are shown in Figures 7.2 and 7.1 (in Appendix 7). These plots

[4]For simplicity the symbol ˆ over model parameters denotes their median values of posterior distribution, e.g., the $\hat{\mu}_{\beta_0}$ median value of μ_{β_0} posterior distributions.

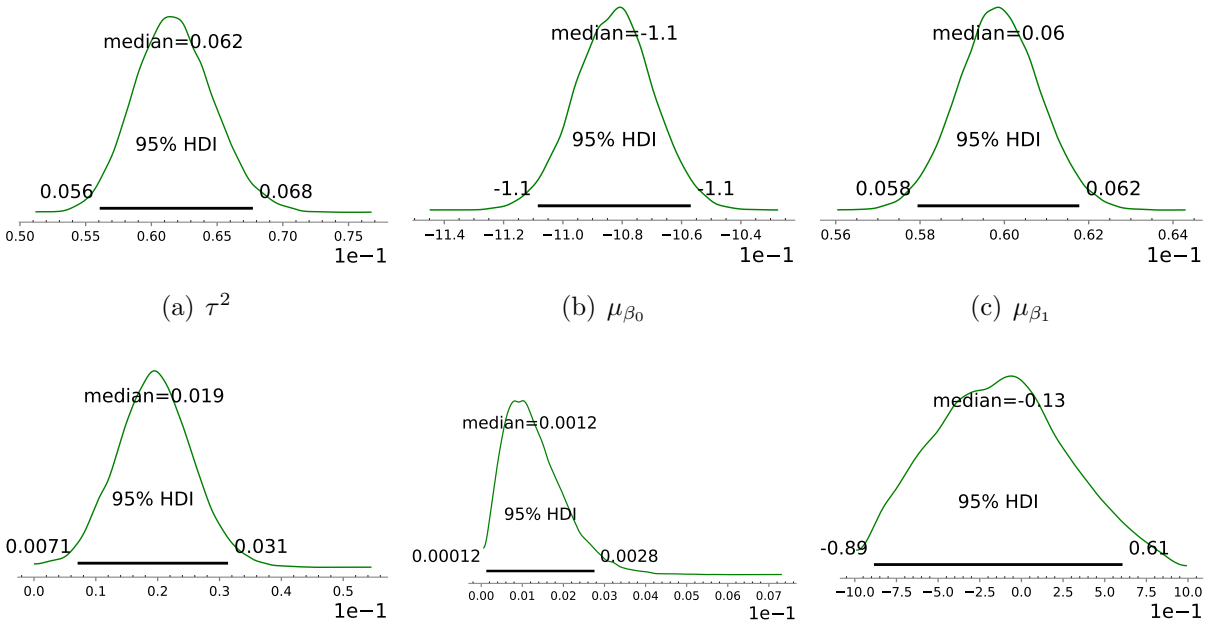

(a) τ^2 (b) μ_{β_0} (c) μ_{β_1}

(d) σ_{β_0} (e) σ_{β_1} (f) ρ

Figure 5.7: The marginal posterior distribution of model parameters with their median value and 95% HDI (denoted in black) for experimental datasets.

generally ensure and diagnose whether the draws accurately describe the joint posterior distribution of model parameters. Furthermore, a non-centered parameterization is used to avoid divergence during NUTS sampling.

Based on the median value of the marginal posterior distribution of unit-specific parameters, i.e., median values of each unit slope $\hat{\beta}_{1j}$ and intercept $\hat{\beta}_{0j}$ are used to fit a liner line for each unit. In contrast, the median values $\hat{\mu}_{\beta_0}$ and $\hat{\mu}_{\beta_1}$ are used to fit the mean response of whole units based on Equation (5.10) for both experimental and simulated DI datasets, as shown in Figure 5.8 (in thick blue straight line). It should be noted that these plots are displayed with response y as Normal distribution (in yellow color) at four crack lengths estimated based on mean and standard deviation Equations (5.10) and (5.11) of the response distribution after substituting the median values of model parameters. It defines the response strength i.e., capability at a given threshold for each crack length during inspection or monitoring. For example, the response strength at 11 mm crack length is higher than 8 mm crack length and increases as the crack length increases and changes with threshold settings.

Futhermore, POD and their 95% confidence curve are computed based on Equation (5.13), where median and 0.05 quantile values of posterior distributions of model parameters are substituted, respectively, to compute the $\widehat{POD}(x)$ and $\widehat{POD}_{95}(x)$ curve with varying x values, as shown in Figure 5.10. Similar to *length-at-detection* method, the confidence interval for experimental POD curve is wider than simulated POD curve because of the smaller number of units, i.e., the difference value $\delta_{90|95-90}$ for experimental and simulated POD curves are observed 0.61 mm and 0.36 mm, respectively. Note that $x_{90|95}$

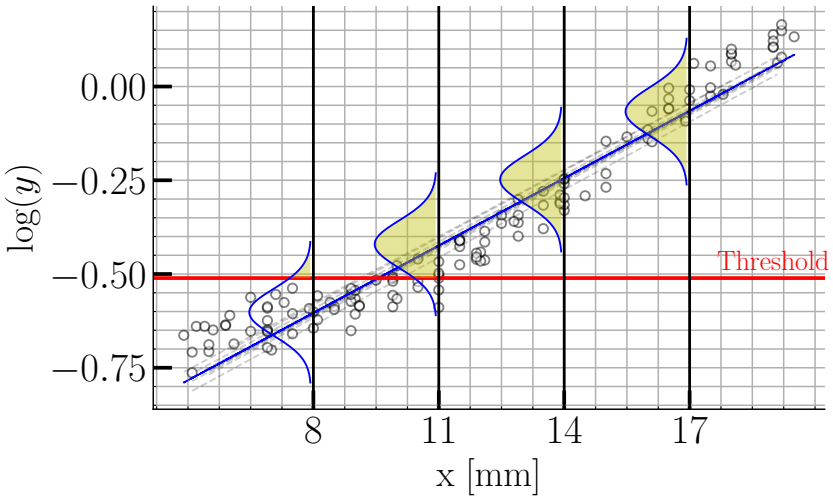

(a) Experimental DI

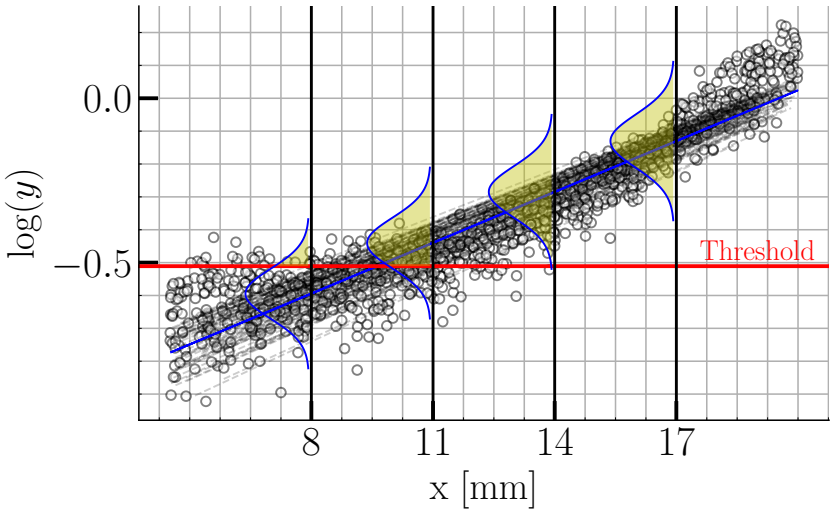

(b) Simulated DI

Figure 5.8: log(y) and x response plot with a *random effects* regression line (black dashed line --) for each unit of both (a) experimental and (b) simulated DI datasets (denoted in white ∘ marker). A mean response line (solid blue) is fitted based on the median response of marginal posterior distributions of the model parameters.

and x_{90} values for both the experimental and simulated datasets are slightly increased from the *length-at-detection* method due to the additional parameters consideration in the *random effects* method. In contrast, the *length-at-detection* method considers only the first detected crack length and is based only on two parameters, the sample mean and standard deviation.

It is also worth noting that the marginal posterior distribution of model parameters for the experimental dataset is more uncertain than for the simulated dataset due to fewer units. Specifically, the correlation coefficient distribution ρ, i.e., the correlation

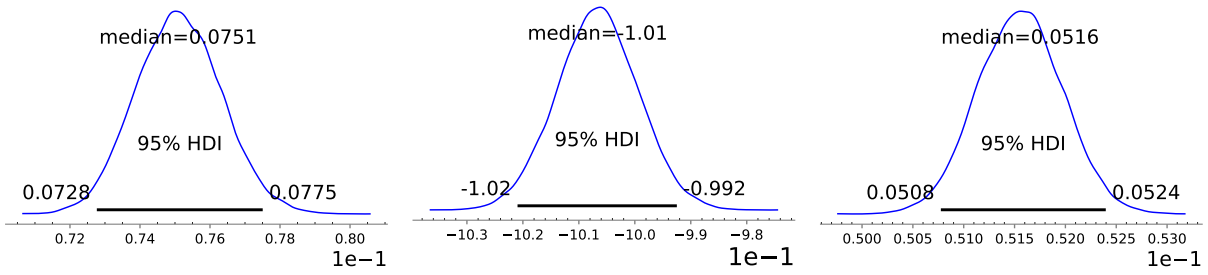

(a) τ^2 (b) μ_{β_0} (c) μ_{β_1}

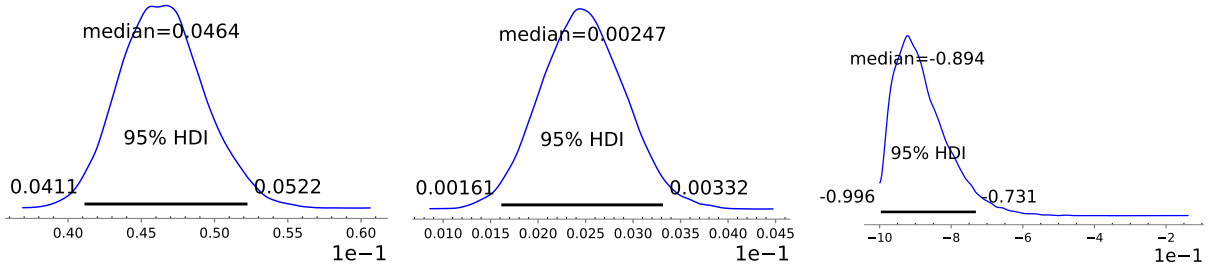

(d) σ_{β_0} (e) σ_{β_1} (f) ρ

Figure 5.9: The marginal posterior distribution of model parameters with their median value and 95% HDI (denoted in black) for simulated datasets.

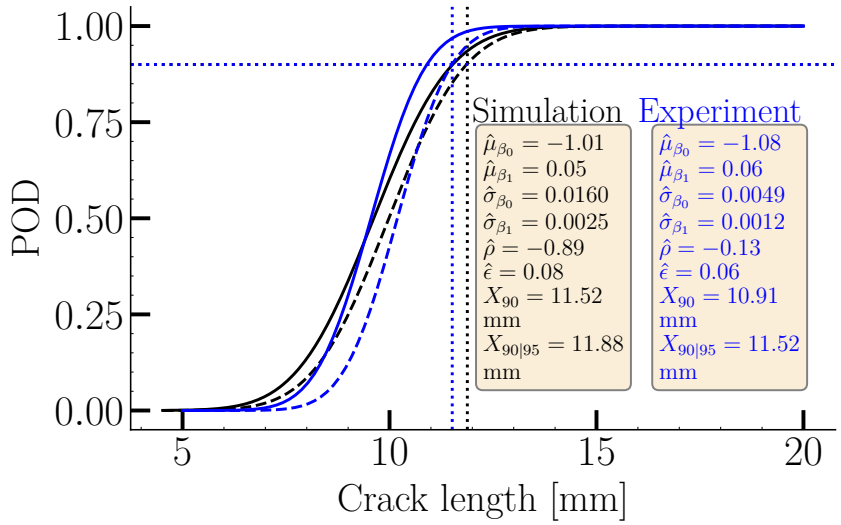

Figure 5.10: POD curve with 95% confidence interval bound (denoted in dashed line --) computed from draws of joint distribution of the posterior distribution of *random effects* model parameters for both experimental (in blue) and simulated (in black line) datasets.

coefficient between slopes and intercepts for the experimental dataset, exhibits a nearly flat distribution, as shown in Figure 5.7(f). In contrast, as shown in Figure 5.9(f), the ρ distribution for the simulated dataset with 95% HDI ranging from -1 to -0.73 achieved

high confidence via MAPOD. Also, note that $\hat{\sigma}_{\beta_1}$ marginal distribution is almost zero for both experimental and simulated datasets, i.e., the variation in slope is almost zero between units, as mentioned in Figures 5.7(e) and 5.9(e). While $\hat{\sigma}_{\beta_0}$, as mentioned in Figures 5.7(d) and 5.9(d), has some variations suggesting that a fixed slope and varying intercept regression model is also sufficient to model these experimental and simulated datasets, commonly known as the linear mixed model and also used by Kabban et al. [109] for repeated measurement.

It can be observed that the MAPOD study provides less uncertainty with more confidence over the results, while the experimental study with 12 units provides larger uncertainty. Similar to the *length-at-detection* based POD, the simulated POD curve exhibits a conservative side from the experimentally calculated POD curves due more variabilities in simulation. In the next section, both *length-at-detection* and *random effects* of POD computation methods are compared.

5.3.4 Comparison of *length-at-detection* and *random effects* methods

The *length-at-detection* method is fast, easy to perform, and understandable once the CDF of the underlying distribution is known along with the corresponding confidence interval. An important issue with the *length-at-detection* method is that it uses only the first crossing crack length values to predict the distribution of crack lengths and ignores the rest of the data. Also, an underlying distribution of *length-at-detection* values varies with threshold settings, and the calculation of confidence intervals is often based on the empirical distribution, which requires solid statistical expertise. Whereas the *random effects* method uses all the repeated SHM data to calculate the model parameters to define a POD curve, making it more reliable than *length-at-detection*. This method is a more generalized version of the signal response method, which is already documented in [86] for certification of NDT inspection systems. The significant advantage of *random effects* over *length-at-detection* is the model parameter estimation based on Bayesian analysis, which can provide informative priors to experimental datasets via the MAPOD framework, therefore requiring fewer units for experimental POD calculations. However, the *random effects* method is computationally expensive because of estimating the two layers of the posterior distribution via Bayesian analysis. Nevertheless, this computational cost is not a significant challenge in today's practices.

Furthermore, based on experimental and simulated datasets, the *random effects* method provides a slightly conservative value of $x_{90|95}$ compared to the *length-at-detection* method, as shown in Figure 5.11. Another thing that should be noted is that *random effects* and *length-at-detection* methods do not share a common statistical framework except for the assumption of a Normal distribution; Therefore, it is difficult to show comparisons based on model parameters. However, the *random effects* method estimates six parameters to define a POD curve, while the *length-at-detection* method is straightforward in analysis based on two parameters (sample mean and standard deviation). The choice between these two methods can be made based on the number of units under consideration, i.e., the *length-at-detection* method is more helpful for POD calculations when fewer units (about 10) are present because fitting the six parameters via *random effects* may not be

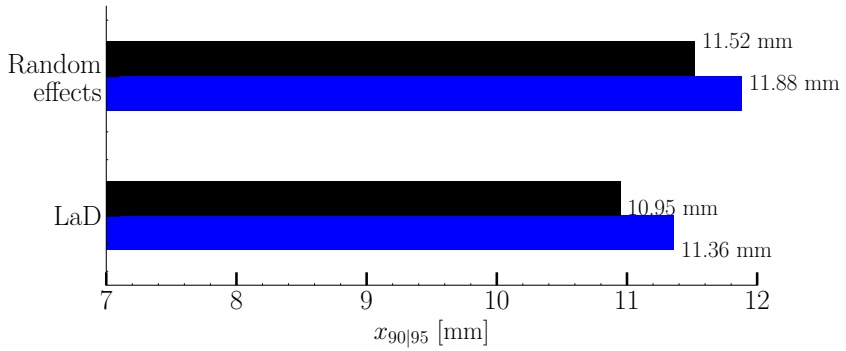

Figure 5.11: Comparison of $x_{90|95}$ values from the *length-at-detection* and *random effects* for simulated (denoted in blue) and experimental POD curves (denoted in black).

appropriate [111].

5.3.5 Sample size determination for estimating $x_{90|95}$

A study of sample size determination is carried out for estimating $x_{90|95}$ value based on the *random effects* method. This study is useful for determining how many units are needed to achieve a certain level of accuracy in the confidence interval, specifically for the upper limit of x_{90}. This is done through the *random effects* method based on the absolute difference between x_{90} and $x_{90|95}$ values, i.e., $\delta_{90|95-90} = |x_{90|95} - x_{90}|$, with the increasing number of units in sample size. The study is carried out on both experimental and simulated datasets, where the experimental and simulated datasets contain 12 and 98 units, respectively. These units are chosen randomly in increasing order of sample size without replacement for the simulated dataset, i.e., the sample size does not contain repeating units. In comparison, due to fewer units in the experimental dataset, the sample size increases with replacement, i.e., the repetition of units is allowed in the sample size of the experimental dataset. Note that repeating units in the sample size do not add any new information. For both experimental and simulated datasets based on Bayesian analysis, the *random effects* method is fitted with the increasing number of units (starting at N=3 with a step size of 3) in the sample size. As mentioned earlier, the x_{90} and $x_{90|95}$ are obtained from POD curve computation and their corresponding $\delta_{90|95-90}$ values are calculated by increasing the sample size, as shown in Figure 5.12. In addition, the six model parameters with the increasing sample size and their 95% HDI estimated through Bayesian analysis is shown in Figure 7.3 (in Appendix 7).

It can be seen that the $\delta_{90|95-90}$ values for both the experimental and simulated datasets decrease as the number of units increases in the sample size, while the $\delta_{90|95-90}$ values for the experimental datasets stabilize after 30 units due to repetition of units in sample size. Also, after 20 units of both the experimental and simulated datasets, the $\delta_{90|95-90}$ values do not show much improvement. Therefore, it shows that to get 0.6 mm of the $\delta_{90|95-90}$, it only needs 20 units, while for 0.3 mm, it needs about 60 units. For example, if a particular application allows 0.6 mm to be a $\delta_{90|95-90}$, it needs about 60 units to achieve sufficient confidence, i.e., the uncertainty on the x_{90} prediction should not exceed 0.6 mm. Note

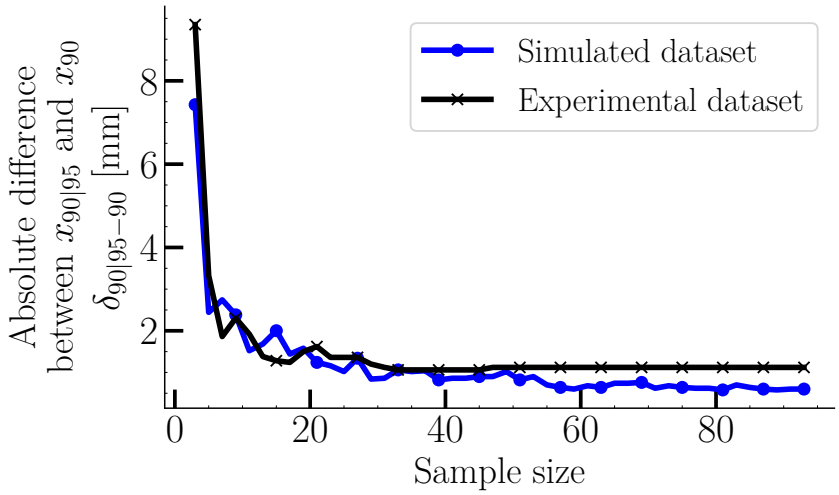

Figure 5.12: Determination of number of units in sample size with δ_{90} for estimating the required upper bound value of $x_{90|95}$.

that we are not sure that a $\delta_{90|95-90}$ value would ever be required for SHM applications. This study expects more on the value of $x_{90|95}$. However, if an x_{90} value is "good enough" but $x_{90|95}$ is not good enough, this result provides an idea of how many samples would be required to reduce $x_{90|95}$ to a good enough value (or if it is possible even then). It is also worth noting that both the experimental and simulated datasets show an almost similar trend of the $\delta_{90|95-90}$ with the increasing number of units. Therefore, the MAPOD approach could be used to decide the number of units in sample size required to reach a certain precision for any particular application.

5.4 Conclusion

This chapter has presented step 4 to the methodology of SHM POD estimation for the repeated measurements of an increasing crack length in a GWs-based SHM system through two recently proposed statistical methods: *length-at-detection* and random effect. These methods have been used for the first time to demonstrate performance via the POD curve on both experimental and simulated SHM datasets. It is exhibited that the MAPOD study agrees well with the experimental POD study, whereas the $x_{90|95}$ value of the POD curve obtained from the MAPOD is slightly conservative from the experimental study due to the larger variability in the simulation study. Similarly, the $x_{90|95}$ value obtained from *random effects* methods shows a conservative side compared to *length-at-detection* method due to considering all data of repeated measurements. A linearity check of the dataset based on the R^2 value and selecting the appropriate crack length range based on the DI variation with the crack length is described before applying these methods. In addition, a sample size requirement study based on the *random effects* method is conducted over experimental and simulated datasets to reach the precision required to estimate the $x_{90|95}$ value for a particular application.

It can be concluded that performance demonstration via MAPOD study of a plate-like isotropic structure of a growing crack length monitoring through SHM is reasonable under the considered variabilities. However, extending this methodology to other configurations requires new studies and validation of simulation tools. Nevertheless, MAPOD study based on Bayesian parameter estimation in the *random effects* method can help to reduce the number of units during a new experimental study by providing informative priors for their parameters. Note that the methodology presented for the MAPOD study was performed on a standard computer, whereas an extensive experimental campaign was carried out to obtain similar results. The feedback on the subject, described in information in Table 5.1 on this particular study, confirms the interest and potential of MAPOD methodology for SHM. Therefore, this MAPOD study opens up many potential ways to use simulations to generate large amounts of data with zero expenses, excluding computational costs.

Task		Time cost	
		Experimental POD	MAPOD (Simulation)
Configuration preparation		4 weeks	4 days
Data acquisition, generation and validation		4 weeks	1 week
Data analysis	Length-at-detection	1 second	1 second
	Random effects	5 minutes	5 minutes
Human efforts and expenditure		High	Limited

Table 5.1: Return on experience over time cost during this thesis to study MAPOD and experimental POD.

CHAPTER 6

Conclusion & perspectives

6.1 Conclusion

POD curve estimation is a significant challenge for SHM due to the high cost and lengthy experimental campaigns required. To overcome this cost, this thesis presented for the first time a validated general methodology to demonstrate the performance of guided waves based SHM in terms of the probability of detection curve through a model-assisted approach. This thesis also presented a hybrid actuator model to enable a larger range of frequency excitation in guided waves simulation. Under the considered variabilities and use case of a growing crack from a hole in an aluminum plate, the model-assisted approach is found reliable and provides a robust POD curve comparable to the experimental POD curve. Hence, this model-assisted approach can be used in similar use cases to demonstrate their performance in other industrial applications. A significant interest of the presented methodology is that it is based on the already established methodology of performance demonstration for non-destructive testing, which is widely accepted by the industry and extensively documented. However, modifications were presented to align these methodologies with the requirements of the considered SHM system, such as variabilities selection, identification and quantification of damage, and selection of the best suitable datasets. In addition, the demonstration of new statistical methods for addressing dependency in SHM data and selecting a proper linear region of datasets based on the wavelength interaction of guided waves are presented for POD computation. Finally, a study of sample size requirement is conducted based on $x_{90|95}$ value for a particular application of SHM.

This thesis benefited from the recently developed time domain transient spectral finite element schemes implemented in CIVA software to perform fast and reliable computation allowing to run the large simulation campaigns necessary for POD curve determination. Since simulation relies on many assumptions and approximations of reality, it is never straightforward to use simulations to obtain such reliable results. Therefore, chapter 2 presented CIVA simulation validations, specifically for an approximate pin force transducer model. The basic theory of the Lamb waves has been recalled based on the Navier-Lamé

equations for an isotropic plate. The previously established analytical displacement and sensor response transduction equations based on the pin force transducer model have been compared with CIVA simulations after converting the time domain signals into the frequency domain. The limits of the pin force model implemented in CIVA have been estimated by comparing a full finite element transducer model in COMSOL (FE tool), while other conditions (e.g., mesh size, geometry, and boundary conditions) were kept the same in both simulation tools. It has been observed that at high frequencies, i.e., above 200 kHz, pin force model does not match COMSOL time signals and exhibits phase shifting, amplitude differences, and extra cycles at the end of the complete burst signals.

Therefore, chapter 3 proposes a new hybrid actuator model with stress functions in both radial and normal directions to overcome the previous limitations of the pin force model while being compatible with the efficient transient spectral finite element schemes in CIVA. These stress functions consider frequency-dependent terms pre-computed from the finite element method and adhesive thickness effect terms estimated through admittance curve ratios of bounded and unbounded piezoelectric transducers. Simulated signals obtained from hybrid actuator model, pin force, and COMSOL (full piezoelectric model) over two distinct configurations have been compared to confirm the validity of the hybrid actuator model on a larger frequency range than pin force model. In addition, an experimental study has been conducted where a correlation coefficient metric is used to compare quantitatively approximated transducer models with experimental signals over a range of excitation frequencies. It has been demonstrated that the proposed hybrid actuator model accurately models the transduction signal above the first free electromechanical resonance frequency of a piezoelectric transducer.

Chapter 4 presented a complete methodology for the performance demonstration of GWs based SHM via a model-assisted approach. Experimental and simulation studies have been carried out on the use case of growing cracks from a hole on an aluminum plate. Repeated measurements have been obtained experimentally from 12 identical and independent aluminum plates with cracks up to 30 mm long to obtain stochastic time domain responses. Experimental variabilities limits have also been recorded to reproduce the variability in the output response from the simulation tool. Both experimental and model-assisted time domain signal datasets are mapped to the damage index and compared to characterize the validity of a model-assisted approach to data generation. It is noted that the experimental and simulated datasets agreed very well in both the time domain and damage index (DI) scatter points. In addition, DI scatter points exhibit higher sensitivity with crack length in the direct and diagonal sensor paths than in indirect sensor paths. However, in the indirect sensor paths, the experimental DI dataset is slightly offset from the DI of the simulated dataset because the crack not being straight during the elongation in the experiment. Some non-linear trends in DI are also marked along the crack length, which is explained by normalized crack length by the wavelength with frequency variation study and divided into four regions based on the wavelength interaction of the wave modes. From this, it is observed that DI is more influenced at higher frequencies for S_0 and lower frequencies for A_0 modes, respectively.

Chapter 5 presented two recently proposed statistical methods (*length-at-detection* and *random effects*) to compute the POD curve for repeatedly measured experimental and simulated DI datasets derived from chapter four. Before applying these methods,

a linearity check has been introduced to identify the linear plot based on the coefficient of determination (R^2) value. *Length-at-detection* POD computation method is fast and simple once the underlying distribution is known to us. At the same time, the *random effects* model is a more generalized form of the conventional signal response method defined in NDT POD computation. Bayesian analysis of model parameter estimation in *random effects* helps to compare the uncertainty distributions of model parameters obtained from both experimental and simulated datasets. It is observed that the simulated POD $x_{90|95}$ values are slightly conservative compared to the experimental POD values due to more significant variabilities and the larger number of units considered in the model-assisted approach. Both *length-at-detection* and *random effects* methods provide roughly similar values, but the *random effects* method is a bit more conservative due to considering all repeated measurements in the analysis. In addition, a sample size calculation has also been presented to estimate the required $x_{90|95}$ value for a particular SHM application. This demonstrates the potential of the simulation tool to estimate the number of samples required for SHM application before performing experimental studies.

With these four chapters of this thesis, we conclude that the MAPOD approach for guided waves SHM is reliable and can be used for similar use cases in the future, provided that a careful study of the variabilities is performed as well as a validation of the simulation tool in the whole range of these variabilities.

6.2 Perspectives

This thesis has led to extensive work on a simplified aluminum plate-like structure, enabling model assisted POD studies. However, much work is needed in the future on POD studies for SHM, especially on real use cases. This thesis observed that the model assisted POD approach is reliable through the use of very large datasets for POD calculations obtained with minimal effort thanks to the use of a simulation tool. Therefore, the same model assisted POD methodology for computing the POD curve of GWs based SHM can be extended to other structures and materials, such as composites, with different known and unknown locations of damage types. In practice, there may be some future work to extend each of the methodological steps of the model assisted POD computation, which are explained below:

Transducer modeling in simulation tool: Transducer modeling is challenging, especially for a circular piezoelectric transducer. This thesis proposed a hybrid actuator model, compatible with the transient spectral finite element scheme developed at CEA, that relies on the pre-computation of bi-directional stresses from COMSOL for each new configuration. Indeed, no analytical formulation of stress computation for the circular piezoelectric transducer is available due to no closed-form equation solution. Therefore, some data-driven approaches, such as meta-model techniques, could be used to address this problem and provide a self-sufficient algorithm that does not require to use of an external simulation code. In addition, the proposed model could be extended to anisotropic materials/structures by computing directional depended stresses from COMSOL.

Variabilities in simulation and experimental POD studies: The demonstration of MAPOD methodology in this thesis has been performed in a rather controlled (lab-

oratory) environment. It would be interesting to consider more realistic/real use cases that include other or more severe sources of variabilities (larger temperature ranges, crack orientation and complex shape, variable structural loads...). Using this methodology on more complex structures, for example, composite plates requires careful and essential efforts to validate the simulation tools. For example, composite materials exhibit larger inter specimen material properties variations and attenuation of guided waves, this must be appropriately captured through experimental characterization campaigns, and simulation must be validated on the full range of expected configurations. These study and validations must be repeated for each source of variability, as in every POD analysis, and is use case dependent. A methodological question then still remains open and would be worth studying: how to take into account the confidence bound of the simulation (i.e., the inevitable discrepancy between simulation and experiment, neglected in this thesis) into MAPOD? Finally, an important phenomenon and source of variability that has not been considered in this study is the aging of the elements that compose the SHM system (such as sensors) and its consequences on the global performance of the SHM system. This difficult topic will require a specific analysis and will be a major step toward improving the confidence of guided waves based SHM.

Damage identification, quantification, and POD computation methods: There is a more prominent use of the machine learning approach found in the literature for damage identification and quantification in guided waves based SHM. From that perspective, it is natural to consider applying the methodology developed in this thesis to quantify the performance of guided waves based SHM systems that use machine learning to detect defects. However, some specificities of machine learning algorithms, primarily due to their non-explainable (black-box) characteristics, might require some adapted performance demonstration approaches. For example, the sensitivity of machine learning algorithms to the database used for training is a recognized difficulty [170]. How to update this database for continuously learning systems while claiming the performances based on an initial POD estimation is, for example, an open and difficult question. More generally, POD is the golden tool to compare analysis processes: POD with/without temperature compensation, for one data processing or another... MAPOD has the potential to easily and rapidly answer the question of the most efficient analysis process for a given configuration. MAPOD of guided waves based SHM systems based on imaging analysis, such as tomography algorithms, also has potential for further investigations. It would require a non-trivial extension of the current methodology based on the recent concepts of the probability of location (POL) [171] and POD map studies [108]. Finally, yet importantly, very few studies have been performed so far on the probability of false alarms (and consequently, receiving operating characteristics) of guided waves based SHM systems. This is a crucial research topic to fully characterize the performances of the monitoring system, closely linked to the definition of detection threshold and analysis processes described just above, which would certainly be of great interest to the final users.

CHAPTER 7

Appendix: Probability of detection

Additional figures of chapter 5

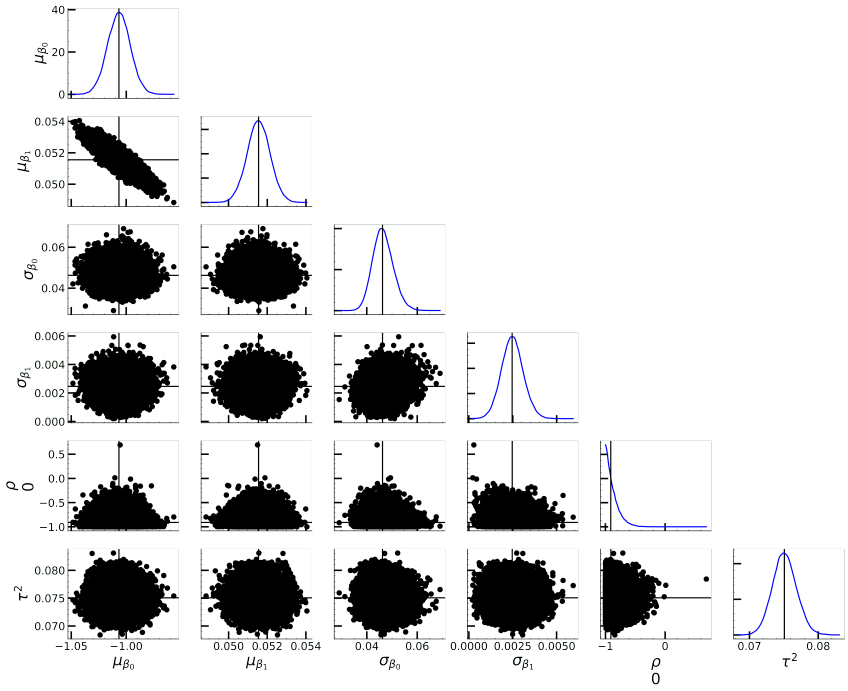

Figure 7.1: A matrix scatter plot of draws from joint posterior distribution of model parameters for simulated DI datasets.

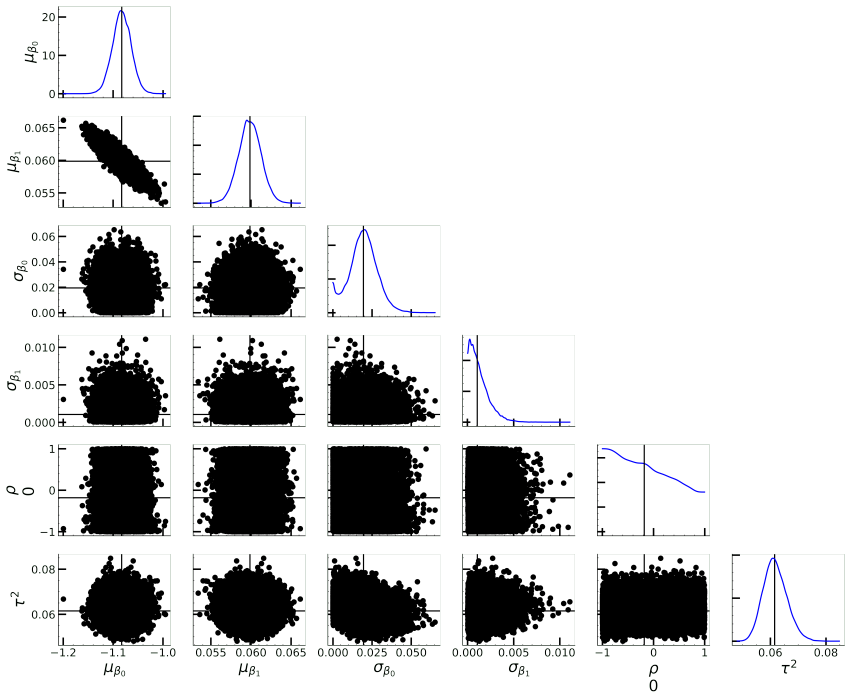

Figure 7.2: A matrix scatter plot of draws from joint posterior distribution of model parameters for experimental DI datasets.

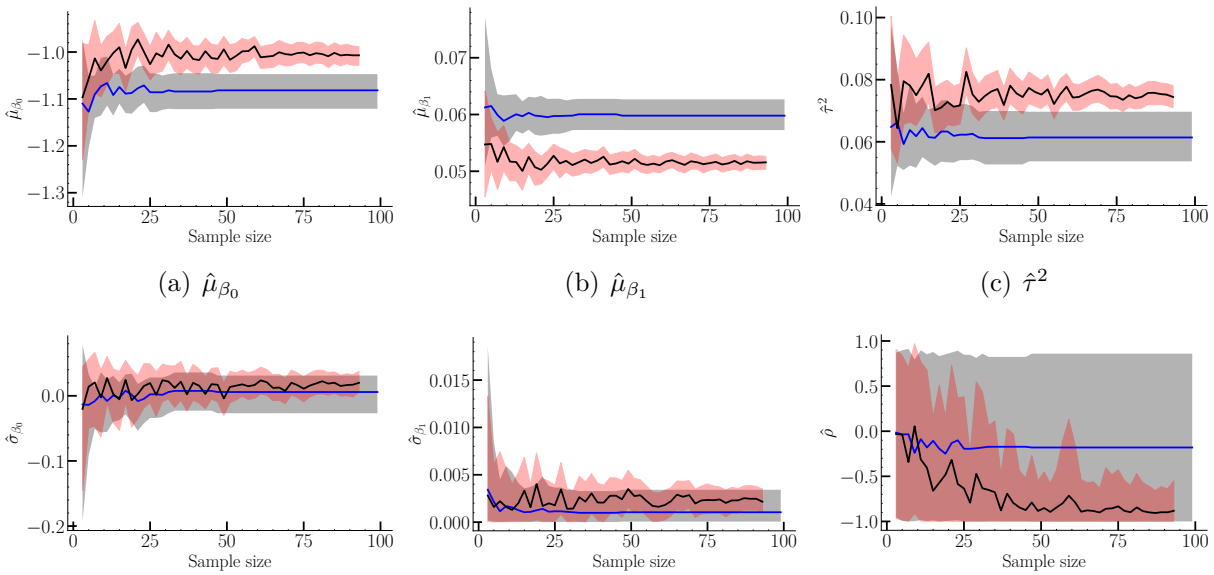

(a) $\hat{\mu}_{\beta_0}$ (b) $\hat{\mu}_{\beta_1}$ (c) $\hat{\tau}^2$

(d) $\hat{\sigma}_{\beta_0}$ (e) $\hat{\sigma}_{\beta_1}$ (f) $\hat{\rho}$

Figure 7.3: The median of marginal posterior distribution of six parameters with sample size for experimental dataset (blue line) and simulated dataset (black line) with an uncertainty of 95% HDI in light red and black for the simulated and experimental datasets, respectively.

CHAPTER 8

Synthèse en français

La surveillance de l'état des structures (SHM) consiste à intégrer des capteurs dans une structure afin d'évaluer son intégrité sans interrompre son fonctionnement. Les ondes élastiques guidées sont reconnues comme une technologie prometteuse pour le SHM dans les domaines de l'aérospatiale, du pétrole et du gaz, et des industries nucléaires. En effet, les ondes guidées dans des structures en forme de plaques ont des caractéristiques de propagation à longue distance et de faible atténuation, ce qui limite considérablement le nombre de capteurs nécessaires pour surveiller une zone critique donnée ou un composant. Des transducteurs piézoélectriques minces, légers et peu coûteux, ont été utilisés dans la majorité des systèmes basés sur les ondes guidées (GW). Ces transducteurs sont fixés à ou dans la structure et génèrent divers modes d'ondes élastiques, généralement des modes de Lamb antisymétriques et symétriques de faible ordre dans des structures isotropes en forme de plaque ou des ondes similaires dans des spécimens anisotropes en forme de plaque. Les modes d'onde sont soit réfléchis, soit diffusés, soit convertis en d'autres modes d'onde par les perturbations géométriques du guide d'onde et les défauts structurels potentiels. Des techniques spécifiques de traitement du signal sont ensuite utilisées pour extraire l'état actuel de la structure par l'analyse des signaux capturés par les transducteurs.

Bien que le domaine du SHM basé sur les GWs ait reçu une attention considérable de la part de la communauté des chercheurs, très peu de techniques d'inspection SHM basées sur les GWs ont encore trouvé des applications industrielles, notamment en raison de la difficulté à démontrer la performance du système de surveillance. Pour les techniques non destructives (CND), la performance est caractérisée par la courbe de probabilité de détection (POD). Largement acceptée par l'industrie, la courbe POD est estimée par de multiples expériences indépendantes sur des structures inspectées données. Alors que pour les essais non destructifs, les expériences indépendantes sont créées en multipliant les étapes d'acquisition par différents opérateurs sur un nombre limité d'échantillons, alors que dans la méthode GW-SHM, les transducteurs sont fixés à la structure ; par conséquent, la création d'acquisitions indépendantes est coûteuse et fastidieuse. Pour surmonter ce problème, une démonstration de performance basée sur la simulation, telle que la probabilité de détection assistée par modèle (MAPOD), est une solution intéressante.

Cependant, MAPOD nécessite un outil validé et efficace capable de générer un nombre statistiquement significatif de simulations à un coût de calcul raisonnable.

Actuellement, de nombreux outils de simulation et de modélisation sont disponibles pour le GW-SHM, et la plupart d'entre eux sont basés sur la modélisation par éléments finis (FE). Certains logiciels FE offrent des modules multiphysiques pour modéliser le couplage transducteur-structure, qui est souvent une partie critique et difficile des simulations. Cependant, les structures typiques sont longues de plusieurs dizaines ou centaines de longueurs d'onde, avec une exigence de 10 à 20 degrés de liberté par plus petite longueur d'onde, ce qui rend les calculs très coûteux. Ceci est généralement prohibitif pour les calculs MAPOD où des centaines ou des milliers de simulations doivent être exécutées.

Pour surmonter ce problème de coût de calcul, la méthode des éléments finis spectraux (SFE) a été introduite et, grâce à une réduction du nombre de degrés de liberté et un calcul plus efficace à chaque pas de temps, elle réduit le coût de calcul global. Récemment, la méthode SFE en régime transitoire a été intégrée au logiciel CIVA afin de réduire le coût de calcul, alors que les logiciels FE conventionnels fournissent des résultats similaires en plusieurs jours à environ une semaine de calcul. Par conséquent, le logiciel CIVA a un excellent potentiel pour produire de nombreuses simulations lors des calculs MAPOD.

Pour obtenir de telles performances de calcul, la plateforme CIVA s'appuie sur deux approches : les éléments finis spectraux d'ordre élevé permettant une procédure de maillage paramétrique basée sur des macro-éléments, et le modèle approximatif de transducteur piézoélectrique appelé Pin Force (PF) est utilisé comme charge de surface pour l'excitation GW.

Le modèle PF consiste en une traction de contrainte constante appliquée dans la direction radiale à la périphérie du transducteur piézoélectrique circulaire. Il convient de noter qu'en raison de l'hypothèse d'un couplage adhésif idéal entre le transducteur piézoélectrique et la structure hôte, et de l'hypothèse d'un transducteur mince, l'hypothèse d'une traction de contrainte radiale constante est limitée à la fréquence d'excitation. La fréquence d'excitation pour le modèle PF est validée bien en dessous de la première fréquence de résonance électromécanique du transducteur piézoélectrique en raison de la non prise en compte de la dynamique et de la contrainte normale du transducteur. Pour surmonter cette limitation, un nouveau modèle est nécessaire qui n'affecte pas le temps de calcul et les performances.

Ici, dans le chapitre 3, nous avons proposé un modèle d'actionneur hybride (HAM) pour la modélisation du transducteur piézoélectrique qui inclut deux directions de tractions, radiale et normale, ainsi que la dynamique du transducteur piézoélectrique. Pour reproduire le comportement en fonction de la fréquence, une épaisseur d'adhésif finie est introduite. Au cours de l'étape de pré-calcul, la dynamique du transducteur piézoélectrique dans les deux directions est calculée par le biais de la FE (COMSOL Multiphysics), et l'effet de l'épaisseur finie de l'adhésif est estimé sur la base du rapport d'admittance du transducteur piézoélectrique collé et non collé. Une étude paramétrique est réalisée pour quantifier la validité du modèle d'actionneur hybride en termes de fréquence d'excitation. On observe que le modèle d'actionneur hybride proposé modélise également avec précision le signal de transduction au-dessus de la première fréquence de résonance électromécanique d'un transducteur piézoélectrique.

Ensuite, dans le chapitre 4, nous avons présenté une méthodologie complète pour la

démonstration des performances du SHM basé sur les GWs via une approche assistée par modèle. Des études expérimentales et de simulation ont été réalisées sur le cas d'utilisation de fissures croissantes à partir d'un trou sur une plaque d'aluminium. Des mesures répétées ont été obtenues expérimentalement à partir de 12 plaques d'aluminium identiques et indépendantes avec des fissures jusqu'à 30 mm de long pour obtenir des réponses stochastiques dans le domaine temporel. Les limites des variabilités expérimentales ont également été enregistrées pour reproduire la variabilité de la réponse de sortie de l'outil de simulation. Les ensembles de signaux dans le domaine temporel, expérimentaux et assistés par modèle, sont mis en correspondance avec l'indice de dommage et comparés pour caractériser la validité d'une approche assistée par modèle pour la génération de données. On constate que les ensembles de données expérimentales et simulées concordent très bien dans les points de dispersion du domaine temporel et de l'indice de dommages (DI). En outre, les points de dispersion de l'indice de dommages présentent une sensibilité plus élevée à la longueur de la fissure dans les trajets de capteurs directs et diagonaux que dans les trajets de capteurs indirects. Cependant, dans les trajectoires de capteurs indirects, l'ensemble de données DI expérimentales est légèrement décalé par rapport à l'ensemble de données simulées parce que la fissure n'est pas droite pendant l'élongation dans l'expérience. Certaines tendances non linéaires de l'ID sont également marquées le long de la longueur de la fissure, ce qui est expliqué par la longueur de fissure normalisée par la longueur d'onde avec l'étude de la variation de fréquence et divisée en quatre régions basées sur l'interaction de longueur d'onde des modes d'onde. On observe ainsi que la DI est plus influencée à des fréquences plus élevées pour les modes S_0 et plus basses pour les modes A_0, respectivement.

Dans le dernier chapitre 5, nous avons présenté deux méthodes statistiques récemment proposées (longueur à la détection et effets aléatoires) pour calculer la courbe POD pour des ensembles de données DI expérimentales et simulées mesurées à plusieurs reprises et dérivées du chapitre 4. Avant d'appliquer ces méthodes, un contrôle de linéarité a été introduit pour identifier le tracé linéaire sur la base de la valeur du coefficient de détermination (R^2). La méthode de calcul POD de *Length-at-detection* est rapide et simple une fois que l'on connaît la distribution sous-jacente. En même temps, le modèle *random effects* est une forme plus généralisée de la méthode conventionnelle de réponse au signal définie dans le calcul POD des CND. L'analyse bayésienne de l'estimation des paramètres du modèle dans le modèle *random effects* permet de comparer les distributions d'incertitude des paramètres du modèle obtenues à partir des ensembles de données expérimentales et simulées. On observe que les valeurs POD $x_{90|95}$ simulées sont légèrement conservatrices par rapport aux valeurs POD expérimentales en raison de variabilités plus importantes et du plus grand nombre d'unités considérées dans l'approche assistée par modèle. Les méthodes *Length-at-detection* et *random effects* fournissent des valeurs à peu près similaires, mais la méthode *random effects* est un peu plus conservatrice car elle prend en compte toutes les mesures répétées dans l'analyse. En outre, un calcul de la taille de l'échantillon a également été présenté pour estimer la valeur $x_{90|95}$ requise pour une application SHM particulière. Cela démontre le potentiel de l'outil de simulation pour estimer le nombre d'échantillons requis pour une application SHM avant de réaliser des études expérimentales.

Avec ces quatre chapitres de cette thèse, nous concluons que l'approche MAPOD pour

le SHM des ondes guidées est fiable et peut être utilisée pour des cas d'utilisation similaires dans le futur, à condition qu'une étude minutieuse des variabilités soit effectuée ainsi qu'une validation de l'outil de simulation dans toute la gamme de ces variabilités.

Cette thèse a conduit à un travail approfondi sur une structure simplifiée de type plaque d'aluminium, permettant des études POD assistées par modèle. Cependant, beaucoup de travail est nécessaire à l'avenir sur les études POD pour SHM, en particulier sur des cas d'utilisation réels. Cette thèse a observé que l'approche POD assistée par modèle est fiable grâce à l'utilisation de très grands ensembles de données pour les calculs POD obtenus avec un effort minimal grâce à l'utilisation d'un outil de simulation. Par conséquent, la même méthodologie POD assistée par modèle pour le calcul de la courbe POD du SHM basé sur les GWs peut être étendue à d'autres structures et matériaux, tels que les composites, avec différents emplacements connus et inconnus des types de dommages.

Bibliography

[1] P.A. Withey. Fatigue failure of the De Havilland Comet i. *Engineering Failure Analysis*, 4(2): 147–154, 1997-06. doi: 10.1016/s1350-6307(97)00005-8. → p. 1

[2] Stefano Invernizzi, Francesco Montagnoli, and Alberto Carpinteri. Fatigue assessment of the collapsed XXth century cable-stayed Polcevera Bridge in Genoa. *Procedia Structural Integrity*, 18: 237–244, 2019. doi: 10.1016/j.prostr.2019.08.159. → p. 1

[3] HLNT Dossier. Gas pipeline explosion at Ghislenghien, Belgium. *Available at: www. iab-atex. nl (Data accessed: July 1, 2015)*, 2005. → p. 1

[4] Ting Dong and Nam H Kim. Cost-effectiveness of structural health monitoring in fuselage maintenance of the civil aviation industry. *Aerospace*, 5(3):87, 2018. → p. 2

[5] S. Gholizadeh. A review of non-destructive testing methods of composite materials. *Procedia Structural Integrity*, 1:50–57, 2016. doi: 10.1016/j.prostr.2016.02.008. → p. 2

[6] Charles J Hellier. *Handbook of nondestructive evaluation*. McGraw-Hill Education, 2013. → p. 2

[7] V Giurgiutiu, A Zagrai, J Bao, J Redmond, D Roach, and Kirk Rackow. Active sensors for health monitoring of aging aerospace. *Int. J. Comadem*, 6(1):3–21, 2003. → p. 2

[8] Xinlin Qing, Wenzhuo Li, Yishou Wang, and Hu Sun. Piezoelectric transducer-based structural health monitoring for aircraft applications. *Sensors*, 19(3):545, 2019-01. doi: 10.3390/s19030545. → p. 3

[9] Victor Giurgiutiu. *Structural health monitoring of aerospace composites*. Academic Press, 2015. → p. 3

[10] Victor Giurgiutiu. *Structural health monitoring: with piezoelectric wafer active sensors*. Elsevier, 2007. → p. 3, 5, 7, 9, 12, 20, 29, 37, 65

[11] Charles R Farrar and Keith Worden. An introduction to structural health monitoring. *Philosophical Transactions of the Royal Society A: Mathematical, Physical and Engineering Sciences*, 365(1851): 303–315, 2006-12. doi: 10.1098/rsta.2006.1928. → p. 3

[12] W. J. Staszewski, C. Boller, and G. R. Tomlinson. *Health Monitoring of Aerospace Structures*. Wiley Online Library, 2003-12. doi: 10.1002/0470092866. → p. 3

[13] Saqlain Abbas, Fucai Li, and Jianxi Qiu. A review on SHM techniques and current challenges for characteristic investigation of damage in composite material components of aviation industry. *Materials Performance and Characterization*, 7(1):20170167, 2018-06. doi: 10.1520/mpc20170167. → p. 3, 9

[14] A Rytter. *Vibration based inspection of civil engineering structures [Ph.D. thesis]*. PhD thesis, Aalborg University, 1993. → p. 3

[15] Opukuro David-West, Daerefa Amafabia, George Haritos, and Diogo Montalvao. A review of structural health monitoring techniques as applied to composite structures. *Structural Durability & Health Monitoring*, 2017. → p. 3

[16] Vahid Reza Gharehbaghi, Ehsan Noroozinejad Farsangi, Mohammad Noori, TY Yang, Shaofan Li, Andy Nguyen, Christian Málaga-Chuquitaype, Paolo Gardoni, and Seyedali Mirjalili. A critical review on structural health monitoring: definitions, methods, and perspectives. *Archives of Computational Methods in Engineering*, pages 1–27, 2021. → p. 3

[17] Francesc Pozo, Diego A. Tibaduiza, and Yolanda Vidal. Sensors for structural health monitoring and condition monitoring. *Sensors*, 21(5):1558, 2021-02. doi: 10.3390/s21051558. → p. 3

[18] Dennis Patrick Roach and Stephen Neidigk. Does the maturity of structural health monitoring technology match user readiness?. Technical report, Sandia National Lab.(SNL-NM), Albuquerque, NM (United States), 2011. → p. 4

[19] Alfredo Güemes. SHM technologies and applications in aircraft structures. In *Proceedings of the 5th International Symposium on NDT in Aerospace, Singapore*, volume 1315, 2013. → p. 4

[20] Paul Swindell, Jon Doyle, and Dennis Roach. Integration of structural health monitoring solutions onto commercial aircraft via the Federal Aviation Administration structural health monitoring research program. *AIP Conference Proceedings*, 1806(1):070001, 2017. doi: 10.1063/1.4974616. → p. 4, 60

[21] Jonathan J Scholey, Paul D Wilcox, CK Lee, Michael I Friswell, and MR Wisnom. Acoustic emission in wide composite specimens. In *Advanced Materials Research*, volume 13, pages 325–332. Trans Tech Publ, 2006. → p. 4

[22] Richard D Finlayson, Mark Friesel, Mark Carlos, P Cole, and JC Lenain. Health monitoring of aerospace structures with acoustic emission and acousto-ultrasonics. *Insight*, 2001. → p. 5

[23] Arnaud Deraemaeker and Keith Worden. *New trends in vibration based structural health monitoring*, volume 520. Springer Science & Business Media, 2012. → p. 5

[24] Wei Fan and Pizhong Qiao. Vibration-based damage identification methods: a review and comparative study. *Structural health monitoring*, 10(1):83–111, 2011. → p. 5

[25] Raimund Rolfes, Stephan Zerbst, G Haake, Jonannes Reetz, and Jerome P Lynch. Integral SHM for offshore wind turbines using smart wireless sensors. In *Proceedings of the 6th International Workshop on Structural Health Monitoring*, volume 200, pages 11–13. Citeseer, 2007. → p. 5

[26] Gayan C Kahandawa, Jayantha Epaarachchi, Hao Wang, and KT Lau. Use of FBG sensors for SHM in aerospace structures. *Photonic Sensors*, 2(3):203–214, 2012. → p. 5

[27] Victor Giurgiutiu and Andrei Zagrai. Damage detection in simulated aging-aircraft panels using the electro-mechanical impedance technique. In *ASME International Mechanical Engineering Congress and Exposition*, volume 19135, pages 349–358. American Society of Mechanical Engineers, 2000. → p. 5

[28] Suresh Bhalla and Chee-Kiong Soh. Electro-mechanical impedance technique for structural health monitoring and non-destructive evaluation. In *National workshop on structural health monitoring, non-destructive evaluation and retrofitting of structures. Indian Institute of Technology Delhi*, 2008. → p. 5

[29] Peter Cawley. Structural health monitoring: Closing the gap between research and industrial deployment. *Structural Health Monitoring*, 17(5):1225–1244, 2018. doi: 10.1177/1475921717750047. → p. 5, 9, 10

[30] Srinivasan Gopalakrishnan. *Wave propagation in materials and structures*. CRC Press, 2016. doi: 10.1201/9781315372099. → p. 5

[31] A. Raghavan and C. E. S. Cesnik. Review of guided-wave structural health monitoring. *The Shock and Vibration Digest*, 39(2):91–114, 2007-03. doi: 10.1177/0583102406075428. → p. 5, 7, 9

[32] A. Tatarinov, Evgeny N. Barkanov, E. Davydov, and M. Mihovski. *T- and L-Types of Long-Range Guided Waves for Defect Detection*, pages 15–29. Springer International Publishing, Cham, 2018.

ISBN 978-3-319-56579-8. doi: 10.1007/978-3-319-56579-8_2. URL https://doi.org/10.1007/978-3-319-56579-8_2. → p. 5

[33] Norbert GH Meyendorf, Peter B Nagy, and Stanislav I Rokhlin. *Nondestructive materials characterization: With applications to aerospace materials*, volume 67. Springer Science & Business Media, 2013. → p. 5

[34] Joseph L Rose. *Ultrasonic waves in solid media*. Cambridge university press, 2004. doi: https://doi.org/10.1017/CBO9781107273610. → p. 5, 6

[35] Hossein Towsyfyan, Ander Biguri, Richard Boardman, and Thomas Blumensath. Successes and challenges in non-destructive testing of aircraft composite structures. *Chinese Journal of Aeronautics*, 33(3):771–791, 2020-03. doi: 10.1016/j.cja.2019.09.017. → p. 6

[36] Joseph L. Rose and Luis E. Soley. Ultrasonic guided waves for anomaly detection in aircraft components, September 2000. ISSN 0025-5327. → p. 6

[37] Karl F Graff. *Wave motion in elastic solids*. Courier Corporation, 2012. → p. 6

[38] W Zhu, JL Rose, JN Barshinger, and VS Agarwala. Ultrasonic guided wave NDT for hidden corrosion detection. *Journal of Research in Nondestructive Evaluation*, 10(4):205–225, 1998. → p. 6

[39] Paul D Wilcox, MJS Lowe, and P Cawley. Mode and transducer selection for long range Lamb wave inspection. *Journal of intelligent material systems and structures*, 12(8):553–565, 2001. → p. 6

[40] Bruce Maxfield and Zhiyong Wang. Electromagnetic acoustic transducers for nondestructive evaluation. *ASM Handbook*, 17:214–237, 2018. → p. 6

[41] Donald J Leo. *Engineering analysis of smart material systems*. John Wiley & Sons, 2007. → p. 7

[42] B Lin and V Giurgiutiu. Modeling and testing of PZT and PVDF piezoelectric wafer active sensors. *Smart Materials and Structures*, 15(4):1085–1093, 2006-07. doi: 10.1088/0964-1726/15/4/022. → p. 7

[43] Stefan Hurlebaus and Lothar Gaul. SMART layer for damage diagnostics. *Journal of Intelligent Material Systems and Structures*, 15(9-10):729–736, 2004-09. doi: 10.1177/1045389x04041937. → p. 7

[44] R.S.C. Monkhouse, P.D. Wilcox, and P. Cawley. Flexible interdigital PVDF transducers for the generation of Lamb waves in structures. *Ultrasonics*, 35(7):489–498, 1997-11. doi: 10.1016/s0041-624x(97)00070-x. → p. 7

[45] Mira Mitra and S Gopalakrishnan. Guided wave based structural health monitoring: A review. *Smart Materials and Structures*, 25(5):053001, 2016. doi: 10.1088/0964-1726/25/5/053001. → p. 7, 8, 9

[46] leong Zhaoyuan, CHAN Louise, Nicholas WALTERS, James CLARKE, William HOLMES, and Simon HAYES. Structural health monitoring using magnetostrictive sensors. In *2018 IEEE International Magnetics Conference (INTERMAG)*, pages 1–5. IEEE, 2018. → p. 7

[47] Chenxi Xie, Tianhao Liu, Cuixiang Pei, and Zhenmao Chen. A flexible thin-film magnetostrictive patch guided-wave transducer for structural health monitoring. *IEEE Sensors Journal*, 2022. → p. 7

[48] W J Staszewski, B C Lee, and R Traynor. Fatigue crack detection in metallic structures with Lamb waves and 3D laser vibrometry. *Measurement Science and Technology*, 18(3):727–739, 2007-01. doi: 10.1088/0957-0233/18/3/024. → p. 7

[49] Joseph L. Rose. A baseline and vision of ultrasonic guided wave inspection potential. *Journal of Pressure Vessel Technology*, 124(3):273–282, 2002-07. doi: 10.1115/1.1491272. → p. 7

[50] D. N. Alleyne, B. Pavlakovic, M. J. S. Lowe, and P. Cawley. Rapid, long range inspection of chemical plant pipework using guided waves. *AIP Conference Proceedings*, 557(1):180–187, 2001.

doi: 10.1063/1.1373757. → p. 7

[51] Ryan P Dalton, Peter Cawley, and Michael JS Lowe. The potential of guided waves for monitoring large areas of metallic aircraft fuselage structure. *Journal of Nondestructive Evaluation*, 20(1): 29–46, 2001. → p. 7

[52] Peter Cawley and David Alleyne. The use of Lamb waves for the long range inspection of large structures. *Ultrasonics*, 34(2-5):287–290, 1996-06. doi: 10.1016/0041-624x(96)00024-8. → p. 7

[53] Zhongqing Su and Lin Ye. *Identification of damage using Lamb waves: from fundamentals to applications*, volume 48. Springer Science & Business Media, 2009. → p. 7, 9

[54] Victor Giurgiutiu, Andrei Zagrai, and Jing Jing Bao. Piezoelectric wafer embedded active sensors for aging aircraft structural health monitoring. *Structural Health Monitoring*, 1(1):41–61, 2002. → p. 7

[55] Roberto Miorelli, Clément Fisher, Andrii Kulakovskyi, Bastien Chapuis, Olivier Mesnil, and Oscar D'Almeida. Defect sizing in guided wave imaging structural health monitoring using convolutional neural networks. *NDT International*, 122:102480, 2021-09. doi: 10.1016/j.ndteint.2021.102480. → p. 7, 9

[56] Christian Boller, Fu-Kuo Chang, and Yozo Fujino, editors. *Encyclopedia of Structural Health Monitoring*. John Wiley & Sons, Ltd, 2009-01. doi: 10.1002/9780470061626. → p. 8

[57] Rahim Gorgin, Ying Luo, and Zhanjun Wu. Environmental and operational conditions effects on Lamb wave based structural health monitoring systems: A review. *Ultrasonics*, 105:106114, jul 2020. doi: 10.1016/j.ultras.2020.106114. → p. 8, 9, 67

[58] Ajay Raghavan and Carlos ES Cesnik. Effects of elevated temperature on guided-wave structural health monitoring. *Journal of Intelligent Material Systems and Structures*, 19(12):1383–1398, 2008. → p. 8

[59] W. J. Staszewski and K. Worden. Signal processing for damage detection. In *Health Monitoring of Aerospace Structures*, pages 163–206. John Wiley & Sons, Ltd, 2003. doi: 10.1002/0470092866.ch5. → p. 8

[60] T Clarke and P Cawley. Enhancing the defect localization capability of a guided wave SHM system applied to a complex structure. *Structural Health Monitoring*, 10(3):247–259, 2011. → p. 8

[61] Piervincenzo Rizzo and Francesco Lanza di Scalea. Feature extraction for defect detection in strands by guided ultrasonic waves. *Structural Health Monitoring*, 5(3):297–308, 2006. → p. 9

[62] Daniel C Betz, Wieslaw J Staszewski, Graham Thursby, and Brian Culshaw. Structural damage identification using multifunctional Bragg grating sensors: II. Damage detection results and analysis. *Smart Materials and Structures*, 15(5):1313–1322, 2006-08. doi: 10.1088/0964-1726/15/5/021. → p. 9

[63] Afshin Sattarifar and Tamara Nestorović. Frequency-bounded delay and sum: A modified damage detection method in thin-walled plates. *PAMM*, 19(1):e201900368, 2019. → p. 9

[64] Lucas S Barreto, Marcela R Machado, Juliana C Santos, Braion B de Moura, and Leila Khalij. Damage indices evaluation for one-dimensional guided wave-based structural health monitoring. *Latin American Journal of Solids and Structures*, 18, 2021. → p. 9, 71

[65] Jian Cai, Lihua Shi, Shenfang Yuan, and Zhixue Shao. High spatial resolution imaging for structural health monitoring based on virtual time reversal. *Smart Materials and Structures*, 20(5):055018, 2011-04. doi: 10.1088/0964-1726/20/5/055018. → p. 9

[66] N Quaegebeur, P Masson, D Langlois-Demers, and P Micheau. Dispersion-based imaging for structural health monitoring using sparse and compact arrays. *Smart Materials and Structures*, 20(2): 025005, 2011-01. doi: 10.1088/0964-1726/20/2/025005. → p. 9

[67] James S Hall, Paul Fromme, and Jennifer E Michaels. Guided wave damage characterization via minimum variance imaging with a distributed array of ultrasonic sensors. *Journal of Nondestructive Evaluation*, 33(3):299–308, 2014. → p. 9

[68] Chao Zhou, Zhongqing Su, and Li Cheng. Quantitative evaluation of orientation-specific damage using elastic waves and probability-based diagnostic imaging. *Mechanical Systems and Signal Processing*, 25(6):2135–2156, 2011-08. doi: 10.1016/j.ymssp.2011.02.001. → p. 9

[69] Andrii Kulakovskyi, Olivier Mesnil, Bastien Chapuis, Oscar d'Almeida, and Alain Lhémery. Statistical analysis of guided wave imaging algorithms performance illustrated by a simple structural health monitoring configuration. *Journal of Nondestructive Evaluation, Diagnostics and Prognostics of Engineering Systems*, 4(3), 2021-02. doi: 10.1115/1.4049571. → p. 9, 12

[70] Anthony J Croxford, Paul D Wilcox, George Konstantinidis, and Bruce W Drinkwater. Strategies for overcoming the effect of temperature on guided wave structural health monitoring. In *Health Monitoring of Structural and Biological Systems 2007*, volume 6532, pages 590–599. SPIE, 2007. → p. 9

[71] G Konstantinidis, B W Drinkwater, and P D Wilcox. The temperature stability of guided wave structural health monitoring systems. *Smart Materials and Structures*, 15(4):967–976, 2006-06. doi: 10.1088/0964-1726/15/4/010. → p. 9

[72] Anthony J. Croxford, Jochen Moll, Paul D. Wilcox, and Jennifer E. Michaels. Efficient temperature compensation strategies for guided wave structural health monitoring. *Ultrasonics*, 50(4-5):517–528, 2010-04. doi: 10.1016/j.ultras.2009.11.002. → p. 9

[73] Stefano Mariani, Sebastian Heinlein, and Peter Cawley. Location specific temperature compensation of guided wave signals in structural health monitoring. *IEEE Transactions on Ultrasonics, Ferroelectrics, and Frequency Control*, 67(1):146–157, 2020. doi: 10.1109/TUFFC.2019.2940451. → p. 9

[74] Wenzhong Qu, Li Xiao, Yanguo Zhou, and Daniel J Inman. Lamb wave damage detection using time reversal DORT method. *Smart Materials and Structures*, 22(4):045014, 2013-03. doi: 10.1088/0964-1726/22/4/045014. → p. 9

[75] Hyung Jin Lim, Hoon Sohn, Chul Min Yeum, and Ji Min Kim. Reference-free damage detection, localization, and quantification in composites. *The Journal of the Acoustical Society of America*, 133(6):3838–3845, 2013-06. doi: 10.1121/1.4802744. → p. 9

[76] Tom Druet, Jean-Loup Tastet, Bastien Chapuis, and Emmanuel Moulin. Autocalibration method for guided wave tomography with undersampled data. *Wave Motion*, 89:265–283, 2019-06. doi: 10.1016/j.wavemoti.2019.04.002. → p. 9, 12

[77] C Fendzi, M Rébillat, N Mechbal, M Guskov, and G Coffignal. A data-driven temperature compensation approach for structural health monitoring using Lamb waves. *Structural Health Monitoring*, 15(5):525–540, 2016-08. doi: 10.1177/1475921716650997. → p. 9

[78] Mahindra Rautela and S. Gopalakrishnan. Ultrasonic guided wave based structural damage detection and localization using model assisted convolutional and recurrent neural networks. *Expert Systems with Applications*, 167:114189, 2021-04. doi: 10.1016/j.eswa.2020.114189. → p. 9

[79] Mahindra Rautela, J. Senthilnath, Jochen Moll, and Srinivasan Gopalakrishnan. Combined two-level damage identification strategy using ultrasonic guided waves and physical knowledge assisted machine learning. *Ultrasonics*, 115:106451, 2021-08. doi: 10.1016/j.ultras.2021.106451. → p. 9, 12

[80] Shruti Sawant, Sheetal Patil, Jeslin Thalapil, Sauvik Banerjee, and Siddharth Tallur. Temperature variation compensated damage classification and localisation in ultrasonic guided wave shm using self-learnt features and gaussian mixture models. *Smart Materials and Structures*, 31(5):055008, 2022. → p. 9

[81] Afshin Sattarifar and Tamara Nestorović. Emergence of machine learning techniques in ultrasonic guided wave-based structural health monitoring. *International Journal of Prognostics and Health Management*, 13(1), 2022-05. doi: 10.36001/ijphm.2022.v13i1.3107. → p. 9

[82] Francesco Falcetelli, Nan Yue, Raffaella Di Sante, and Dimitrios Zarouchas. Probability of detection, localization, and sizing: The evolution of reliability metrics in structural health monitoring. *Structural Health Monitoring*, page 147592172110607, 2021-12. doi: 10.1177/14759217211060780. → p. 9, 10, 13

[83] Zhongqing Su, Lin Ye, and Ye Lu. Guided Lamb waves for identification of damage in composite structures: A review. *Journal of Sound and Vibration*, 295(3-5):753–780, 2006-08. doi: 10.1016/j.jsv.2006.01.020. → p. 9

[84] Hoon Sohn. Effects of environmental and operational variability on structural health monitoring. *Philosophical Transactions of the Royal Society A: Mathematical, Physical and Engineering Sciences*, 365(1851):539–560, 2007. doi: 10.1098/rsta.2006.1935. → p. 9

[85] Mahjoub El Mountassir, Slah Yaacoubi, and Fethi Dahmene. Reducing false alarms in guided waves structural health monitoring of pipelines: review synthesis and debate. *International Journal of Pressure Vessels and Piping*, 188:104210, 2020. → p. 9

[86] C Annis, Erland Bray, Herron Hardy, and PMS Hoppe. Nondestructive evaluation system reliability assessment. *United States Department of Defense, Wright-Patterson AFB, Handbook MIL-HDBK-1823A*, 2009. → p. 9, 12, 60, 80, 82, 95

[87] Mahjoub El Mountassir, Slah Yaacoubi, and Fethi Dahmene. Reducing false alarms in guided waves structural health monitoring of pipelines: Review synthesis and debate. *International Journal of Pressure Vessels and Piping*, 188:104210, 2020-12. doi: 10.1016/j.ijpvp.2020.104210. → p. 10

[88] AP Berens and PW Hovey. *Statistical methods for estimating crack detection probabilities*. ASTM International West Conshohocken, PA 19428-2959, 1983. → p. 10

[89] Fu-Kuo Chang, Johannes FC Markmiller, Jinkyu Yang, and Yujun Kim. Structural health monitoring. *System health management: with aerospace applications*, pages 419–428, 2011. → p. 10

[90] John C. Aldrin, Enrique A. Medina, Eric A. Lindgren, Charles F. Buynak, and Jeremy S. Knopp. Case studies for model-assisted probabilistic reliability assessment for structural health monitoring systems. *AIP Conference Proceedings*, 1335(1):1589–1596, 2011. doi: 10.1063/1.3592119. → p. 10

[91] Peter Cawley. A development strategy for structural health monitoring applications. *Journal of Nondestructive Evaluation, Diagnostics and Prognostics of Engineering Systems*, 4(4), 2021-08. doi: 10.1115/1.4051974. → p. 10

[92] John C. Aldrin, Enrique A. Medina, Eric A. Lindgren, Charles Buynak, Gary Steffes, and Mark Derriso. Model-assisted probabilistic reliability assessment for structural health monitoring systems. *AIP Conference Proceedings*, 1211(1):1965–1972, 2010. doi: 10.1063/1.3362348. → p. 10

[93] Dennis P Roach and Thomas M Rice. Wide area monitoring of aircraft structures using acousto-ultrasonic sensor networks. Technical report, Sandia National Lab.(SNL-NM), Albuquerque, NM (United States), 2016. → p. 10

[94] Anders Rosell and Gert Persson. Model based capability assessment of an automated eddy current inspection procedure on flat surfaces. *Research in Nondestructive Evaluation*, 24(3):154–176, 2013-07. doi: 10.1080/09349847.2013.779401. → p. 10

[95] R Bruce Thompson, Lisa J Brasche, Eric Lindgren, Paul Swindell, and William P Winfree. Recent advances in model-assisted probability of detection. In *4th European-American workshop on reliability of NDE*, 2009. → p. 10

[96] B. Azzabi Zouraq, H. K. Bui, A. Peterzol, G. Wasselynck, G. Berthiau, D. Trichet, and M. Taglione. A model-assisted probability of detection study on induction thermography technique. *IEEE Trans-*

actions on Magnetics, 55(6):1–4, 2019-06. doi: 10.1109/tmag.2019.2898733. → p. 10

[97] Bengisu Yilmaz, Damira Smagulova, and Elena Jasiuniene. Model-assisted reliability assessment for adhesive bonding quality evaluation with ultrasonic NDT. *NDT & E International*, 126:102596, 2022. → p. 10

[98] Ryan M Meyer, Susan L Crawford, John P Lareau, and Michael T Anderson. Review of literature for model assisted probability of detection. *Pacific Northwest National Lab.(PNNL), Richland, WA (United States)*, 2014. → p. 10

[99] Pierre Calmon, Bastien Chapuis, Frédéric Jenson, and Eric Sjerve. The use of simulation in POD curves estimation: An overview of the IIW best practices proposal. In *19th World conference on non-destructive testing, Munich, Germany*, 2016. → p. 10

[100] Carlos Correia and Grupo Endalloy CA-Caracas-Venezuela. The binomial approach for probability of detection. *e-Journal of Nondestructive Testing (NDT)*, 2015. URL www.ndt.net/?id=17498. → p. 10, 80

[101] Cara A.C. Leckey, Kevin R. Wheeler, Vasyl N. Hafiychuk, Halyna Hafiychuk, and Doğan A. Timuçin. Simulation of guided-wave ultrasound propagation in composite laminates: Benchmark comparisons of numerical codes and experiment. *Ultrasonics*, 84:187–200, 2018. doi: 10.1016/j.ultras.2017.11.002. → p. 11, 12

[102] Klaus-Jürgen Bathe. *Finite element procedures*. Klaus-Jurgen Bathe, 2006. → p. 11

[103] BD Shook, HR Millwater, MP Enright, SJ Hudak Jr, and WL Francis. Simulation of recurring automated inspections on probability-of-fracture estimates. *Structural Health Monitoring*, 7(4): 293–307, 2008. → p. 11

[104] Vishnuvardhan Janapati, Fotis Kopsaftopoulos, Frank Li, Sang Jun Lee, and Fu-Kuo Chang. Damage detection sensitivity characterization of acousto-ultrasound-based structural health monitoring techniques. *Structural Health Monitoring*, 15(2):143–161, 2016-02. doi: 10.1177/1475921715627490. → p. 11, 67

[105] Andrea Gianneo, Michele Carboni, and Marco Giglio. Feasibility study of a multi-parameter probability of detection formulation for a Lamb waves–based structural health monitoring approach to light alloy aeronautical plates. *Structural Health Monitoring*, 16(2):225–249, 2017. doi: 10.1177/1475921716670841. → p. 11

[106] Inka Mueller. *Inspection of piezoelectric transducers used for structural health monitoring systems*. PhD thesis, Universität Siegen, 2016. URL https://dspace.ub.uni-siegen.de/handle/ubsi/1086. → p. 11

[107] Jérémy Moriot, Nicolas Quaegebeur, Alain Le Duff, and Patrice Masson. A model-based approach for statistical assessment of detection and localization performance of guided wave–based imaging techniques. *Structural Health Monitoring*, 17(6):1460–1472, 2018. → p. 11, 63

[108] Kilian Tschöke, Inka Mueller, Vittorio Memmolo, Maria Moix-Bonet, Jochen Moll, Yevgeniya Lugovtsova, Mikhail Golub, Ramanan Sridaran Venkat, and Lars Schubert. Feasibility of model-assisted probability of detection principles for structural health monitoring systems based on guided waves for fiber-reinforced composites. *IEEE Transactions on Ultrasonics, Ferroelectrics, and Frequency Control*, 68(10):3156–3173, 2021. → p. 11, 14, 102

[109] Christine M Schubert Kabban, Brandon M Greenwell, Martin P DeSimio, and Mark M Derriso. The probability of detection for structural health monitoring systems: Repeated measures data. *Structural Health Monitoring*, 14(3):252–264, 2015-01. doi: 10.1177/1475921714566530. → p. 11, 13, 61, 95

[110] William Q Meeker, Dennis Roach, and Seth S Kessler. Statistical methods for probability of detection in structural health monitoring. In *International Workshop on Structural Health Monitoring*, 2019. → p. 11, 13, 61, 80, 83, 84, 88, 90, 91

[111] Emily O'Connor. Quantifying method differences in predicting the probability of detection for structural health monitoring applications. *Iowa State university digital repository*, 2019. → p. 11, 96

[112] Vahan Baronian, Laurent Bourgeois, Bastien Chapuis, and Arnaud Recoquillay. Linear sampling method applied to non destructive testing of an elastic waveguide: theory, numerics and experiments. *Inverse Problems*, 34(7):075006, 2018. → p. 12

[113] Roberto Miorelli, Andrii Kulakovskyi, Bastien Chapuis, Oscar D'Almeida, and Olivier Mesnil. Supervised learning strategy for classification and regression tasks applied to aeronautical structural health monitoring problems. *Ultrasonics*, 113:106372, 2021-05. doi: 10.1016/j.ultras.2021.106372. → p. 12

[114] C. Willberg, S. Duczek, J. M. Vivar-Perez, and Z. A. B. Ahmad. Simulation methods for guided wave-based structural health monitoring: A review. *Applied Mechanics Reviews*, 67(1), 2015-01. doi: 10.1115/1.4029539. → p. 12

[115] BC Lee and WJ Staszewski. Modelling of Lamb waves for damage detection in metallic structures: Part i. wave propagation. *Smart materials and structures*, 12(5):804, 2003. → p. 12

[116] Ajay Raghavan and Carlos ES Cesnik. Modeling of piezoelectric-based Lamb wave generation and sensing for structural health monitoring. In *Smart Structures and Materials 2004: Sensors and Smart Structures Technologies for Civil, Mechanical, and Aerospace Systems*, volume 5391, pages 419–430. SPIE, 2004. → p. 12

[117] Ajay Raghavan and Carlos E. S. Cesnik. 3-D elasticity-based modeling of anisotropic piezocomposite transducers for guided wave structural health monitoring. *Journal of Vibration and Acoustics*, 129 (6):739–751, 2007-02. doi: 10.1115/1.2748776. → p. 12, 37

[118] Ajay Raghavan and Carlos ES Cesnik. Finite-dimensional piezoelectric transducer modeling for guided wave based structural health monitoring. *Smart materials and structures*, 14(6):1448, 2005. → p. 12

[119] Jordan Barras, Alain Lhémery, and Alexandre Impériale. Modal pencil method for the radiation of guided wave fields in finite isotropic plates validated by a transient spectral finite element method. *Ultrasonics*, 103:106078, 2020-04. doi: 10.1016/j.ultras.2020.106078. → p. 12

[120] Fabien Treyssède and Laurent Laguerre. Numerical and analytical calculation of modal excitability for elastic wave generation in lossy waveguides. *The Journal of the Acoustical Society of America*, 133(6):3827–3837, 2013-06. doi: 10.1121/1.4802651. → p. 12

[121] Srinivasan Gopalakrishnan, Abir Chakraborty, and Debiprosad Roy Mahapatra. *Spectral finite element method: wave propagation, diagnostics and control in anisotropic and inhomogeneous structures*. Springer Science & Business Media, 2007. → p. 12

[122] V. Baronian, A. Lhémery, and K. Jezzine. Hybrid SAFE/FE simulation of inspections of elastic waveguides containing several local discontinuities or defects. *AIP Conference Proceedings*, 1335(1): 183–190, 2011. doi: 10.1063/1.3591855. → p. 12

[123] Emmanuel Lizé, Marc Rébillat, Nazih Mechbal, and Christian Bolzmacher. Optimal dual-PZT sizing and network design for baseline-free SHM of complex anisotropic composite structures. *Smart Materials and Structures*, 27(11):115018, 2018. → p. 12

[124] Wieslaw Ostachowicz, Pawel Kudela, Marek Krawczuk, and Arkadiusz Zak. *Guided waves in structures for SHM: the time-domain spectral element method*. John Wiley & Sons, 2011. doi: 10.1002/9781119965855. → p. 12

[125] Pawel Kudela. Parallel implementation of spectral element method for Lamb wave propagation modeling. *International Journal for Numerical Methods in Engineering*, 106:413–429, 2016. doi: https://doi.org/10.1002/nme.5119. → p. 12

[126] Alexandre Imperiale and Edouard Demaldent. A macro-element strategy based upon spectral finite elements and mortar elements for transient wave propagation modeling. application to ultrasonic testing of laminate composite materials. *International Journal for Numerical Methods in Engineering*, 119(10):964–990, 2019. doi: 10.1002/nme.6080. → p. 12, 13, 26

[127] Olivier Mesnil, Arnaud Recoquillay, Tom Druet, Valentin Serey, Huu Tinh Hoang, Alexandre Imperiale, and Edouard Demaldent. Experimental validation of transient spectral finite element simulation tools dedicated to guided wave-based structural health monitoring. *Journal of Nondestructive Evaluation, Diagnostics and Prognostics of Engineering Systems*, 4(4), 2021. → p. 12

[128] Jochen Moll, Jens Kathol, Claus-Peter Fritzen, Maria Moix-Bonet, Marcel Rennoch, Michael Koerdt, Axel S Herrmann, Markus GR Sause, and Martin Bach. Open guided waves: online platform for ultrasonic guided wave measurements. *Structural Health Monitoring*, 18(5-6):1903–1914, 2018. doi: 10.1177/1475921718817169. → p. 12

[129] Olivier Mesnil, Alexandre Imperiale, Edouard Demaldent, and Bastien Chapuis. Validation of spectral finite element simulation tools dedicated to guided wave based structure health monitoring. *AIP Conference Proceedings*, 2102(1):050018, 2019. doi: 10.1063/1.5099784. → p. 12

[130] Gary C Cohen. *Higher-order numerical methods for transient wave equations*, volume 5. Springer, 2002. → p. 12

[131] Victor Giurgiutiu. Tuned Lamb wave excitation and detection with piezoelectric wafer active sensors for structural health monitoring. *Journal of Intelligent Material Systems and Structures*, 16(4):291–305, 2005. doi: 10.1177/1045389x05050106. → p. 13, 24, 28, 37, 63

[132] Evgeny Glushkov, Natalia Glushkova, Oleg Kvasha, and Wolfgang Seemann. Integral equation based modeling of the interaction between piezoelectric patch actuators and an elastic substrate. *Smart Materials and Structures*, 16(3):650–664, 2007. doi: 10.1088/0964-1726/16/3/012. → p. 13, 36

[133] S Beard, B Liu, P Qing, and D Zhang. Challenges in implementation of SHM. In *6th Internat. Workshop on Structural Health Monitoring (IWSHM)*, 2007. → p. 13

[134] Bastien Chapuis, Pierre Calmon, and Frédéric Jenson. *Best Practices for the Use of Simulation in POD Curves Estimation*. Springer International Publishing, 2018. doi: 10.1007/978-3-319-62659-8. → p. 14, 60

[135] Edward F Crawley and Javier De Luis. Use of piezoelectric actuators as elements of intelligent structures. *AIAA journal*, 25(10):1373–1385, 1987. doi: 10.2514/3.9792. → p. 24, 36

[136] Edward F Crawley and Eric H Anderson. Detailed models of piezoceramic actuation of beams. *Journal of Intelligent Material Systems and Structures*, 1(1):4–25, 1990. doi: 10.1177/1045389x9000100102. → p. 24, 25, 36

[137] PZT-5A. Comsol multiphysics® v. 5.5. *COMSOL AB, Stockholm, Sweden.*, 9:707, 2020. URL https://doc.comsol.com/5.5/doc/com.comsol.help.comsol/COMSOL_ReferenceManual.pdf. → p. 27, 41

[138] D Alleyne and Peter Cawley. A two-dimensional Fourier transform method for the measurement of propagating multimode signals. *The Journal of the Acoustical Society of America*, 89(3):1159–1168, 1991. → p. 28

[139] Santosh Kapuria, Bhabagrahi Natha Sharma, and A. Arockiarajan. Dynamic shear-lag model for stress transfer in piezoelectric transducer bonded to plate. *AIAA Journal*, 57(5):2123–2133, may 2019. doi: 10.2514/1.j057681. → p. 29, 37

[140] N Quaegebeur, P-C Ostiguy, and P Masson. Hybrid empirical/analytical modeling of guided wave generation by circular piezoceramics. *Smart Materials and Structures*, 24(3):035003, feb 2015. doi: 10.1088/0964-1726/24/3/035003. → p. 30, 38, 39, 41

[141] Suresh Bhalla and Chee Kiong Soh. Structural health monitoring by piezo-impedance transducers.

i: Modeling. *Journal of Aerospace Engineering*, 17(4):154–165, oct 2004. doi: 10.1061/(asce) 0893-1321(2004)17:4(154). → p. 37

[142] Suresh Bhalla and Chee Kiong Soh. Structural health monitoring by piezo–impedance transducers. II: Applications. *Journal of Aerospace Engineering*, 17(4):166–175, oct 2004. doi: 10.1061/(asce) 0893-1321(2004)17:4(166). → p. 37

[143] Suresh Bhalla and Chee Kiong Soh. Electromechanical impedance modeling for adhesively bonded piezo-transducers. *Journal of Intelligent Material Systems and Structures*, 15(12):955–972, dec 2004. doi: 10.1177/1045389x04046309. → p. 37

[144] Lingyu Yu, Giola Bottai-Santoni, and Victor Giurgiutiu. Shear lag solution for tuning ultrasonic piezoelectric wafer active sensors with applications to Lamb wave array imaging. *International Journal of Engineering Science*, 48(10):848–861, oct 2010. doi: 10.1016/j.ijengsci.2010.05.007. → p. 37

[145] Lingfang Li, Mohammad Faisal Haider, Hanfei Mei, Victor Giurgiutiu, and Yong Xia. Theoretical calculation of circular-crested Lamb wave field in single-and multi-layer isotropic plates using the normal mode expansion method. *Structural Health Monitoring*, pages 357–372, 2019. doi: 10.1177/1475921719848149. → p. 37

[146] Hoon Sohn and Sang Jun Lee. Lamb wave tuning curve calibration for surface-bonded piezoelectric transducers. *Smart Materials and Structures*, 19(1):015007, nov 2009. doi: 10.1088/0964-1726/19/1/015007. → p. 37

[147] Jun Li, Zahra Sharif Khodaei, and M H Aliabadi. Boundary element modelling of ultrasonic Lamb waves for structural health monitoring. *Smart Materials and Structures*, 29(10):105030, sep 2020. doi: 10.1088/1361-665x/aba6ce. → p. 38

[148] Santosh Kapuria, Bhabagrahi Natha Sharma, and A Arockiarajan. Role of transducer inertia in generation, sensing, and time-reversal process of Lamb waves in thin plates with surface-bonded piezoelectric transducers. *Journal of Intelligent Material Systems and Structures*, page 1045389X2110290, jul 2021. doi: 10.1177/1045389x211029043. → p. 40

[149] Valentin Serey, Nicolas Quaegebeur, Philippe Micheau, Patrice Masson, Michel Castaings, and Mathieu Renier. Selective generation of ultrasonic guided waves in a bi-dimensional waveguide. *Structural Health Monitoring*, 18(4):1324–1336, 2018. doi: 10.1177/1475921718808220. → p. 40

[150] Modif-PZT-4. SM111. http://www.steminc.com/piezo/PZ_property.asp, 2015. STEMINC Piezoelectric Supplier. → p. 41, 64

[151] Jochen Moll, Mikhail V Golub, Evgeny Glushkov, Natalia Glushkova, and Claus-Peter Fritzen. Non-axisymmetric Lamb wave excitation by piezoelectric wafer active sensors. *Sensors and Actuators A: Physical*, 174:173–180, 2012. → p. 52

[152] D Roach. Real time crack detection using mountable comparative vacuum monitoring sensors. *Smart structures and systems*, 5(4):317–328, 2009. → p. 60

[153] Olivier Mesnil, Roberto Miorelli, Xavier Artusi, Pierre Calmon, Bastien Chapuis, and Oscar D'Almeida. Model assisted probability of detection applied to guided wave imaging for structural health monitoring. *Review of Progress in Quantitative Nondestructive Evaluation*, 2019. → p. 60, 66

[154] Kyle R Mulligan, Nicolas Quaegebeur, Patrice Masson, Louis-Philippe Brault, and Chunsheng Yang. Compensation of piezoceramic bonding layer degradation for structural health monitoring. *Structural Health Monitoring: An International Journal*, 13(1):68–81, sep 2013. doi: 10.1177/1475921713500516. → p. 66

[155] G Konstantinidis, BW Drinkwater, and PD Wilcox. The temperature stability of guided wave structural health monitoring systems. *Smart Materials and Structures*, 15(4):967, 2006. → p. 67, 68

[156] Gilles Hennenfent and Felix J. Herrmann. Simply denoise: Wavefield reconstruction via jittered undersampling. *Geophysics*, 73(3):V19–V28, 2008-05. doi: 10.1190/1.2841038. → p. 69

[157] Ziemowit Dworakowski, Lukasz Ambrozinski, Pawel Packo, Krzysztof Dragan, and Tadeusz Stepinski. Application of artificial neural networks for compounding multiple damage indices in Lamb-wave-based damage detection. *Structural Control and Health Monitoring*, 22(1):50–61, 2014-04. doi: 10.1002/stc.1659. → p. 71

[158] Ye Lu, Lin Ye, Zhongqing Su, and Chunhui Yang. Quantitative assessment of through-thickness crack size based on Lamb wave scattering in aluminium plates. *NDT & e International*, 41(1): 59–68, 2008. → p. 76

[159] Jochen H Kurz, Anne Jüngert, Sandra Dugan, and Gerd Dobmann. Probability of detection (POD) determination using ultrasound phased array for considering NDT in probabilistic damage assessments. In *South-African Insitute for Non-destructive Testing: World Conference on Nondestructive Testing (18), WCNDT*. Citeseer, 2012. → p. 79

[160] Andrew Gelman, John B Carlin, Hal S Stern, and Donald B Rubin. *Bayesian data analysis*. Chapman and Hall/CRC, 1995. → p. 83

[161] Kevin P Murphy. *Machine learning: a probabilistic perspective*. MIT press, 2012. → p. 83

[162] Gareth James, Daniela Witten, Trevor Hastie, and Robert Tibshirani. *An introduction to statistical learning*, volume 112. Springer, 2013. → p. 83

[163] Fiona Steele. Module 5: Introduction to multilevel modelling concepts. *LEMMA (Learning Environment for Multilevel Methodology and Applications), Centre for Multilevel Modelling, University of Bristol*, 2008. → p. 83

[164] Peter D Hoff. *Lecture Notes on Hierarchical Modeling*. Class notes, 2019. → p. 83

[165] Luca Gandossi and Charles Annis. Probability of detection curves: Statistical best-practices. *ENIQ report*, 41, 2010. → p. 83

[166] William Q Meeker, Gerald J Hahn, and Luis A Escobar. *Statistical intervals: a guide for practitioners and researchers*, volume 541. John Wiley & Sons, 2017. → p. 85, 87

[167] Richard McElreath. *Statistical rethinking: A Bayesian course with examples in R and Stan*. Chapman and Hall/CRC, 2020. → p. 88, 91

[168] Peter D Hoff. *A first course in Bayesian statistical methods*, volume 580. Springer, 2009. → p. 88, 91

[169] John Salvatier, Thomas V Wiecki, and Christopher Fonnesbeck. Probabilistic programming in Python using PyMC3. *PeerJ Computer Science*, 2:e55, 2016. → p. 91

[170] Iikka Virkkunen, Martin Bolander, Heikki Myöhänen, Roberto Miorelli, Ola Johansson, Philip Kicherer, Chris Curtis, and Oliver Martin. Qualification of non-destructive testing systems that make use of machine learning: ENIQ Recommended Practice 13. *ENIQ report*, 2021. → p. 102

[171] Jérémy Moriot, Nicolas Quaegebeur, Alain Le Duff, and Patrice Masson. A model-based approach for statistical assessment of detection and localization performance of guided wave–based imaging techniques. *Structural Health Monitoring*, 17(6):1460–1472, 2017-12. doi: 10.1177/1475921717744679. → p. 102